

People's Democratic Republic of Algeria
الجمهورية الديمقراطية الشعبية الجزائرية
Ministry of Higher Education and Scientific Research
وزارة التعليم العالي والبحث العلمي



Mohamed Khider University-Biskra
Faculty of Science and Technology
Department of Mechanical Engineering

Ref :...../2020

Thesis

Presented for obtaining the

Master's degree

In Mechanical Engineering

Option: Energy Systems and Sustainable Development

By

Mammar Bouhelal

Thermal design of Earth–Air Heat Exchanger (EAHE) using analytical, semi-analytical and CFD methods

Before the jury members composed of:

Adel Benchabane	Professor, Univ-Biskra, Alegria	Supervisor
Nora Boultif	MCB, Univ-Biskra, Alegria	Chairman
Hocine Djemai	MCB, Univ-Biskra, Algeria	Examiner

University of Biskra 2020

Université de Mohamed Khider Biskra
Université de Biskra, BP 145 RP, 07000 Biskra, Algérie
www.univ-biskra.dz

République Algérienne Démocratique et Populaire
الجمهورية الديمقراطية الشعبية الجزائرية
Ministère de l'Enseignement Supérieur et de la Recherche Scientifique
وزارة التعليم العالي والبحث العلمي



Université Mohamed Khider Biskra
Faculté des Sciences et de la Technologie
Département de Génie Mécanique

Ref :/2020

Mémoire de fin d'étude
Présenté pour l'obtention du diplôme de
MASTER

En Génie Mécanique
Spécialité: Systèmes énergétiques et développement durable

Présenté par
Mammar Bouhelal

**Thermal design of Earth–Air Heat Exchanger (EAHE)
using analytical, semi-analytical and CFD methods**

Devant le jury composé de :

Adel Benchabane	Professeur, Univ-Biskra, Algérie	Encadreur
Nora Boultif	MCB, Univ-Biskra, Algérie	Président
Hocine Djemai	MCB, Univ-Biskra, Algérie	Examineur

Université de Biskra 2020

Dedication

I would like to dedicate this modest work:

To my dear father and to my dear mother

To my brother: Abdelhamid and to all my sisters

To all members of my family and to all my dear and faithful friends

Acknowledgements

First and foremost, I thank ALLAH, who gave me life and health, I am grateful for his help in the realization of this thesis.

Firstly, I would like to thank my thesis supervisor, Pr. Adel BENCHABANE (Professor, University of Biskra) for having entrusted me with this research work and for his availability throughout the project, his excellent guidance, understanding and patience.

In the second place, I would like to thank Dr. Abdelhamid BOUHELAL (MCB, Ecole Nationale Polytechnique, Algiers). I am very grateful for his great help and encouragement during the period of this thesis.

I also avail myself of this opportunity to thank members of my thesis committee: Dr. Nora Boulouf, and Dr. Hocine Djemai. I appreciate your time and efforts to evaluate this thesis.

Finally, I thank all those who helped me and supported me from near or far,

Thank you very much to all.

Contents

Dedication	i
Acknowledgements	ii
Contents	iii
List of Tables	vi
Liste of Figures	vii
Introduction	1
Chapter 1: Overview and Literature Review	4
1.1 Brief history of geothermal energy	4
1.2 Definition of geothermal	5
1.3 Geothermal gradient	5
1.4 Type of geothermal systems	6
1.4.1 Geothermal electricity	6
1.4.2 Geothermal direct use	7
1.4.3 Geothermal heat pumps	8
1.5 Classification of Geothermal	8
1.5.1 High grade geothermal energy	8
1.5.2 Low grade geothermal energy	9
1.5.3 Very low-grade geothermal energy	9
1.6 Definition of Earth to air heat exchanger (EAHEs)	9
1.7 Functional principle of EAHEs	9
1.8 Classification of EAHE	10
1.8.1 Open loop system	10
1.8.2 Closed loop system:	10
1.8.3 Hybrid systems	11
1.9 Literature review on the EAHE prediction methods	12
1.9.1 Analytical methods	13
I.9.1.1 Infinite line source model (ILS)	13

1.9.1.2 Infinite Cylinder Source (ICS)	13
1.9.1.3 Finite Line Source (FLS)	13
1.9.2 Numerical methods	14
Chapter 2: Mathematical Formulation	16
2.1 Temperature of the ground	16
2.2 Analytical models	23
2.2.1 Infinite line source model	23
2.2.2 Infinite cylindrical source model	27
2.2.3 Finite line source model	31
2.3 Semi-analytical model	36
2.3.1 Estimation of air temperature	37
2.3.2 Estimation of soil thermal resistance	38
2.3.3 Organizational chart of the GRBM model	42
2.4 CFD model	44
2.4.1 Governing equations	44
2.4.2 Turbulence modeling approaches	44
2.4.2.1 Large eddy simulation (LES)	45
2.4.2.2 Statistical approach	45
2.4.3 Reynolds averaged equations	46
2.4.4 Closure problem	46
2.4.5 Boussinesq hypothesis	46
2.4.6 Turbulence model: k- ϵ model	47
Chapter 3: Numerical Modeling and Implementation	50
3.1 Temperature of the ground: Kusuda equation	50
3.2 Implementation of the analytical models	51
3.2.1 Calculation steps	51
3.2.2 Calculation subroutine	52
3.1.2.1 ILS model implementation	52
3.1.2.2 ICS model implementation	53
3.1.2.3 FLS model implementation	53
3.3 Implementation of the semi-analytical model	54
3.3.1 RBM model implementation	54
3.3.2 GRBM model implementation	55
3.4 CFD modeling	57
3.4.1 Geometry design	57

3.4.2	Mesh generation	58
3.4.3	Discretization of equations	59
3.4.3.1	First-order upwind	61
3.4.3.2	Second-order upwind	61
3.4.4	Pressure interpolation schemes	62
3.4.4.1	Linear	62
3.4.4.2	Second order	62
3.4.4.3	PRESTO	62
3.4.4.4	Body Force Weighted	63
3.4.4.5	Standard	63
3.4.5	Pressure-Velocity coupling	63
3.4.5.1	SIMPLE/SIMPLEC algorithms	64
3.4.5.2	Coupled algorithm	64
3.4.6	Boundary conditions	65
Chapter 4:	Results and Discussion	67
4.1	Description of the experimental EAHE setup	67
4.2	Determination of the undistributed soil temperature	69
4.3	Analytical simulations	70
4.3.1	ICS model	70
4.3.2	ILS model	74
4.3.3	FLS model	77
4.4	Semi-analytical model	81
4.5	CFD model	84
4.6	Comparisons of results	88
	Conclusion	91
	Bibliography	93

List of Tables

Tableau 1: Input parameters for the comparative verification with Barakat et al.....	55
Tableau 2 : Physical and thermal properties of air, pipe and soil used in the validation.....	70
Tableau 3: Validation of the ICS model air temperatures with the experimental measurements carried out in the University of Biskra (May 2 nd , 2013).....	73
Tableau 4: Validation of the ILS model air temperatures with the experimental measurements carried out in the University of Biskra (May 2 nd , 2013).	77
Tableau 5: Validation of the FLS model air temperatures with the experimental measurements carried out in the University of Biskra (May 2 nd , 2013).	80
Tableau 6: Validation of the GRBM model air temperatures with the experimental measurements carried out in the University of Biskra (May 2 nd , 2013).	84
Tableau 7: Validation of the CFD model air temperatures with the experimental measurements carried out in the University of Biskra (May 2 nd , 2013).	87
Tableau 8: Comparison of min and max relative errors.....	90

List of Figures

Figure 1: A scheme of open and closed geothermal systems.....	6
Figure 2: Simplified diagram of earth to air heat exchanger.	10
Figure 3: Open loop system.	10
Figure 4: Closed loop system.....	11
Figure 5: Horizontal loop and vertical loop system.	12
Figure 6: Parallel tube and one tube system.....	12
Figure 7: diagram of heat transfer in the soil.	17
Figure 8: Contour path of the ICS model.....	30
Figure 9: Finite line source model.	34
Figure 10: Scheme shows the subdivision of the EAHE pipe and the soil into many layers according to the GRBM model, where i, j and k are the indexes of time, layer and radius respectively.....	37
Figure 11: Scheme shows the disturbed soil thickness, δ , and the soil radius $r\delta$	39
Figure 12: Axial and radial views of the pipe and the surrounding soil at j th layer where the soil is considered as a semi-infinite hollow cylinder, where i, j and k are the indexes of time, layer and radius respectively.....	40
Figure 13: Detailed organizational chart of GRBM model.....	43
Figure 14: Measured and predicted ground temperature at depths 1 m, 8.5 m, 16 m, and 26 m at Varennes for the period from February 4 th to November 25 th , 2014.....	51
Figure 15: Representation of the EAHE separated into segments used in analytical IFS, ICS and FLS models.....	52

Figure 16: Reverification of the RBM model with the work of Barakat et al. [45].	55
Figure 17: Geometry of the EAHE and surrounding soil in ANSYS Workbench.	57
Figure 18: Mesh generation using ANSYS Workbench.	58
Figure 19: Example of a 2-D triangular control volume.	60
Figure 20 : Photos of the experimental EAHE setup in the University of Biskra: (a) hole with a serpentine shape; (b) buried horizontal PVC pipe with thermocouples.	67
Figure 21: Scheme shows the position of thermocouples measuring air flow temperatures (T_{in} , T_1 , T_2 , ..., T_{14}) with the following distances (from the EAHE inlet): 0, 63, 469, 872, 1089, 1304, 1707, 2337, 2607, 3010, 3400, 3589, 3782, 4210, 4700 cm.	68
Figure 22: Variation of EAHE temperature with time at different positions.	68
Figure 23: Variation of the min, max and average temperature at the level of 2 m, measured for Biskra region by [58].	69
Figure 24: Distribution of the ground temperature with depth simulated for Biskra region using Kusuda equation.	70
Figure 25: Variation of the air temperature with EAHE length, calculated using ICS model.	71
Figure 26: Validation of the ICS model with experimental results after different hours of functioning.	72
Figure 27: Variation of the outlet temperature with time of operation, validation of the ICS model with experimental data.	74
Figure 28: Variation of the air temperature with EAHE length, calculated using ILS model.	75
Figure 29: Variation of the outlet temperature with time of operation, validation of the ILS model with experimental data.	75
Figure 30: Validation of the ILS model with experimental results after different hours of functioning.	76
Figure 31: Variation of the air temperature with EAHE length, calculated using FLS model.	78
Figure 32: Validation of the FLS model with experimental results after different hours of functioning.	79

Figure 33: Variation of the outlet temperature with time of operation, validation of the FLS model with experimental data.	81
Figure 34: Variation of the air temperature with EAHE length, calculated using GRBM model.	82
Figure 35: Variation of the outlet temperature with time of operation, validation of the GRBM model with experimental data.	82
Figure 36: Validation of the GRBM model with experimental results after different hours of functioning.....	83
Figure 37: Variation of the air temperature with EAHE length, calculated using CFD model.	85
Figure 38: Validation of the CFD model with experimental results after different hours of functioning.....	86
Figure 39: Variation of the outlet temperature with time of operation, validation of the CFD model with experimental data.	88
Figure 40: Comparison of local relative error computed using different models.	89
Figure 41: Outlet air temperature variation after 6 hours of operation, comparison between analytical, semi-analytical and CFD methods.	89

Introduction

Energy is a fundamental input to economic activity. Modern energy services light up our homes and schools, fuel economic activity to produce and consume, provide comfort and mobility, pump water and contribute to health and well-being. Harnessing energy sources to replace manual and animal labour was the platform of the Industrial Revolution: a period of unprecedented economic and social development.

The 20th century witnessed large increases in the global population, economic output and fossil fuel consumption. The gains from growth have been impressive for many people. Yet these gains have taken a toll on a range of environmental systems where unsustainable practices have dominated [1]. Continuing deterioration of natural resources could stress the ability to meet the needs of a growing population and undermine economic activity. Green growth could meet this challenge. Green growth is about fostering economic growth and development while ensuring that natural assets continue to provide the ecosystem services on which our well-being relies. To do this it must catalyze investment and innovation which will underpin sustained growth and give rise to new economic opportunities.

The renewable resources include, but are not limited to, bioenergy, geothermal energy, hydropower, solar energy, ocean energy, and wind energy. According to the International Energy Agency's 2018 report [2], renewables saw the highest growth rate of any energy source (nuclear, gas, oil, coal, etc.) in 2017, meeting a quarter of global energy demand growth last year.

Geothermal energy is considered among renewable energy resources that permits easy access for supplying low-degree thermal energy without harming the environment. It has been considered as a promising solution for space cooling and heating. Several ways of ground heat exchangers have been proposed and used in order to absorb/release heat from/in the ground. Earth to Air Heat Exchanger (EAHE) is one of the promising techniques. This system is made of long metallic, plastic or concrete pipes that are laid underground and are connected to the air

intake of buildings and houses. The air blown through the pipes, exchanges heat with the ground and gets heat/cool depending on the temperature difference between the air and the ground. The resulting warm/cold air is used to regulate the indoor temperature in order to satisfy the human comfort. This system requires low energy consumption.

The transient simulation of thermal behavior of EAHEs is an important step in the design and optimization. Different analytical, semi-analytical and numerical method have been developed and used, in the literature, for simulate the performances of the EAHEs. The main contribution of this work is to evaluate the ability of different types of analytical/numerical methods to predict the thermal performance of EAHEs installed in local climates of Algeria (region of Biskra). Five different methods have been implemented and validated in this study, namely as: ICS, ILS, FLS, GRBM and CFD models. The dissertation has been divided into four chapters organized as follows:

Chapter 1. we will present a general overview of geothermal energy and a quick review of the most commonly used methods for studying analytically and numerically the EAHEs.

Chapter 2. in the second chapter, the governing equations, the detailed formulation and available solutions corresponding of each model will be described.

Chapter 3. consists of presenting the numerical modeling and implementation of the studied analytical, semi-analytical and CFD methods.

Chapter 4. we will present and discuss the obtained analytical/numerical results, validation and the comparison.

Finally, the main conclusions found in this study and the main recommendations relevant to the future work will ultimately be addressed towards the end of this thesis.



Chapter **I**

*Overview and Literature
Review*



Chapter 1

Overview and Literature Review

1.1 Brief history of geothermal energy

In tropical climates, air conditioning is widely employed not only for industrial production but also for the comfort of occupants. It can be achieved efficiently by vapor compression machines, but due to depletion of ozone layer by chlorofluorocarbons (CFCs) and the need to reduce high grade energy consumption; numerous alternative techniques are being currently explored. One such proposition is the EAHE that uses soil as the heat sink and air as the transfer medium for summer cooling and winter heating. When the warm air flows in the earth air pipes, heat is transferred from air to the earth. When the warm air flows in the earth air pipes, heat is transferred from air to the earth. As result, the air temperature at the outlet is lower/higher than the ambient temperature [3, 4].

The idea of using earth as a heat sink was known in ancient times. In about 3000 BC, Iranian architects used wind towers and underground air tunnels for passive cooling. In 19th Century Wilkinson designed a Barn; in order to cool the barn during summertime, he buried a 500 ft underground passage. From the middle of the twentieth century, a number of investigators have studied the cooling potential of buried pipe. Since that time, a number of experimental and analytical studies of this technique have appeared in the literature. Goswami and Dhaliwal, they presented an analytical solution to the problem of transient heat transfer between the air and surrounding soil as the air is made to pass through a pipe buried underground. EAHE system is probably the most growing alternative renewable energy in the world. With increasing demand for energy savings in the recent years. A 10% increase has been seen in installations in about 30 countries over the last 10 years. Places like South Algeria where four-fifths of the land is desert which has a dry desert climate, where during summer maximum temperature rises to 45 °C and during winter temperature lower below 1 °C, the EAHE system

cannot be used all alone. Under this condition, EAHE system is made a conjunction with air conditioning system [3, 4].

1.2 Definition of geothermal

Geothermal energy can be described as the internal heat generation of the earth. Three methods of internal generation are common. The first is a result of the radioactive decay of elements within the earth's crust, which release thermal energy. The second method of production is the conduction of thermal energy from depth within the earth, transporting through several layers to reach the surface. Additionally, there are several areas where direct channels bring molten rock and steam to the surface. These direct channels are known as high temperature geothermal and can be used for means of electrical generation. The last of the heat generation methods is solar radiation. The earth's crust absorbs approximately 47% of the sun's solar radiation, making it a very lucrative energy source. By some estimates, this low energy geothermal is 500 times more energy than all of mankind uses in a year [5].

1.3 Geothermal gradient

The temperature of the rocks increases with depth; this is called the geothermal gradient. It varies according to the layers traversed. The average values are for the continental crust $3\text{ }^{\circ}\text{C} / 100\text{ m}$ and for the mantle $1\text{ }^{\circ}\text{C} / 100\text{ m}$. The geothermal gradient observed in the continental crust varies widely from one place to another, although the normal value in the order of $3\text{ }^{\circ}\text{C} / 100\text{ m}$, nevertheless some regions record more than $100\text{ }^{\circ}\text{C} / 100\text{m}$ as in Larderello in Italy, While others do not exceed $1\text{ }^{\circ}\text{C} / 100\text{ m}$ as in Padua. The deepest oil drilling is the best way to account for the geothermal gradient. This gradient is estimated for each oil drilling using the drilling mud temperatures.

The Algerian Sahara presents as a whole an average geothermal gradient at the order of $4\text{ }^{\circ}\text{C} / 100\text{ m}$. In the northern part of the Sahara, the average geothermal gradient is $3\text{ }^{\circ}\text{C} / 100\text{ m}$; this seems to be due to the effect of depth. A strong geothermal anomaly is well demonstrated in the western Sahara in the regions of Bechar, Beni Abbas and Timimoune. The gradient is more than $6\text{ }^{\circ}\text{C} / 100\text{m}$, it is probably due to the intense tectonics experienced by the western part of the Saharan platform during the Hercynian orogeny as reported in the reference [6].

1.4 Type of geothermal systems

Geothermal energy can be produced by drilling deep holes into the earth crust. Two systems are in use: open and closed. In the open system, the energy is produced by pumping cold water through one side of the reservoir; circulating it through hot fractured rock; and then collecting it in the other side, to be brought back to the surface. In the closed system, the energy is produced using a single borehole where cold water is pumped in one path and returned in another, using the same pipe. (Figure 1 shows a schematic representation of these two systems).

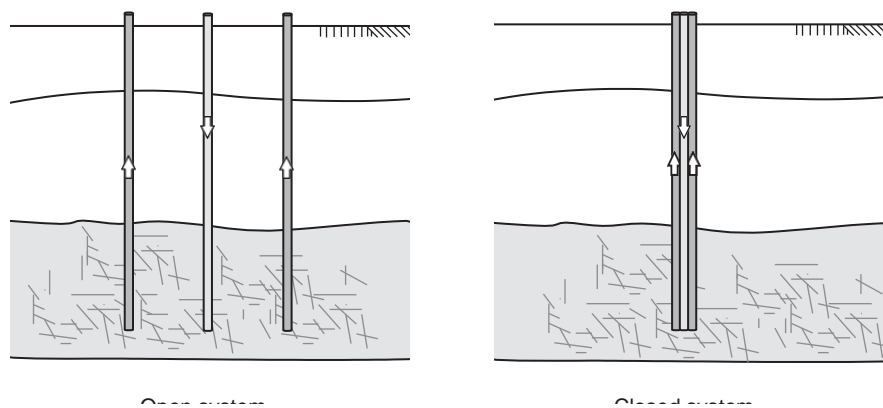


Figure 1: A scheme of open and closed geothermal systems.

Many geothermal systems have been developed, making use of the many advantages of the geothermal energy. They are in general classified into two categories: deep geothermal energy systems, and shallow geothermal systems. Deep geothermal systems are mainly those go as deep as few kilometers below the surface and reach hydrothermal aquifers, dry hot rocks or magma. Projects involving electricity production or direct heat production are classified in this category. Shallow geothermal systems, on the other hand, are those that do not go more than 250 m below the surface. The ground heat pump (GHP) is classified in this category [7].

1.4.1 Geothermal electricity

Geothermal electricity constitutes one of the most important, but also challenging sources of energy. It is an attractive source of energy because of its low CO₂ emission. The emission of CO₂ from existing geothermal electric plants is on average 122 kg of CO₂ per megawatt-hour of electricity, whereas CO₂ emission from a conventional oil combustion thermal power station is on average 760 kg of CO₂ per megawatt-hour of electricity. A geothermal power plant does not require fuel for its operation, but the capital cost is quite high.

Drilling of wells accounts for over half the costs, and exploration of deep resources entails significant risks, with a probability of over 20% failure rate.

Technologies in use include dry steam power plants, flash steam power plants and binary cycle power plants. Dry steam plants are the simplest and oldest design. They require geothermal steam of 150°C or more to drive the turbines. This entails drilling wells deeper than 3 km inside the earth. Flash steam plants pull superheated high-pressured water from deep reservoirs into lower-pressure tanks and use the resulting flashed steam to drive the turbines. They require fluid temperatures of at least 180 °C, usually more. This is the most common type of plants in operation today. Binary cycle power plants are the most recent development, and can accept fluid temperatures as low as 60 °C to drive the turbines. Water of such a temperature can be reached from hydrothermal systems, not deeper than 3 km below the surface. Due to this relatively low temperature requirement, this type of geothermal electricity plants is recently becoming the most commonly built system [7].

1.4.2 Geothermal direct use

This kind of energy constitutes one of the oldest ways of energy consumption, and the most popular source of geothermal energy. It has been utilized for hundreds of years when people started using natural hot springs for cooking, heating, and entertainment. In modern time, hot water has been extracted from deep geothermal reservoirs, few kilometers below the surface of the earth, and used directly for heating of buildings, greenhouses and industry. Geothermal reservoirs of low-to-moderate water temperature ranging from 40°C to 150°C are used for this purpose. This range of temperature is lower than those required for most geothermal power plants.

Geothermal direct-use systems consist of basically three parts: down hole well pumps, piping network, and heat exchangers. Different types of well pumps are in use and share many of the properties of those usually used in oil industry. Pipe networking is somewhat more complicated than those used in delivering urban cities with clean water since this network carries hot water. Care must be taken for insulating the pipes and reducing clogging of metals on the pipe joints and fittings. The heat exchangers work to extract heat from the coming water and dispose the resulting cold water back into the reservoir [7].

1.4.3 Geothermal heat pumps

Geothermal heat pumps (GHP) constitutes one of the most easy to extract and locally available in all parts of the world. It does not share the requirements of the other geothermal energy types in terms of geology or equipment. Rather, it makes use of the relatively constant temperature at shallow depths. In shallow grounds, just 10 m below the surface, the earth maintains nearly constant temperature ranging between 10°C and 20°C, depending on the region. Usually, the ground temperature at this depth is warmer than the air in winter and cooler in summer. Geothermal heat pumps are commonly used to exploit this abundant source of energy for heating and cooling of individual buildings and small compounds.

Geothermal heat pump systems consist of basically two parts: the ground heat exchanger, and the heat pump unit. The ground heat exchanger is a system of pipes, known as a loop, which is buried in the ground either vertically or horizontally. In winter, heat from the earth is extracted via a fluid, usually water or a mixture of water and antifreeze, circulating through the pipes at a certain rate and collecting heat from the earth. The heat pump extracts heat from the fluid and pumps it into the building. In summer, the process is reversed, and the heat pump extracts heat from the indoor air and transfers it to the heat exchanger. Heat removed from the indoor air during summer can also be used for heating water, which can be used for cooking and bathing [7].

1.5 Classification of Geothermal

1.5.1 High grade geothermal energy

High grade geothermal energy exploits the fields of dry or wet vapor (water and steam mixtures). These fields are characterized by temperatures above 150 °C. This high-grade geothermal energy is encountered in volcanic and seismic (plate boundary) regions where the geothermal gradient is particularly high.

High grade geothermal energy is mainly used for the production of electricity. The steam, which is drawn from the geothermal reservoir, is discharged into a turbine, connected to an alternator for the production of electricity. Dry steam is used directly, whereas wet steam which is more frequent requires the use of a separator, an example of this type of geothermal energy is given by Bouillante plant in Guadeloupe-France [6].

1.5.2 Low grade geothermal energy

Low grade geothermal energy is characterized by a temperature between 30 °C and 150 °C and is encountered at an average depth of 1000 to 2500 m in water permeable formations located mainly in large sedimentary basins. It is mainly used for district heating and greenhouse heating [6].

1.5.3 Very low-grade geothermal energy

Very low-grade geothermal energy is encountered at shallow depths where the temperature is in the order of 10 to 30 ° C. It is used for refreshing buildings & greenhouses, fish farming, horticulture and drying of agricultural products.

1.6 Definition of Earth to air heat exchanger (EAHEs)

A ground-coupled heat exchanger is an underground metal or plastic pipe through which air is drawn. As air travels through the pipe, it gives up or receives some of its heat to/from the surrounding soil and enters the room as conditioned air during the cooling and heating period. They use the earth's near constant subterranean temperature to warm or cool air or other fluids for residential, agricultural or industrial uses. If air from buildings is blown through the heat exchanger for heat recovery ventilation, they are called earth tubes (also known as earth cooling tubes or earth warming tubes) in Europe or earth–air heat exchangers (EAHE or EAHX) in North America [8, 9].

1.7 Functional principle of EAHEs

The principle of the EAHE is that a pipe or several pipes buried in the ground. One end of the pipe system (the inlet) acts as the entrance for outdoor ambient air, whilst the other end of the pipe system (the outlet) releases air to the interior of a building. Ambient air is drawn into the pipe inlet, the air travelling through the pipe exchanging heat with the pipe walls which are in contact with the surrounding underground environment. In this way, heat is transferred to or from the surrounding soil by conduction through the pipe wall and convection with the tunnel air, tempering the air as it flows through the pipe. Figure 2 illustrates this concept [10].

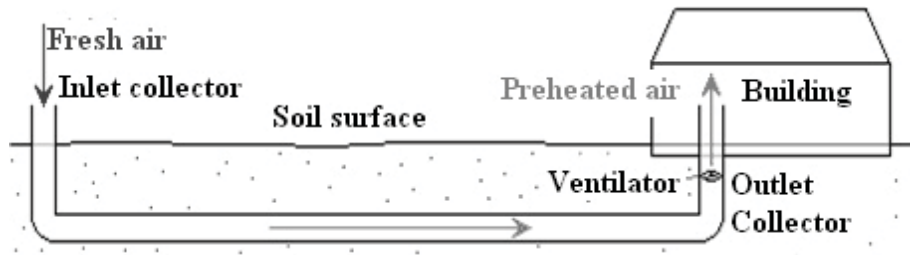


Figure 2: Simplified diagram of earth to air heat exchanger.

1.8 Classification of EAHE

The EAHE systems are designed on the basis of three configurations: open loop system and closed loop system and Hybrid system:

1.8.1 Open loop system

The ambient air is passed through the buried pipes for pre-heating or pre-cooling of air as shown in Figure 3. Then the air passes through a conventional system to cool down or get warm up before entering the space. The air is then passed away through the ventilation [4].

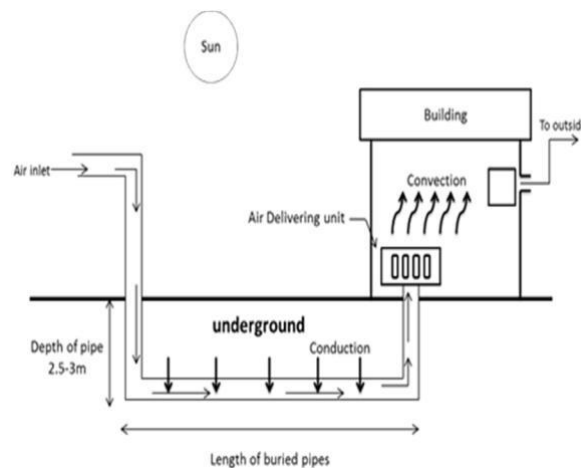


Figure 3: Open loop system.

1.8.2 Closed loop system:

Closed loop systems are also known as earth coupled system as shown in Fig. 3. Air sucked from inlet travels through a loop of pipes buried underground and extracts the heat from the ground. The ground loops are arranged either vertically or horizontally. The vertical loops

are more expensive than the horizontal loop. Closed loop is efficient than open loop system. Closed loop system reduces the problem of humidity [4].

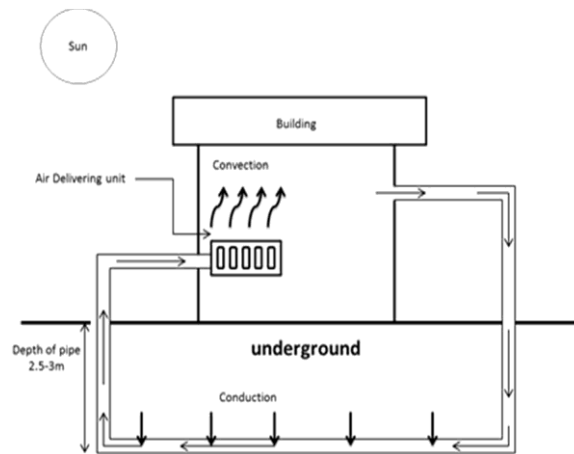


Figure 4: Closed loop system.

1.8.3 Hybrid systems

The EAHE is coupled with other heating/cooling devices such as air conditioner, heaters, solar chimney, solar air heaters etc. These devices improve the comfort and efficiency of the EAHE systems.

The EAHE are also classified on the basis of pipe layout in the ground and according to the mode of arrangement as shown in Figs. 4 and 5.

On the basis of pipe layout, the EAHE classified as:

- Horizontal/straight Loop.
- Vertical Looped.
- Slinky/spiral Looped.
- Pond/Helical Looped.

On the basis of mode of arrangement, EAHE is classified as:

- One tube system.
- Parallel tube system.

One tube system is not appropriate to meet the requirements of an air conditioning system in a building. This is because the tube is too large for the use in generation. Parallel tube systems are used as it reduces the pressure drop and increases the thermal performance of the system [4].

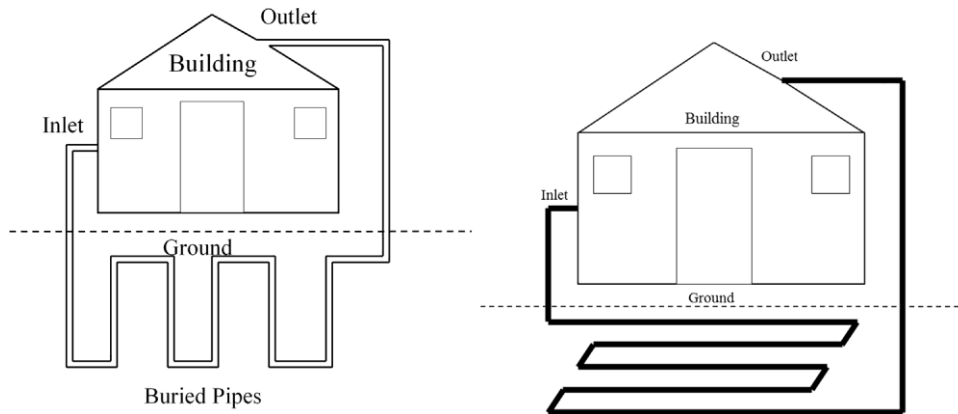


Figure 5: Horizontal loop and vertical loop system.

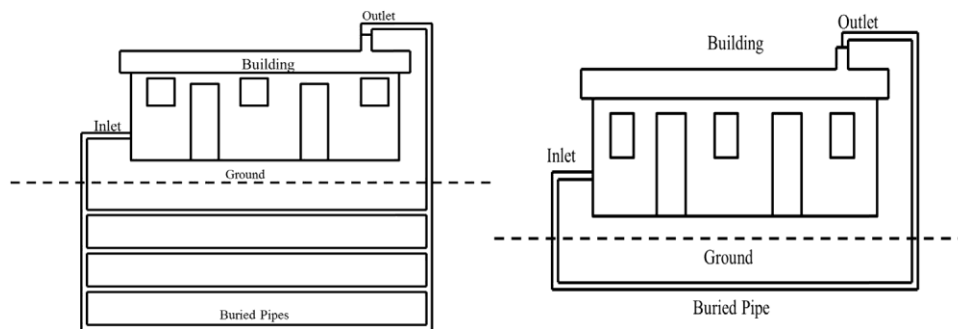


Figure 6: Parallel tube and one tube system.

1.9 Literature review on the EAHE prediction methods

In this section, we will present the most widely used methods to simulate the transient behavior of air-ground heat exchangers. These methods are categorized as analytical, semi-analytical and CFD methods. For analytical methods, three models are more widely used in the literature for vertical geothermal systems, named as Infinite Line Source (ILS), Finite Line Source (FLS) and Infinite Cylinder Source (ICS) models. These methods have been adapted for horizontal geothermal system in the present study. The methods that use a semi-analytical algorithm to simulate the transient behavior of the EAHEs are rare according to the literature, most researchers prefer purely numerical methods. In the present study, a semi-analytical

method developed by Benchabane's team denoted as GRBM model has been used. The detailed formulation on this method will be given in the next chapter.

1.9.1 Analytical methods

I.9.1.1 Infinite line source model (ILS)

The infinite line source model (ILS) is a direct utilization of the point and infinite line source solutions provided by Carslaw and Jaeger (1959). Ingersoll (1954) provided practical applications of these solutions and established the framework for more elaborate modeling of shallow geothermal systems. ILS model describes heat flow in an infinite soil mass subjected to a constant heat flux from a borehole heat exchanger. The borehole heat exchanger is represented by an infinite line embedded along the vertical axis. This modeling set-up entails that heat flow in the soil mass occurs only in the radial direction, and furthermore, the contact between the soil and the borehole heat exchangers goes along the centerline of the borehole, not along its surface area [7].

I.9.1.2 Infinite Cylinder Source (ICS)

Instead of modeling the borehole as a line, a cylinder can be used. The infinite cylinder source, often just referred to as the cylinder source model, assumes that the borehole consists of a cylindrical volume of infinite length. The contents of the borehole cylinder can be modeled in several different ways: as empty with all heat rejected from the cylinder wall, as a perfect conductor with specific thermal capacitance, and as a homogeneous material with thermal properties disparate from those of the ground (Carslaw and Jaeger 1959) [11].

1.9.1.3 Finite Line Source (FLS)

The finite line source builds upon the infinite line source model by imposing end effects and a boundary condition to model the ground surface. The ground surface is modeled by mirroring the borehole line source about the boundary as a line sink. This Method of Images creates a constant temperature boundary condition to model the surface of the ground. This is especially important for ground heat exchanger modeling when the design period is greater than a year which is when the accuracy of the model becomes more important (Spitler and Bernier

2016). Because the finite line source model is based on the integral of the point source model, when the integral is evaluated numerically it resolves into a series of point sources [11].

1.9.2 Numerical methods

Numerical models can be classified as one-dimensional, two-dimensional and three-dimensional. One-dimensional model is used to derive a relation between pipes inlet and outlet temperatures. Most of the researchers opted two-dimensional and three-dimensional models for their studies. Two-dimensional models are advanced than one-dimensional and were adopted during 90s that could calculate temperatures of ground and different depths.

Three-dimensional models are more dynamic, advanced in technology and used in recent years. Three-dimensional models allow any type of grid geometry that helps to analyze the temperature variations around the pipes and in the depth of ground. Various types of commercial computational fluid dynamics (CFD) tools for numerical modelling are available. EnergyPlus and TRANSYS are used for analysis but not quickly for design.

CFD is a popular tool for two-dimensional and three-dimensional studies. Some popular commercial CFD software are: ANSYS FLUENT, ANSYS CFX, STAR CCM+, CD, FIDAP, ADINA, OpenFoam, PHOENICS and others [12].



Chapter **II**

Mathematical Formulation



Chapter 2

Mathematical Formulation

2.1 Temperature of the ground

Evaluating the potential of using surface geothermal energy and the appropriate technology for its exploitation involves determining the variations, throughout the year, in soil temperature at different depths. These variations are obtained using simple modeling using soil properties and ambient temperatures assuming the soil as a semi-infinite media. The changes in ambient temperature as a function of time (day) is generally represented by a cosine function of the form [13].

$$T = T_i + T_{moy} \cdot \cos[w(t - t_0)]. \quad \text{Eq. 1}$$

Where:

T_i : Daily ambient temperature.

T_{moy} : Mean surface temperature (average air temperature).

W : Angular frequency [$w = (2 \times \pi)/24$] (rad/hour).

t_0 : day of the year of the maximum surface temperature at solar noon.

The heat transfer in the soil is assumed to be one-dimensional taking place by dominant conduction, while considering that it is a homogeneous medium, the unsteady equation of the heat transfer in this case is written as:

$$\Delta^2 T = \frac{\rho_{sol} C p_{sol}}{\lambda_{sol}} \cdot \frac{\partial T}{\partial t}$$

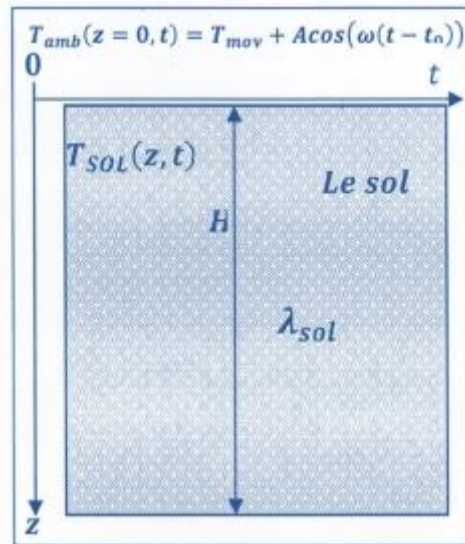


Figure 7: diagram of heat transfer in the soil.

Which can be rewritten in the form: $\frac{\partial T}{\partial t} = \alpha \nabla^2 T$

Were:

λ_{sol} : Soil conductivity. [W/m. °C]

Cp_{sol} : Thermal capacity of soil. [J/Kg. °C]

ρ_{sol} : Soil density. [Kg/m³]

T: Soil temperature, t and z function. [°C]

t: Time. [s]

z: Depth below ground surface. [m]

α : Thermal diffusivity of the ground $\alpha = \lambda / (\rho \cdot Cp)$. [m²/s]

So, the monodirectional equation of the heat transfer by conduction can be rewritten as:

$$\frac{\partial^2 T}{\partial z^2} = \frac{1}{\alpha} \cdot \frac{\partial T}{\partial t} \quad \text{Eq. 3}$$

Whose boundary conditions are:

$$T_{amb}(z = 0, t) = T_{amb} + A \cos[w(t - t_0)]$$

Where $T(\infty, t) = T_i$

Let's introduce the variable θ which is defined by: $\theta = T - T_i$

T_i : is the soil temperature at a depth z_i . such as $T(z) = T_i (\forall z > z_i)$.

The partial differential equation will then take the form:

$$\frac{\partial^2 \theta}{\partial z^2} = \frac{1}{\alpha} \cdot \frac{\partial \theta}{\partial t} \quad \text{Eq. 4}$$

Where $\bar{T} = T_{moy} - T_i$

With $\theta_{amb}(z = 0, t) = \bar{T} + A \cos[w(t - t_0)]$

Using the method of separating variables such as:

$$\theta = x(z) \cdot y(t) \quad \text{Eq. 5}$$

Let us replace in the differential partial differential equation:

$$x''(z)y(t) = \frac{1}{\alpha} x(z)y'(t) \quad \text{Eq. 6}$$

Divide the two sides of the equation by x and y:

$$\alpha \frac{x''(z)}{x(z)} = \frac{y'(t)}{y(t)} = \beta \quad \text{With } \beta \text{ constant} \quad \text{Eq. 7}$$

The sinusoidal temperature imposed on the surface, in periodic regime where the problem considered being linear, we seek a solution of the same frequency as the excitation, assuming that $\beta = i\omega$. Where $i^2 = -1$. the differential equation becomes:

$$y'(t) - \beta y(t) = 0 \quad \text{Eq. 8}$$

$$\Rightarrow \frac{dy}{dt} - \beta \cdot y = 0$$

$$\Rightarrow \frac{dy}{dt} = \beta \cdot y$$

$$\Rightarrow \frac{dy}{y} = \beta \cdot dt$$

$$\Rightarrow \ln y = \beta \cdot t + c$$

$$\Rightarrow y = e^{\beta \cdot t + c}$$

$$\Rightarrow y = K e^{i\omega \cdot t}$$

With K and c are constant.

Then let's look for the value of x , such that:

$$\alpha \frac{x''(z)}{x} = \beta \quad \text{Eq. 9}$$

$$\Rightarrow x''(z) - \frac{\beta}{\alpha} x(z) = 0$$

It is a differential equation of 2nd homogeneous order that admits as solution:

Eq. 10

$$x(z) = A. \exp\left(-\sqrt{\frac{\beta}{\alpha}}.z\right) + B. \exp\left(\sqrt{\frac{\beta}{\alpha}}.z\right)$$

Where $\lim_{z \rightarrow \infty} x(z)$ tends to a finite limit $\Rightarrow A \rightarrow 0$.

$$\text{Such that: } x(z) = B. \exp -\sqrt{\frac{\beta}{\alpha}}.z$$

If we consider the real part be the imaginary part of the solution, depending on whether the temperature varies as a periodic function of the form $\cos(\omega t)$ or $\sin(\omega t)$. We will therefore:

$$x(z) = B. \exp\left(-\sqrt{\frac{\beta}{\alpha}}.z\right) \text{ as } \sqrt{\beta} = \sqrt{i\omega}$$

Other by the real part is:

$$[X(Z).Y(Z)] = \text{real}\left[K.B. e^{-i\omega t}. e^{-\sqrt{\frac{\omega}{2\alpha}}(i+a)z}\right]$$

Eq. 11

Which must satisfy the equation T (z, t) at the point of origin of the abscissa $z = 0$, such that:

$$\theta_{amb}(z = 0, t) = \bar{T} + A \cos[w(t - t_0)]$$

$$= \text{real}[K.B. e^{-i\omega t}. 1]$$

$$= \text{real}[K.B. (\cos \omega t + i \sin \omega t)]$$

$$\Rightarrow K.B = \frac{\bar{T} + A \cos[w(t - t_0)]}{\cos \omega t}$$

From equation (Eq. 9) we get:

Eq. 12

$$\theta(z, t) = \frac{T + A \cos[w(t - t_0)]}{\cos(\omega t)} \cdot e^{-i\omega t} \cdot e^{-\sqrt{\frac{\omega}{2\alpha}}(i+1)z}$$

$$\Rightarrow \theta(z, t) = \frac{T + A \cos[w(t - t_0)]}{\cos(\omega t)} \cdot \exp\left(-\sqrt{\frac{\omega}{2\alpha}}z\right) \cdot [(\cos \omega t \cdot i \sin \omega t)] \left(\cos\left(-\sqrt{\frac{\omega}{2\alpha}}z\right)\right)$$

$$\begin{aligned} \theta(z, t) = & \frac{T + A \cos[w(t - t_0)]}{\cos(\omega t)} \cdot \exp\left(-\sqrt{\frac{\omega}{2\alpha}}z\right) \cdot \left[\left(\cos \omega t \cdot \cos\left(-\sqrt{\frac{\omega}{2\alpha}}z\right) \right. \right. \\ & + i \cos \omega t \cdot \sin\left(-\sqrt{\frac{\omega}{2\alpha}}z\right) + i \sin \omega t \cdot \cos\left(-\sqrt{\frac{\omega}{2\alpha}}z\right) \\ & \left. \left. + i^2 \sin \omega t \sin\left(-\sqrt{\frac{\omega}{2\alpha}}z\right) \right] \end{aligned}$$

So :

$$\begin{aligned} \theta(z, t) &= \frac{T + A \cos[w(t - t_0)]}{\cos(\omega t)} \cdot \exp\left(-\sqrt{\frac{\omega}{2\alpha}}z\right) \cdot \left[\left(\cos \omega t \cdot \cos\left(-\sqrt{\frac{\omega}{2\alpha}}z\right) \right. \right. \\ &- \sin \omega t \sin\left(-\sqrt{\frac{\omega}{2\alpha}}z\right) \\ &\left. \left. + i \left(\cos \omega t \cdot \sin\left(-\sqrt{\frac{\omega}{2\alpha}}z\right) + \sin \omega t \cdot \cos\left(-\sqrt{\frac{\omega}{2\alpha}}z\right) \right) \right] \end{aligned}$$

Eq. 12'

The real part in the equation:

$$\frac{T + A \cos[w(t - t_0)]}{\cos(\omega t)} \cdot \exp\left(-\sqrt{\frac{\omega}{2\alpha}}z\right) \cdot \cos\left(\omega t - \sqrt{\frac{\omega}{2\alpha}}z\right)$$

So, the solution of the equation (Eq. 4):

$$\theta(z, t) = \frac{T + A \cos[w(t - t_0)]}{\cos(\omega t)} \cdot \exp\left(-\sqrt{\frac{\omega}{2\alpha}}z\right) \cdot \cos\left(\omega t - \sqrt{\frac{\omega}{2\alpha}}z\right)$$

By replacing the boundary conditions in the equation (Eq. 12'), we get:

$$\theta(z, t) = \frac{T + A \cos[w(t - t_0)]}{\cos(\omega t)} \cdot \exp\left(-\sqrt{\frac{\omega}{2\alpha}} z\right) \cdot \cos\left(\omega t - \sqrt{\frac{\omega}{2\alpha}} z\right) - \frac{T_i}{\cos \omega t} \quad \text{Eq. 12''}$$

From equation (Eq. 12'), we get:

$$T_{sol}(z, t) = T_{moy} + A \cdot \cos[\omega(t - t_0)] \cdot \exp\left(-\sqrt{\frac{\omega}{2\alpha}} z\right) \cdot \cos\left(\omega t - \sqrt{\frac{\omega}{2\alpha}} z\right) \quad \text{Eq. 13}$$

Finally, the soil temperature as a function of time and depth takes the following expression:

$$T_{sol}(z, t) = \left[\left(T_{moy} + A \cdot \cos[\omega(t - t_0)] \cdot \exp\left(-z\sqrt{\frac{\omega}{2\alpha}}\right) \cdot \cos\left(\omega t - \sqrt{\frac{\omega}{2\alpha}} z\right) + T_i \right) \frac{1}{\cos \omega t} \right] + T_i$$

Different expressions are available in the literature, the most used one is the Kusuda equation given as:

$$T_{soil}(z, t) = T_{mean} + T_{amp} \cdot \exp\left(-z\sqrt{\frac{\omega}{2\alpha}}\right) \cdot \cos\left(t - t_{shift} - \frac{z}{2}\sqrt{\frac{\omega}{2\alpha}}\right) \quad \text{Eq. 14}$$

This form is used in several software: TRNSYS (2005) [14], DOE- 2 (1982) and RETScreen (2005) [15], where:

Where $T_{soil}(z, t)$ is the ground temperature at the given time t (hours) and at a depth z (m). While T_{mean} is the soil's average temperature (°C); on the other hand, T_{amp} is the amplitude of surface temperature (°C) calculated using $((T_{max} - T_{min})/2)$; T_{max} is the maximal ambient temperature (°C) and T_{min} is the minimal ambient temperature (°C); t_{shift} is the hour of the year with the minimum temperature value of the surface and α is the soil thermal diffusivity (m²/h). $\omega = 2\pi/365$ (radian/days) is the angular frequency.

2.2 Analytical models

2.2.1 Infinite line source model

The governing partial differential equation of the Infinite Line Source (ILS) model is described in the cylindrical coordinate system in terms of the temperature difference, $\theta(r, t) = T(r, t) - T_0$, with T_0 represents the initial temperature of the soil, as [7]:

$$\begin{aligned} \frac{1}{\alpha} \frac{\partial \theta}{\partial t} &= \frac{\partial^2 \theta}{\partial r^2} + \frac{1}{r} \frac{\partial \theta}{\partial r} \\ \theta(r, 0) &= 0 \\ \theta(r \rightarrow \infty, t) &= 0 \\ -\lambda \frac{\partial \theta}{\partial r} \cdot 2\pi r \Big|_{r \rightarrow 0} &= q_0 \end{aligned} \tag{Eq. 15}$$

In which q_0 is the borehole heat exchangers (BHE) heat flux. Solving this initial and boundary value problem is usually conducted using the Laplace transforms. Accordingly, the temperature in the Laplace domain can be described as

$$\hat{\theta}(r, s) = \mathcal{L}[\theta(r, t)] = \int_0^{\infty} e^{-st} \theta(r, t) dt \tag{Eq. 16}$$

Where the transform is conducted on the time domain. Applying Eq. (16) to the time derivative in Eq. (15) gives

$$\mathcal{L} \left[\frac{\partial \theta}{\partial t} \right] = \int_0^{\infty} e^{-st} \frac{\partial \theta}{\partial t} dt = \lim_{p \rightarrow \infty} \int_0^p e^{-st} \frac{\partial \theta}{\partial t} dt \tag{Eq. 17}$$

Integrating by parts, yields

$$\begin{aligned} \mathcal{L} \left[\frac{\partial \theta}{\partial t} \right] &= \lim_{p \rightarrow \infty} \left\{ e^{-st} \theta(r, t) \Big|_0^p + s \int_0^p e^{-st} \theta(r, t) dt \right\} \\ &= -\theta(r, 0) + s \int_0^{\infty} e^{-st} \theta(r, t) dt \\ &= s \hat{\theta}(r, s) - \theta(r, 0) \end{aligned} \tag{Eq. 18}$$

Applying the first and second order spatial derivatives gives:

$$\mathcal{L} \left[\frac{\partial \theta}{\partial r} \right] = \int_0^{\infty} e^{-st} \frac{\partial \theta}{\partial r} dt = \frac{d}{dr} \left\{ \lim_{p \rightarrow \infty} \int_0^p e^{-st} \theta dt \right\} = \frac{d\hat{\theta}}{dr} \quad \text{Eq. 19}$$

$$\mathcal{L} \left[\frac{\partial^2 \theta}{\partial r^2} \right] = \int_0^{\infty} e^{-st} \frac{\partial^2 \theta}{\partial r^2} dt = \frac{d^2}{dr^2} \left\{ \lim_{p \rightarrow \infty} \int_0^p e^{-st} \theta dt \right\} = \frac{d^2 \hat{\theta}}{dr^2}$$

Considering the initial condition yields

$$\frac{d^2 \hat{\theta}}{dr^2} + \frac{1}{r} \frac{d\hat{\theta}}{dr} - \frac{s}{\alpha} \hat{\theta} = 0 \quad \text{Eq. 20}$$

$$\hat{\theta}(r \rightarrow \infty, s) = 0$$

$$-\lambda \frac{d\hat{\theta}}{dr} \cdot 2\pi r \Big|_{r \rightarrow 0} = \frac{q_0}{s}$$

The solution of this ordinary differential equation can be expressed as

$$\hat{\theta}(r, s) = AK_0(r\sqrt{s/\alpha}) + BI_0(r\sqrt{s/\alpha}) \quad \text{Eq. 21}$$

In which I_0 and K_0 are the modified Bessel functions of zero order of the first and second kind, respectively. A and B are arbitrary constants which need to be determined from the boundary conditions. Applying the first boundary condition in Eq. (21), and as I_0 is unbounded at infinity, yields $B = 0$, and Eq. (21) becomes

$$\hat{\theta}(r, s) = AK_0(r\sqrt{s/\alpha}) \quad \text{Eq. 22}$$

Substituting Eq. (22) into the second boundary condition of Eq. (20), and knowing that

$$\lim_{r \rightarrow 0} K_1(r) \simeq \frac{1}{r} \quad \text{Eq. 23}$$

Where K_1 is the modified Bessel functions of the first order, we obtain

$$A = \frac{q_0}{2\pi\lambda s} \quad \text{Eq. 24}$$

The solution of $\hat{\theta}(r, s)$ in the Laplace domain is thus

$$\hat{\theta}(r, s) = \frac{q_0}{2\pi\lambda s} K_0(r\sqrt{s/\alpha}) \quad \text{Eq. 25}$$

Having solved the heat equation in the Laplace domain, we now have to reconstruct the temperature back to the time domain, using the inverse Laplace transform. This entails solving for:

$$\hat{\theta}(r, t) = \mathcal{L}^{-1}[\hat{\theta}(r, s)] = \frac{q_0}{2\pi\lambda s} \mathcal{L}^{-1} \left[\frac{1}{s} K_0(r\sqrt{s/\alpha}) \right] \quad \text{Eq. 26}$$

Making use of the Laplace transform of integrals

$$\frac{1}{s} \hat{f}(s) = \mathcal{L} \left[\int_0^t f(\tau) d\tau \right] \quad \text{Eq. 27}$$

Eq. (26) can be written as:

$$\theta(r, t) = \frac{q_0}{2\pi\lambda} \int_0^t \mathcal{L}^{-1} [K_0(r\sqrt{s/\alpha})] d\tau \quad \text{Eq. 28}$$

Using the inverse Laplace transform tables provided by Carslaw and Jaeger [16], we obtain:

$$\mathcal{L}^{-1} [K_0(r\sqrt{s/\alpha})] = \frac{1}{2t} \exp(-r^2/4\alpha t) \quad \text{Eq. 29}$$

Substituting Eq. (29) into Eq. (28) yields the temperature in the time domain, as:

$$\theta(r, t) = \frac{q_0}{4\pi\lambda} \int_0^t \left[\frac{1}{\tau} \exp(-r^2/4\alpha\tau) \right] d\tau \quad \text{Eq. 30}$$

This concludes the solution of the infinite line source model. For convenience, the integrand can be written using an independent variable, such that:

$$v = \frac{r^2}{4\alpha\tau} ; \quad d\tau = -\frac{r^2}{4\alpha v^2} dv \quad \text{Eq. 31}$$

Substituting Eq. (31) into Eq. (30), gives

$$\theta(r, t) = \frac{q_0}{4\pi\lambda} \int_{r^2/4\alpha t}^{\infty} \frac{e^{-v}}{v} dv \quad \text{Eq. 32}$$

In the literature, Eq. (32) is usually expressed as:

$$T(r, t) - T_0 = \frac{q_0}{2\pi\lambda} \int_{r/2\sqrt{\alpha t}}^{\infty} \frac{e^{-v^2}}{v} dv = \frac{q_0}{4\pi\lambda} Ei\left(\frac{r^2}{4\alpha t}\right) = \frac{q_0}{2\pi\lambda} Ei\left(\frac{r}{2\sqrt{\alpha t}}\right) \quad \text{Eq. 33}$$

Where $Ei(x)$ is the exponential integral function, defined as

$$Ei(x) = \int_x^{\infty} \frac{e^{-v}}{v} dv \quad \text{Eq. 34}$$

Where

$$-Ei\left(\frac{r^2}{4\alpha t}\right) = -\frac{1}{2} Ei\left(\frac{r}{2\sqrt{\alpha t}}\right) \quad \text{Eq. 35}$$

Ingersoll and Plass [17] provided tabulated values of the exponential integral function. For $r/2\sqrt{\alpha t} < 0.2$, the integral in Eq. (34) can be approximated by:

$$I(v) = \ln \frac{1}{v} + \frac{v^2}{2} - \frac{v^4}{8} - 0.2886 \quad \text{Eq. 36}$$

Ingersoll and Plass recommended using the ILS model only for applications with Fourier's number, $F_o(r_b) = \alpha t / (r_b^2) > 20$. For smaller values, the solution gets distorted in the shorter time scale because the effect of the actual finite length of the BHE becomes significant.

Hart and Couvillion [18] introduced an algebraic approximation to Eq. (33) of the form:

$$T(r, t) - T_0 = \frac{q_0}{2\pi\lambda} \left[\ln \frac{r_{\infty}}{r} - 0.9818 + \frac{2r^2}{r_{\infty}^2} - \frac{1}{8} \left(\frac{4r^2}{r_{\infty}^2} \right)^2 + O\left(\frac{4r^2}{r_{\infty}^2}\right) \right] \quad \text{Eq. 37}$$

In which r_{∞} is a hypothetical far-field radius where the effect of the line source vanishes. They also proposed a radius of the form:

$$r_{\infty} = 4\sqrt{\alpha t} \tag{Eq. 38}$$

Hart and Couvillion [18] asserted that this solution provides computationally efficient calculations for $r_{\infty} > 15r_p$, with r_p the pipe diameter. Lower than this value, the calculations become more involved.

From Eq. (33) we note that as $t \rightarrow \infty$, $Ei(0) = \infty$, and thus there exists no steady-state solution to this model. However, for a small value of v , i.e., large values of t , Carslaw and Jaeger [16] have shown that the temperature can be approximated as:

$$T(r, t) \simeq \frac{q_0}{4\pi\alpha} \ln \frac{4\alpha t}{r^2} - \frac{q_0}{4\pi\alpha} \gamma \tag{Eq. 39}$$

In which $\gamma = 0.5772$. . ., is Euler's constant. Furthermore, for the same reason, in this model the temperature at the center, where $r = 0$, cannot be calculated. Despite of these two disadvantages, the ILS model is usually used in practice to get a quick estimate of the soil temperature.

For an instantaneous line heat source, where a heat flux is released suddenly at $t = 0$ with a strength q_i (J/m), Yener and Kakac [19] have shown that the solution of the heat equation leads to:

$$\theta(r, t) = T(r, t) - T_0 = \frac{q_i}{4\pi\lambda} \frac{1}{t} \exp(-r^2/4\alpha t) \tag{Eq. 40}$$

2.2.2 Infinite cylindrical source model

Similar to the ILS model, the Infinite Cylindrical Source model (ICS) simulates heat conduction in a soil mass subjected to a constant heat flow rate. The difference, however, is that the contact area between the borehole heat exchanger and the soil is along the surface area of the borehole, i.e. at $r = r_b$, the borehole radius. The governing partial differential equation of the ICS model is described in the cylindrical coordinate system in terms of $\theta(r, t) = T(r, t) - T_0$, with T_0 represents the initial temperature of the soil, as [7]:

$$\frac{1}{\alpha} \frac{\partial \theta}{\partial t} = \frac{\partial^2 \theta}{\partial r^2} + \frac{1}{r} \frac{\partial \theta}{\partial r}, \quad r > r_b$$

$$\theta(r, 0) = 0$$

$$\theta(r \rightarrow \infty, t) = 0 \quad \text{Eq. 41}$$

$$-\lambda \frac{\partial \theta}{\partial r} \cdot 2\pi r \Big|_{r=r_b} = q_0$$

Using Laplace transform, the subsidiary equation can be expressed as:

$$\frac{d^2 \bar{\theta}}{dr^2} + \frac{1}{r} \frac{d\bar{\theta}}{dr} - \frac{s}{\alpha} \bar{\theta} = 0$$

$$\bar{\theta}(r \rightarrow \infty, s) = 0 \quad \text{Eq. 42}$$

$$-\lambda \frac{\partial \bar{\theta}}{\partial r} \cdot 2\pi r \Big|_{r=r_b} = \frac{q_0}{s}$$

$$\hat{\theta}(r, t) = \frac{q_0}{2\pi r_b \lambda s} \frac{K_0(r\sqrt{s/\alpha})}{K_1(r_b\sqrt{s/\alpha})}$$

The solution of this boundary value problem can readily be obtained as:

$$\hat{\theta}(r, t) = \frac{q_0}{2\pi r_b \lambda s} \frac{K_0(r\sqrt{s/\alpha})}{K_1(r_b\sqrt{s/\alpha})} \quad \text{Eq. 43}$$

In which K_0 and K_1 are the modified Bessel functions of the second kind of order zero and one, respectively. Then, using the Bromwich integral, the inverse Laplace transform can be expressed as:

$$\theta(r, t) = \frac{q_0}{4\pi^2 r_b \lambda_i} \int_{\gamma-i\infty}^{\gamma+i\infty} e^{st} \frac{K_0(r\sqrt{s/\alpha})}{s K_1(r_b\sqrt{s/\alpha})} ds \quad \text{Eq. 44}$$

Carslaw and Jaeger (1959) provided the solution of this integrand, of the form

$$T(r, t) - T_0 = -\frac{2Q_0}{\pi\lambda} \int_0^\infty (1 - e^{-\alpha v^2 t}) \frac{J_0(vr)Y_1(vr_b) - Y_0(vr)J_1(vr_b)}{v^2 [J_1^2(vr_b) + Y_1^2(vr_b)]} dv \quad \text{Eq. 45}$$

in which $Q_0 = q_0/2\pi r_b$, at $r = r_b$

Solving the integral in Eq. (45) is quite difficult. Nevertheless, Carslaw and Jaeger provided approximate solutions for short and long-time scales. For a short time, scale, i.e. small values of Fourier's number $\alpha t/r_b^2$, they showed that Eq. (45) can be represented as

$$T(r, t) = \frac{2Q_0}{\lambda} \sqrt{\frac{\alpha r_b t}{r}} \left[\operatorname{ierfc} \frac{r - r_b}{2\sqrt{\alpha t}} - \frac{(3r + r_b)\sqrt{\alpha t}}{4rr_b} i^2 \operatorname{erfc} \frac{r - r_b}{2\sqrt{\alpha t}} + \dots \right] \quad \text{Eq. 46}$$

where $i^n \operatorname{erfc}$ is the iterated integrals of the complementary error function, defined as:

$$i^n \operatorname{erf}(z) = \int_z^\infty i^{n-1} \operatorname{erf}(\zeta) d\zeta \quad \text{Eq. 47}$$

For a long time, scale, the evaluation of the integral in Eq. (45) becomes more involved and difficult to solve analytically. Therefore it is important to begin from the subsidiary equation and solve the problem by proper evaluation of the Bromwich integral, Eq. (44), and as the radius of the circle tends to infinity, the integrals over the arcs AKJ and EDB tend to zeros; and the line $\gamma - i\infty, \gamma + i\infty$ can be transformed into the contour JHGFE, Figure 8. Hence the integral will be performed along the contour which begins from $-\infty$ in the lower half plane, passes around the branch point at the origin in the positive direction, and ends at $-\infty$ in the upper plane. This contour is denoted as $(-\infty, +0)$. Hence, the counter integration in Eq. (44) can be approximated as:

$$\theta(r, t) = \frac{Q_0}{2\pi r_b i \lambda} \int_{-\infty}^{0^+} e^{v^2 \alpha t} \frac{2K_0(rv)}{vK_1(r_b v)} dv \quad \text{Eq. 48}$$

In which $v = \sqrt{s/\alpha}$. That is the contour integral along the complex plane $\gamma - i\infty, \gamma + i\infty$ is reduced to areal integral along $(-\infty, +0)$. This makes the integration somewhat easier. To facilitate the integrand in Eq. (47), the modified Bessel function is approximated using:

$$\begin{aligned} K_n(z) = & (-1)^{n+1} \{ \ln(z/2) + \gamma \} I_n(z) \\ & + \frac{1}{2} (-1)^n \sum_{x=0}^{\infty} \frac{(z/2)^{n+2x}}{x! (n+x)!} \left[\sum_{m=1}^{n+x} m^{-1} \sum_{m=1}^x m^{-1} \right] \\ & + \frac{1}{2} \sum_{x=0}^{n-1} (-1)^x \left(\frac{z}{2} \right)^{-n+2x} \frac{(n-x-1)!}{x!} \end{aligned} \quad \text{Eq. 49}$$

Where n is any positive integer, and \ln is the modified Bessel function of the first kind of order n , and $\gamma = 0.57722 \dots$, is Euler's constant. Now, using some other typical integrals given in Carslaw and Jaeger [16], together with Eq. (49), Carslaw and Jaeger showed that the solution for the long-time scale can be approximated by:

$$\theta(r, t) = \frac{Q_0 r_b}{2\lambda} \left\{ \ln \frac{4\alpha t}{Cr^2} + \frac{r_b^2}{2\alpha t} \ln \frac{4\alpha t}{Cr^2} + \frac{1}{4\alpha t} \left[r_b^2 + r^2 - 2r_b^2 \ln \frac{r_b}{r} \right] + \dots \right\} \quad \text{Eq. 50}$$

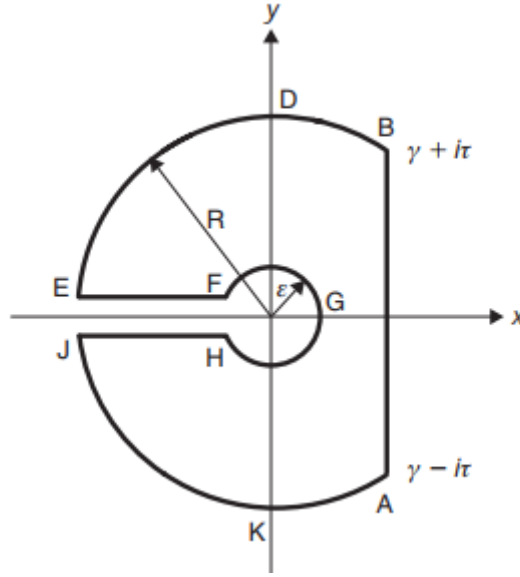


Figure 8: Contour path of the ICS model.

Note that Eq. (50) is equivalent to Eq. (39) for a line source emitting $2\pi r_b q_0$ units of heat per unit of time per unit of length. In this context, Ingersoll asserted that for a heat source of less than 50 mm in diameter, the infinite line source model can still produce accurate results. Beyond that, error occurs.

Ingersoll et al. [20] provided tabulated values of the integral in Eq. (45) for different values of Fourier's number, but limited to only four values of r/r_b . Philippe presented and utilized the solution given by Baudoin, who solved Eq. (43) using the Gaver-Stehfest numerical Laplace transform inversion algorithm, which yields:

$$\theta(r, t) = -\frac{q_0}{2\pi\lambda r_b} \sum_{j=1}^{10} \left[\frac{D_j}{j\mu_j} \frac{K_0(\mu_j r)}{K_1(\mu_j r_b)} \right] \quad \text{Eq. 51}$$

With

$$\mu_j = \sqrt{j \ln 2/\alpha t} \quad \text{Eq. 52}$$

$$D_j = \sum_{k=\text{int}((j+1)/2)}^{\min(j,5)} \frac{(-1)^{j-5} k^5 (2k)!}{(5-k)! (k-1)! k! (j-k)! (2k-j)!}$$

It can be noticed that modeling heat conduction in infinite and semi-infinite regions, and even by applying simplified physical assumptions such as small or large Fourier's numbers, or using numerical procedures for solving the semi-infinite integral in Eq. (45), it is still a formidable task. On the other hand, for a finite region, the solution can be obtained in terms of series summation, which converge relatively rapidly. In cylindrical coordinate system, for example, Yener and Kakac [19] have shown that the solution of the heat equation of a finite domain in the range $r_b \leq r \leq R$, subjected to a heat flux $q'(t)$ per unit length, is:

$$T(r, t) - T_0 = \frac{1}{\pi R^2} \sum_{n=1}^{\infty} e^{-\alpha \beta_n^2 t} \frac{J_0(\beta_n r) J_0(\beta_n r_b)}{J_1^2(\beta_n R)} \int_0^t e^{\alpha \beta_n^2 \tau} q'(\tau) d\tau \quad \text{Eq. 53}$$

where β_n is the positive roots of $J_0(\beta R) = 0$. In practice, in many of the currently utilized models, heat flux coming from the borehole heat exchanger is considered constant, i.e. $q'(t) = q'$. In this case, and by solving the integral of Eq. (53), the temperature distribution in the medium can be expressed as:

$$T(r, t) - T_0 = \frac{q'}{\pi \lambda R^2} \sum_{n=1}^{\infty} \frac{1 - e^{-\alpha \beta_n^2 t}}{\beta_n^2} \frac{J_0(\beta_n r) J_0(\beta_n r_b)}{J_1^2(\beta_n R)} \quad \text{Eq. 54}$$

Obviously, Eq. (54) is much more elegant and relatively easy to handle. Therefore, and in order to circumvent the hassle of solving infinite integrals involved in infinite regions, it is recommended, when possible, to terminate the far field distance at, say $r = R$, where it is known analytically or intuitively that heat flux generated by the source vanishes. That is, despite dealing with an infinite region, our region of interest is finite.

2.2.3 Finite line source model

The Finite Line Source model (FLS) approximates the borehole heat exchanger by a finite line constituting a series of point sources. The temperature in the soil is calculated by integrating the solution of the continuous point source case over the length of the borehole [7].

The temperature at point r in an infinite domain subjected to a constant heat flux, q_0 , is described as:

$$T(r, t) = \frac{q_0}{4\pi r \lambda} \operatorname{erfc}(r/2\sqrt{\alpha t}) \quad \text{Eq. 55}$$

In an infinitely thin layer, $d\xi$, the temperature variation due to total heat flux $q_0 d\xi$, can be described as:

$$dT(r, t) = \frac{q_0}{4\pi r \lambda \xi} \operatorname{erfc}(r/2\sqrt{\alpha t}) d\xi \quad \text{Eq. 56}$$

Imagine that we have many thin layers laid on top of each other and inserted in an infinite domain. Each layer is subjected to a point source at its origin, as shown in Figure 9. Points in the domain are subjected to an accumulated heat flow coming from all involved point heat sources. In this case, the temperature at a point $P(r, z)$ for instance, can be described by integrating Eq. (56) over the length of the point heat sources as:

$$T(r, z, t) = \frac{q_0}{4\pi\lambda} \int_0^L \frac{1}{r_1} \operatorname{erfc}(r_1/2\sqrt{\alpha t}) d\xi \quad \text{Eq. 57}$$

In which $r_1 = \sqrt{r^2 + (z - \zeta)^2}$, with ζ is any point along the line source (borehole).

Physically, the soil mass is semi-infinite and the surface temperature variation has significant influence on the soil temperature. To model the soil mass as a semi-infinite region in the z -direction, and impose a prescribed temperature at the ground surface, the method of images can be utilized [16]. This method was first introduced in the mathematical theory of electricity, and elegantly adopted to the solution of heat conduction in semi-infinite medium, where a constant temperature is imposed at the surface. The image has identical values as those in the original domain but opposite in magnitude. In this case, we have a source at point ζ and a sink at point $-\zeta$, Figure 9. Based on this technique, Eskilson [21] introduced the FLS model, expressed as:

$$T(r, z, t) - T_0 = \frac{q_0}{4\pi\lambda} \int_0^L \left[\frac{1}{r_1} \operatorname{erfc}\left(\frac{r_1}{2\sqrt{\alpha t}}\right) - \frac{1}{r_2} \operatorname{erfc}\left(\frac{r_2}{2\sqrt{\alpha t}}\right) \right] d\xi \quad \text{Eq. 58}$$

In which T_0 is the initial temperature, and

$$r_1 = \sqrt{r^2 + (z - \zeta)^2}, r_2 = \sqrt{r^2 + (z + \zeta)^2} \quad \text{Eq. 59}$$

This model is valid for the following condition:

$$5r_b^2/\alpha < t < t_s/10 \quad \text{Eq. 60}$$

Where t_s is the time when the steady-state condition has been reached. This time ranges between few hours to few years.

On the basis of this model, Claesson and Eskilson introduced the concept of what is known as the g-function. This function is a dimensionless function representing the temperature at the borehole wall, described as:

$$T_b - T_0 = \frac{q_0}{2\pi\lambda} g\left(\frac{t}{t_s}, \frac{r_b}{L}\right), t_s = \frac{L^2}{9\alpha} \quad \text{Eq. 61}$$

In which T_b is the borehole surface temperature, and t_s is a steady-state time scale. In the last two decades, and since the introduction of the Eskilson model in 1987, this model has been utilized intensively and seems to dominate the research works for ground source heat pumps, especially those dealing with analytical and semi-analytical procedures.

Claesson and Eskilson treated Eq. (61) numerically and analytically. Numerically, the temperature distribution in the soil mass due to a unit step heat pulse is calculated using the finite difference method. The response to multiple heat sources coming from different boreholes is calculated as a superposition of a series of step functions, such that:

$$T_b - T_0 = \sum_i \frac{\Delta q_i}{2\pi\lambda} g\left(\frac{t - t_i}{t_s}, \frac{r_b}{L}\right) \quad \text{Eq. 62}$$

These functions are calculated for various borehole geometry and configurations, and stored in the database of commonly utilized design and analysis software. The limitation of the numerical g-function is that it is only valid for a time greater than $L^2/9\alpha$. Analytically, Claesson and Eskilson gave two asymptotic approximations to the g-function, such that:

$$g\left(\frac{t}{t_s}, \frac{r_b}{L}\right) = \begin{cases} \ln\left(\frac{L}{2r_b}\right) + \frac{1}{2}\ln\left(\frac{t}{t_s}\right) & 5r_b^2/\alpha < t \leq t_s \\ \ln\left(\frac{L}{2r_b}\right) & t \geq L^2/9\alpha \end{cases} \quad \text{Eq. 63}$$

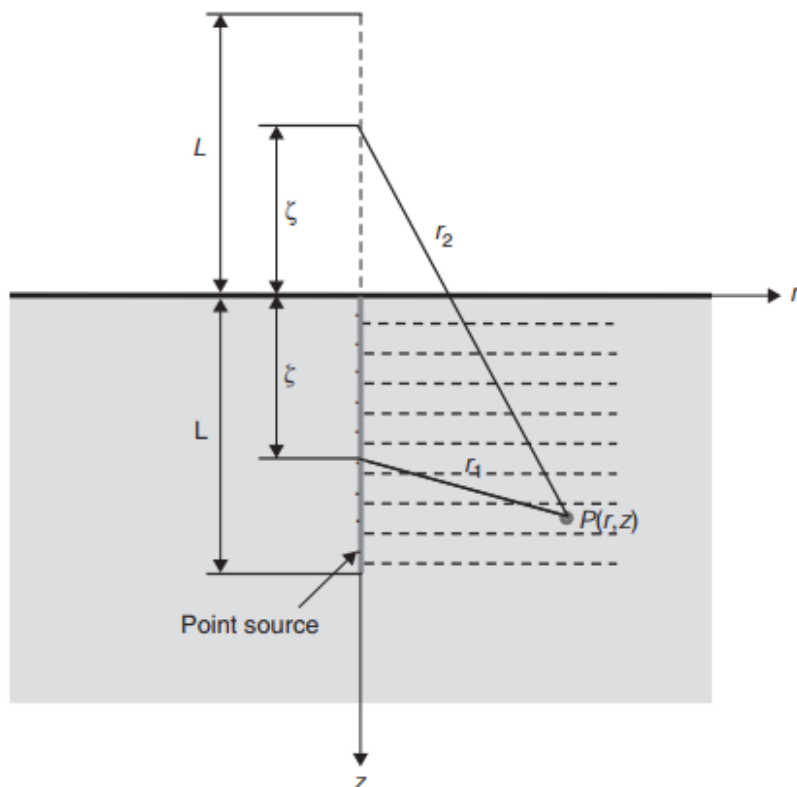


Figure 9: Finite line source model.

The concept of the g-function has received considerable interest from researchers in the field and soon after its introduction, several models with different complexity and computational efficiency have been introduced. Some authors suggested somewhat similar, non-dimensional g-function, defined as:

$$g(t, L') = \int_0^1 \left[\frac{1}{\tilde{r}_1} \operatorname{erfc} \left(\frac{\tilde{r}_1}{2\sqrt{F_0}} \right) - \frac{1}{\tilde{r}_2} \operatorname{erfc} \left(\frac{\tilde{r}_2}{2\sqrt{F_0}} \right) \right] dL' \quad \text{Eq. 64}$$

Where

$$\tilde{r}_1 = \sqrt{R^2 + (Z - L')^2}, \tilde{r}_2 = \sqrt{R^2 + (Z + L')^2}, F_0 = at/L^2 \quad \text{Eq. 65}$$

$$Z = z/L, L' = \zeta/L, R = r/L$$

However, this model does not really produce significant improvements. Lamarche and Beauchamp [22] derived a computationally more efficient g-function based on the continuous infinite line source model. After an elaborate mathematical manipulation, they arrived at a g-function of the form:

$$g(t^*, \beta) = \int_{\beta}^{\sqrt{\beta^2+1}} \frac{\operatorname{erfc}(\gamma z)}{\sqrt{z^2 - \beta^2}} dz - D_A - \int_{\sqrt{\beta^2+1}}^{\sqrt{\beta^2+4}} \frac{\operatorname{erfc}(\gamma z)}{\sqrt{z^2 - \beta^2}} dz - D_B \quad \text{Eq. 66}$$

In which

$$\begin{aligned} D_A &= \int_{\beta}^{\sqrt{\beta^2+1}} \operatorname{erfc}(\gamma z) dz & \text{Eq. 67} \\ &= \sqrt{\beta^2 + 1} \operatorname{erfc}(\gamma \sqrt{\beta^2 + 1}) - \beta \operatorname{erfc}(\gamma \beta) \\ &\quad - \frac{1}{\gamma \sqrt{\pi}} [e^{-\gamma^2(\beta^2+1)} - e^{-\gamma^2 \beta^2}] \end{aligned}$$

And

$$\begin{aligned} D_B &= \frac{1}{2} \left[\int_{\beta}^{\sqrt{\beta^2+1}} \operatorname{erfc}(\gamma z) dz + \int_{\sqrt{\beta^2+1}}^{\sqrt{\beta^2+4}} \operatorname{erfc}(\gamma z) dz \right] & \text{Eq. 68} \\ &= \sqrt{\beta^2 + 1} \operatorname{erfc}(\gamma \sqrt{\beta^2 + 1}) - \frac{1}{2} \beta \operatorname{erfc}(\gamma \beta) \\ &\quad + \sqrt{\beta^2 + 4} \operatorname{erfc}(\gamma \sqrt{\beta^2 + 4}) \\ &\quad - \frac{1}{\gamma \sqrt{\pi}} \left[e^{-\gamma^2(\beta^2+1)} - \frac{1}{2} (e^{-\gamma^2 \beta^2} + e^{-\gamma^2(\beta^2+4)}) \right] \end{aligned}$$

Where $t^* = t/t_s$ with t_s is as shown in Eq. (61), and $\gamma = 3/2\sqrt{2^*}$. For the detailed solution of the integrals in Eqs. (67) and (68) the reader is referred to Lamarche and Beauchamp [22]. Note that the first integral in Eq. (66) is convergent improper and need special numerical tools for solving it. Lamarche and Beauchamp provided information on the possible utilization of some available numerical tools, which are suitable for solving Eq. (66). They conducted numerical examples for two β values and showed that, despite the apparent intricate formulation, the CPU time needed for solving their g -function was ten of orders less than those of Eskilson and Zeng. Marcotte and Pasquier [23], solved this model in the frequency domain using the Fast Fourier Transform algorithm (FFT). They also extended the model to account for borehole inclination and borehole head located below the ground surface.

In contrast to ISL, FSL model allows for the calculation of the steady-state temperature, which can be described as:

$$T(r, z) - T_0 = -\frac{q_0}{4\pi\lambda} \int_0^L \left(\frac{1}{r_1} - \frac{1}{r_2} \right) d\zeta \quad \text{Eq. 69}$$

Solving Eq. (69) gives:

$$T(r, z) - T_0 = -\frac{q_0}{4\pi\lambda} \ln \left(\frac{\sqrt{r^2 + (z-L)^2} - (z-L)}{\sqrt{r^2 + (z+L)^2} + (z+L)} \cdot \frac{\sqrt{r^2 + z^2} + z}{\sqrt{r^2 + z^2} - z} \right) \quad \text{Eq. 70}$$

$$T(r, z) - T_0 = -\frac{q_0}{4\pi\lambda} \ln \left(\frac{\sqrt{r^2 + (z-L)^2} - (z-L)}{\sqrt{r^2 + (z+L)^2} + (z+L)} \cdot \frac{\sqrt{r^2 + z^2} + z}{\sqrt{r^2 + z^2} - z} \right) \quad \text{Eq. 71}$$

2.3 Semi-analytical model

In the present study, a transient short-time scale semi-analytical model developed by Benchabane's team (reported in [24, 25]) has been used. This model is mainly based on the ICS model presented above by Eq. (54). The specifications of this model reside on variable boundary conditions for both air and soil with time to make the sizing more accurate. The idea of the GRBM model is based on following steps [25]:

First, the soil and the EAHE pipe are subdivided into many layers. For each layer, the thickness of the disturbed soil and the radial soil temperature in the vicinity of the pipe were determined by the RBM model developed by Rouag et al. [24] to compute soil temperature and its thermal resistance. Subsequently, the total thermal resistance is calculated for the whole: air, pipe and soil. Finally, the determined parameters, which considered as constants for full current time step, are used to evaluate the air outlet temperature of the current layer. According to the GRBM model and for each step of time, all above steps are applied to each layer where the outlet air temperature of the j^{th} layer is considered as the inlet air temperature for the next layer, $(j+1)^{\text{th}}$ layer. This operation is repeated until the extremity of the EAHE pipe ($j = n_p$) as shown in Figure 10. The thermal resistance of soil for each layer of the previous time step serves as initialization for the next increment of time.

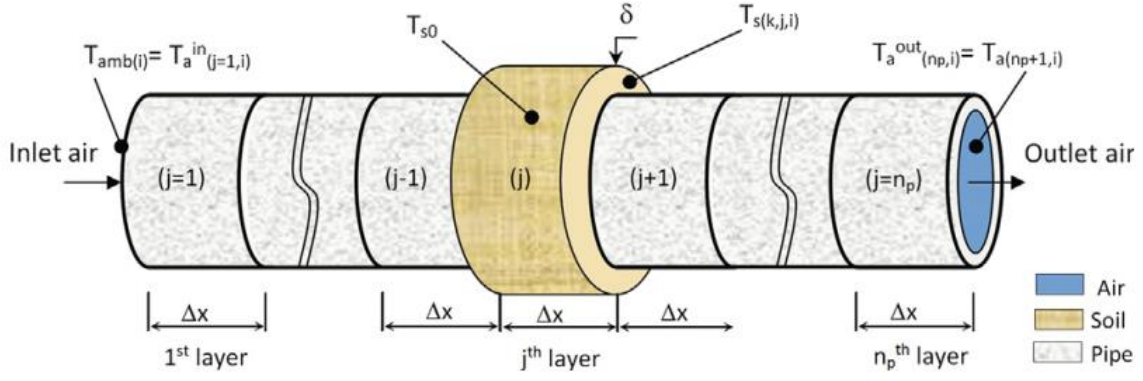


Figure 10: Scheme shows the subdivision of the EAHE pipe and the soil into many layers according to the GRBM model, where i , j and k are the indexes of time, layer and radius respectively.

2.3.1 Estimation of air temperature

The modelling of EAHE is established in such a way that the following assumptions are respected: (i) Soil around the heat exchanger is homogenous; (ii) Soil properties are isotropic and there is a perfect contact between the soil and the pipe; (iii) Air flow is uniform along the length of the buried pipes; (iv) Thermophysical properties of air are constants; (v) The pipe and the soil are subdivided into many layers of length (Δx) arranged in series; (vi) The air flow is considered one-dimensional as shown in Figure 10; (vii) In each layer, the heat flux between air and soil is assumed to be constant for the full current time step.

For a j^{th} layer, the energy balance is written by the following relation:

$$\dot{m}_a C p_a \frac{dT_a}{dx} = - \frac{(T_a - T_s)}{R_{tot}} \quad \text{Eq. 72}$$

Where T_a , $C p_a$ and \dot{m}_a are respectively the temperature, the specific heat capacity and the mass flow rate of air. Total thermal resistance, R_{tot} , is the sum of the thermal resistances of air, R_{cv} , pipe, R_p and R_s of the disturbed soil surrounding the j^{th} layer.

By solving analytically, the differential Eq. 72, the air outlet temperature of the j^{th} layer is given as follows [26]:

$$T_{a(j)}^{out} = (T_{a(j)}^{in} - T_{s0}) \exp\left(\frac{-\Delta x}{R_{tot} \dot{m}_a C p_a}\right) + T_{s0} \quad \text{Eq. 73}$$

For a given time, t_i , by taking the length of the layer $\Delta x = 1m$ and considering the inlet air temperature of the current j^{th} layer as the outlet air temperature of the previous $(j - 1)^{\text{th}}$ layer, the Eq. 73 can be written as:

$$T_{a(j+1,i)} = (T_{a(j,i)} - T_{s0}) \exp\left(\frac{-1}{\rho_a C p_a S V_a R_{tot(j,i)}}\right) + T_{s0} \quad \text{Eq. 74}$$

This last form of equation is well known solution for study-state EAHE in the literature [26].

2.3.2 Estimation of soil thermal resistance

The total thermal resistance between air, pipe and the soil surrounding j^{th} layer of the EAHE can be expressed by the following relation:

$$R_{tot} = R_{cv} + R_p + R_g \quad \text{Eq. 75}$$

Where the thermal resistance due to convective heat transfer between air and the inner surface of the pipe, R_{cv} , is calculated as:

$$R_{cv} = 1/(h_a 2\pi r_{int}) \quad \text{Eq. 76}$$

The air convective coefficient is:

$$h_a = Nu \cdot \lambda_a / d_{int} \quad \text{Eq. 77}$$

Where d_i is the inner diameter of the pipe. The Nusselt number for air flow inside the pipe is given by the Eq. (78):

$$Nu = 0.023 \cdot Re^{0.8} \cdot Pr^{0.3} \quad \text{Eq. 78}$$

Where Re and Pr are respectively Reynolds and Prandtl numbers are defined as:

$$Re = \frac{V_a \cdot d_H}{\nu_a} \quad \text{Eq. 79}$$

$$\text{Eq. 80}$$

$$Pr = \frac{\mu_a \cdot Cp_a}{\lambda_a}$$

The thermal resistance of the pipe, R_p , is given by the following equation:

$$R_p = \frac{\log\left(\frac{r_e}{r_{int}}\right)}{(2\pi\lambda_p)} \quad \text{Eq. 81}$$

The thermal resistance of the soil annulus, R_g , is given by the Eq. 79:

$$R_g = \frac{\log\left(\frac{r_\delta}{r_e}\right)}{(2\pi\lambda_s)} \quad \text{Eq. 82}$$

$$\text{Eq. 83}$$

$$r_\delta = r_e + \delta$$

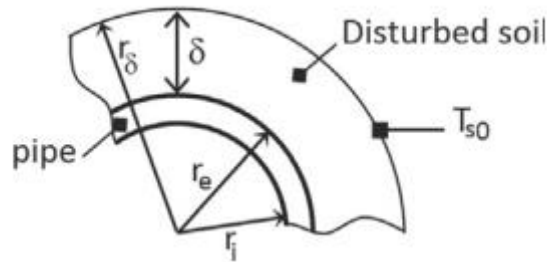


Figure 11: Scheme shows the disturbed soil thickness, δ , and the soil radius r_δ .

Where r_δ and δ are respectively the soil radius and the disturbed soil thickness (see Figure 11). Generally, the thermal resistance of the pipe, R_p and the thermal resistance due to the air convection in the pipe, R_{cv} are constants.

In GRBM model, the transient soil thermal resistance is considered in the prediction of the outlet air temperature by using the RBM model. The RBM model considers that the distance r_δ is not constant, but variable depending on the pipe diameter (r_e), the time of operating (t) and the diffusivity of the soil α_s [24]. For that, the analytical solution of the heat conduction equation (Eq. 84) in the soil is presented below. This equation is expressed in cylindrical coordinates at the j^{th} layer of the pipe and the surrounding soil considered as a semi-infinite hollow cylinder as shown in (Figure 12).

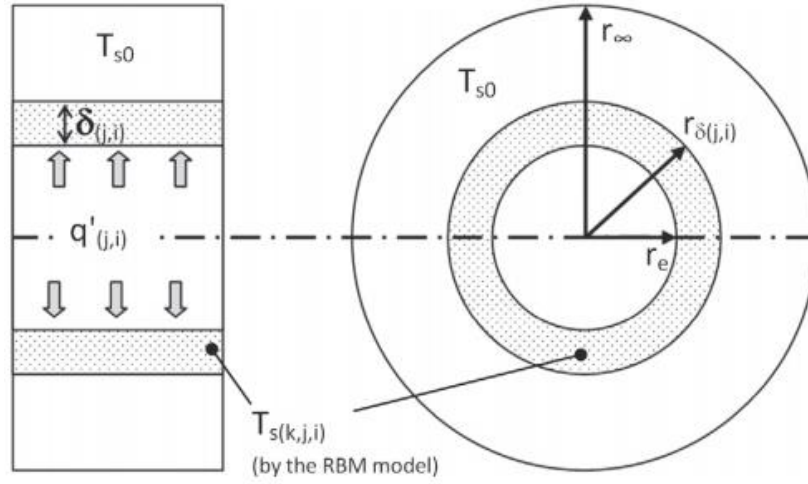


Figure 12: Axial and radial views of the pipe and the surrounding soil at j^{th} layer where the soil is considered as a semi-infinite hollow cylinder, where i, j and k are the indexes of time, layer and radius respectively.

$$\left\{ \begin{array}{l} \frac{1}{\alpha_s} \frac{\partial \theta}{\partial t} = \frac{\partial^2 \theta}{\partial r^2} + \frac{1}{r} \frac{\partial \theta}{\partial r} \quad \text{For } r \geq r_e \\ \text{With } \theta(r, 0) = 0 \\ \theta(r \rightarrow \infty, t) = 0 \\ \left[-\lambda_s \frac{\partial \theta}{\partial r} 2\pi r \right]_{r=r_e} = q' \end{array} \right. \quad \text{Eq. 84}$$

Where $u(k, j, i) = T_{s(k,j,i)} - T_{s0}$ with i, j and k are the indexes of time, layer and radius respectively. T_{s0} is the initial soil temperature and q' is the heat flux per unit length of the j^{th} layer for the i^{th} step of time.

$$\theta(k, j, i) = \frac{1}{\pi r_\infty^2} \sum_{n=1}^{\infty} e^{-\alpha_s \beta_n^2 t_i} \frac{J_0(\beta_n r_k) J_0(\beta_n r_e)}{J_1^2(\beta_n r_\infty)} \int_0^{t_i} e^{\alpha_s \beta_n^2 \tau} q'(\tau) d\tau \quad \text{Eq. 85}$$

where, β_n , are defined by the positive roots of $J_0(\beta_n r_\infty) = 0$, with $\beta_n = z_n / r_\infty$ and z_n are the positive roots of the Bessel functions $J_0(z) = 0$.

Referred to the assumption (vii), there are two ways to calculate the heat flux per unit length, $q'(\tau)$, in the Eq. 85:

- a) The heat flux, q' , is considered constant in the full step of time, Δt . In this case, the entity $q'(\tau)$ can be outputted directly from the integral of the Eq. 85. Thus, the soil temperature at the j^{th} layer can be written as:

$$T_s(k, j, i) - T_{s0} = \frac{q'(j, i)}{\pi \lambda_s r_\infty^2} \sum_{n=1}^{\infty} \frac{1 - e^{-\alpha_s \beta_n^2 t_i}}{\beta_n^2} \frac{J_0(\beta_n r_k) J_0(\beta_n r_e)}{J_1^2(\beta_n r_\infty)} \quad \text{Eq. 86}$$

For the current i^{th} step of time, the heat flux per unit length, $q'(j, i)$, is calculated by the soil thermal resistance, $R_s(j, i - 1)$, as:

$$q'(j, i) = \frac{(T_{a(j,i)} - T_{s0})}{R_{s(j,i-1)}} \quad \text{Eq. 87}$$

Where $T_{a(j,i)} = T_{a(j-1,i)}^{\text{out}}$

$$R_s(j, i - 1) = \frac{1}{2\pi \lambda_s} \log \left(\frac{r_{\delta(j,i-1)}}{r_e} \right) \quad \text{Eq. 88}$$

After substitution of Eqs. 87 and 88 in Eq. 86, the transient temperatures of soil surrounding the pipe can be written as:

$$T_s(k, j, i) = \frac{2(T_{a(j,i)} - T_{s0})}{r_\infty^2 \log \left(\frac{r_{\delta(j,i-1)}}{r_e} \right)} \sum_{n=1}^{\infty} \frac{1 - e^{-\alpha_s \beta_n^2 t_i}}{\beta_n^2} \frac{J_0(\beta_n r_k) J_0(\beta_n r_e)}{J_1^2(\beta_n r_\infty)} + T_{s0} \quad \text{Eq. 89}$$

b) The usual integral properties of Chasles' relation (Fiche et al.,[27]) were employed in the development. In this case the Eq. 85 becomes for the j^{th} layer:

$$\theta(k, j, m) = \frac{1}{\pi r_\infty^2} \sum_{n=1}^{\infty} \left(\frac{J_0(\beta_n r_k) J_0(\beta_n r_e) e^{-\alpha_s \beta_n^2 t_m}}{J_1^2(\beta_n r_\infty)} \left(\int_0^{t_1} e^{\alpha_s \beta_n^2 \tau} q'_{(j)}(\tau) d\tau \right. \right. \\ \left. \left. + \int_{t_1}^{t_2} e^{\alpha_s \beta_n^2 \tau} q'_{(j)}(\tau) d\tau + \dots + \int_{t_{m-1}}^{t_m} e^{\alpha_s \beta_n^2 \tau} q'_{(j)}(\tau) d\tau \right) \right) \quad \text{Eq. 90}$$

Or

$$\theta(k, j, m) = \frac{1}{\pi r_\infty^2} \sum_{n=1}^{\infty} \left(\frac{J_0(\beta_n r_k) J_0(\beta_n r_e) e^{-\alpha_s \beta_n^2 t_m}}{J_1^2(\beta_n r_\infty)} \sum_{i=1}^m \left(q'_{(i,j)} \int_{t_{i-1}}^{t_i} e^{\alpha_s \beta_n^2 \tau} d\tau \right) \right) \quad \text{Eq. 91}$$

Where the $(q'_{(i,j)}, i = 0, 1 \dots m)$ is the constant heat flux per unit of length of each i^{th} interval of time $[t_{i-1} - t_i]$ (assumption vii), which is calculated by the soil thermal resistance, $R_{s(j,i-1)}$ as:

$$q'_{(i,j)} \Big|_{t_{i-1}}^{t_i} = \frac{T_{a(j,i)} - T_{s0}}{R_{s(j,i-1)}} \quad \text{Eq. 92}$$

$$R_{s(j,i-1)} = \frac{1}{2\pi\lambda_s} \log\left(\frac{r_{\delta(j,i-1)}}{r_e}\right) \quad \text{Eq. 93}$$

Where $T_{a(j,i)} = T_{a(j-1,i)}^{out}$

As a result, the soil temperature of the j^{th} studied layer with variable inlet air temperature can be expressed in Eqs. (92) and (93) as:

$$\theta(k,j,m) = \frac{1}{\pi\lambda_s r_{\infty}^2} \sum_{n=1}^{\infty} \left(\frac{J_0(\beta_n r_k) J_0(\beta_n r_e) e^{-\alpha_s \beta_n^2 t_m}}{J_1^2(\beta_n r_{\infty})} \sum_{i=1}^m \left(\frac{q'_{(i,j)}}{\beta_n^2} [e^{\alpha_s \beta_n^2 \tau}]_{t_{i-1}}^{t_i} \right) \right) \quad \text{Eq. 94}$$

$$\begin{aligned} T_s(k,j,m) & \quad \text{Eq. 95} \\ &= \frac{2}{r_{\infty}^2} \sum_{n=1}^{\infty} \left(\frac{e^{-\alpha_s \beta_n^2 t_m}}{\beta_n^2} \frac{J_0(\beta_n r_k) J_0(\beta_n r_e)}{J_1^2(\beta_n r_{\infty})} \sum_{i=1}^m \left(\frac{T_{a(j,i)}}{\log\left(\frac{r_{\delta(j,i-1)}}{r_e}\right)} [e^{\alpha_s \beta_n^2 \tau}]_{t_{i-1}}^{t_i} \right) \right) \\ &+ T_{s0} \end{aligned}$$

Thus, both the transient soil temperatures surrounding the pipe and the soil radius r_d are estimated by using Eq. 89 in the case of constant inlet air temperature and by using Eq. 94 in the case of variable inlet air temperature.

2.3.3 Organizational chart of the GRBM model

For better understanding the calculation method based on the GRBM model, the organizational chart presented in Figure 13 summarizes the different steps described above. It should be noted that the soil thermal resistance and the soil temperature were estimated, for each layer, by using the subroutine RBM model. Furthermore, this subroutine depends on the inlet boundary condition (inlet fluid temperature) which implies the use of: (i) the Eq. 89 in the case of constant heat flux, (ii) or the Eq. 95 in the case of variable heat flux.

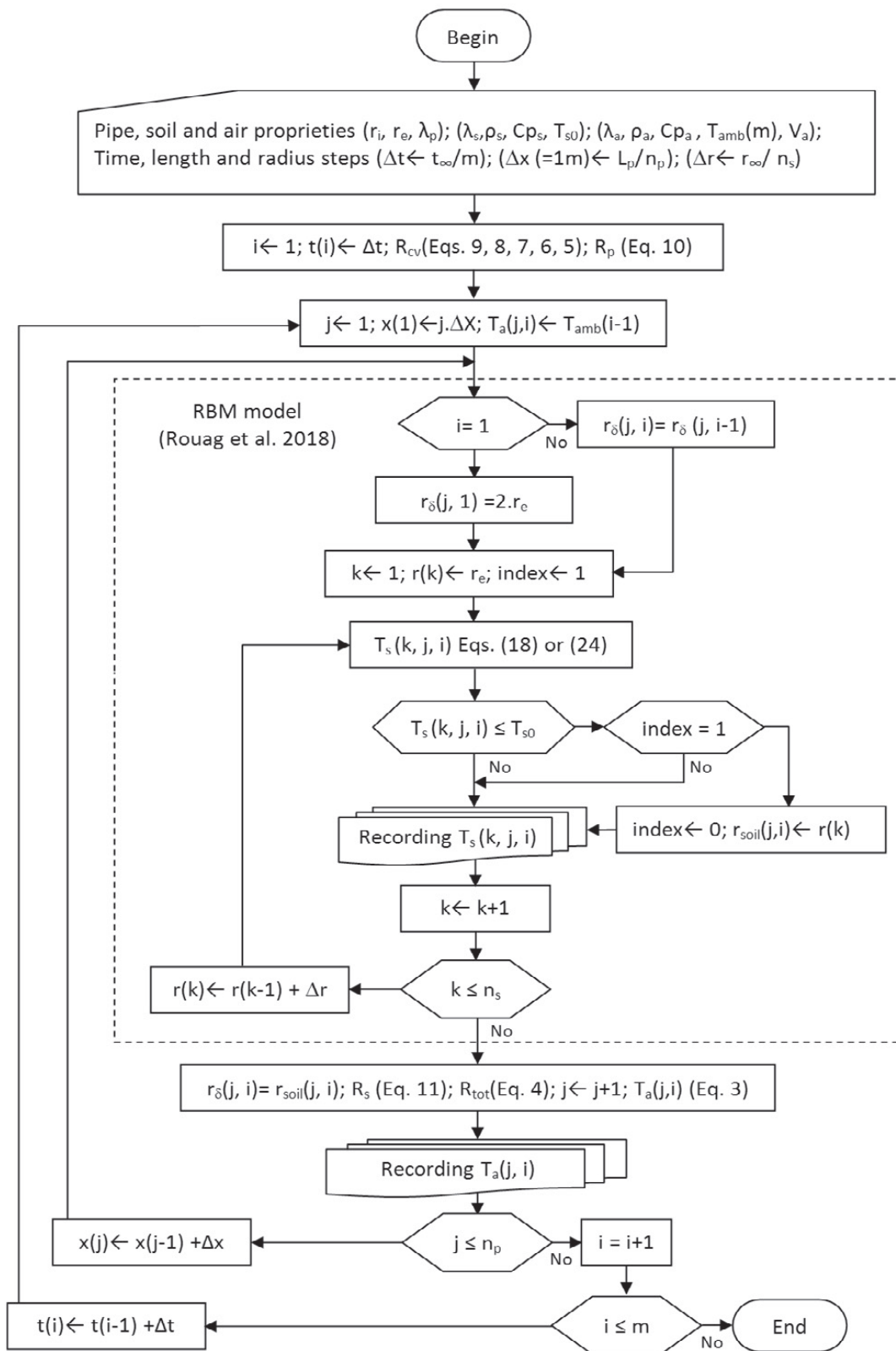


Figure 13: Detailed organizational chart of GRBM model.

2.4 CFD model

2.4.1 Governing equations

The governing equations for CFD (Computational Fluid Dynamics) are the continuity, the momentum and the energy equations. These equations for incompressible flow are respectively given by:

$$\frac{\partial u_i}{\partial x_i} = 0 \quad \text{Eq. 96}$$

$$\rho \frac{\partial u_i}{\partial t} + \rho u_j \frac{\partial u_i}{\partial x_j} = -\frac{\partial p}{\partial x_i} + \frac{\partial}{\partial x_j} (\tau_{ij}) \quad \text{Eq. 97}$$

$$\frac{\partial(\rho T)}{\partial t} + \nabla \cdot (u_j \rho T) = \nabla \cdot (k \cdot \nabla T) + S_T \quad \text{Eq. 98}$$

Where u_i denotes the i^{th} velocity component, p is the pressure, ρ is the fluid density, T is the fluid temperature, k is thermal conductivity, S_T is an additionally volumetric heat energy due to viscosity and τ_{ij} is viscous stress tensor. For Newtonian fluid, it can be defined as:

$$\tau_{ij} = 2\mu s_{ij} \quad \text{Eq. 99}$$

Where μ is the molecular viscosity and s_{ij} is the strain-rate tensor defined as:

$$s_{ij} = \frac{1}{2} \left(\frac{\partial u_i}{\partial x_j} + \frac{\partial u_j}{\partial x_i} \right) \quad \text{Eq. 100}$$

2.4.2 Turbulence modeling approaches

Turbulent flows are characterized by fluctuating velocity fields. These fluctuations mix transported quantities such as momentum, energy, and species concentration, and cause the transported quantities to fluctuate as well. Since these fluctuations can be of small scale and high frequency, they are too computationally expensive to simulate directly in practical engineering calculations. Instead, the instantaneous (exact) governing equations can be time-

averaged, ensemble-averaged, or otherwise manipulated to remove the small scales, resulting in a modified set of equations that are computationally less expensive to solve. However, the modified equations contain additional unknown variables, and turbulence models are needed to determine these variables in terms of known quantities [28].

2.4.2.1 Large eddy simulation (LES)

Large eddy simulation (LES) provides an alternative approach in which the large eddies are calculated in a time-dependent simulation that uses a set of “filtered” equations. Filtering is essentially a manipulation of the exact Navier-Stokes equations to remove only the eddies that are smaller than the size of the filter, which is usually taken as the mesh size. The idea was derived from Kolmogorov's theory [29, 30], which assumes that the large eddies of the flow are dependant on the geometry while the smaller scales are more universal. The filtering process creates additional unknown terms that must be modeled in order to achieve closure. Statistics of the mean flow quantities, which are generally of most engineering interest, are gathered during the time-dependent simulation. The attraction of LES is that, by modeling less of the turbulence (and solving more), the error induced by the turbulence model will be reduced. Different sub-grid scale models are available in the literature, such as Smagorinsky model [31], Algebraic Dynamic model [32], Localized Dynamic model [33], WALE (Wall-Adapting Local Eddy-viscosity) model [34] and Dynamic Global-Coefficient model [35].

In contrast to RANS, where the computational cost is only weakly dependent on Re , the computational cost of LES scales roughly with Re^2 [36]. Near solid boundaries, where boundary layers are present, LES is extremely expensive because it requires refinement in three directions, whereas RANS only requires refinement in the direction normal to the wall.

2.4.2.2 Statistical approach

Because turbulence consists of random fluctuations of the various flow properties, the statistical approach can be used. This approach is mainly based on the procedure introduced by Reynolds [37], in which all quantities are expressed as the sum of mean and fluctuating quantities [38]. The Reynolds-averaged Navier-Stokes (RANS) equations represent transport equations for the mean flow quantities only, with all the scales of the turbulence being modeled. The approach of permitting a solution for the mean flow variables greatly reduces the

computational effort. Therefore, this approach is currently the most commonly used CFD approach.

2.4.3 Reynolds averaged equations

For an incompressible flow, the RANS equations can be written as:

$$\frac{\partial \bar{u}_i}{\partial x_i} = 0 \quad \text{Eq. 101}$$

$$\rho \frac{\partial \bar{u}_i}{\partial t} + \rho \bar{u}_j \frac{\partial \bar{u}_i}{\partial x_j} = -\frac{\partial p}{\partial x_i} + \frac{\partial}{\partial x_j} (\bar{\tau}_{ij} - \overline{\rho u'_i u'_j}) \quad \text{Eq. 102}$$

$$\bar{\tau}_{ij} = 2\mu \bar{s}_{ij} \quad \text{Eq. 103}$$

$$\bar{s}_{ij} = \frac{1}{2} \left(\frac{\partial \bar{u}_i}{\partial x_j} + \frac{\partial \bar{u}_j}{\partial x_i} \right) \quad \text{Eq. 104}$$

Eq. (104) is usually referred to as the Reynolds-Averaged Navier-Stokes equation. The quantity $(-\overline{\rho u'_i u'_j})$ is known as the Reynolds-stress tensor, we denote it by T_{ij} , thus:

$$T_{ij} = -\overline{\rho u'_i u'_j} \quad (1)$$

2.4.4 Closure problem

Because T_{ij} is a symmetric tensor ($T_{ij} = T_{ji}$), it has six independent components. Hence, six unknown quantities have been produced as a result of Reynolds averaging. However, no additional equations were gained. The system of equations is not yet closed. To close the system, additional equations are needed.

2.4.5 Boussinesq hypothesis

To model the Reynolds stresses in terms of mean flow quantities, the Boussinesq hypothesis [39, 40] is commonly used. This hypothesis assumes that the Reynolds stress is related linearly to the mean strain-rate tensor as in a laminar flow. The proportional factor is

the eddy viscosity. The Boussinesq hypothesis for an incompressible flow can be written as [41]:

$$\tau_{ij} = 2\mu_t \bar{s}_{ij} - \frac{1}{2} \rho k \delta_{ij} \quad \text{Eq. 105}$$

where μ_t is the eddy viscosity, δ_{ij} is the Kronecker symbol and k is the turbulent kinetic energy defined as:

$$k = \frac{1}{2} (\overline{u'_i u'_i}) \quad \text{Eq. 106}$$

2.4.6 Turbulence model: k - ϵ model

Several turbulence models are available in the literature to close RANS equations. In this study, the standard k - ϵ model [42] which is the most widely used turbulence model in the CFD community due to its simplicity and robustness has been used. This model involves transport equations for the turbulent kinetic energy (k) and its dissipation rate (ϵ).

In the standard k - ϵ model, the turbulent (or eddy) viscosity is calculated by combining k and ϵ as follows:

$$\mu_t = \rho C_\mu \frac{k^2}{\epsilon} \quad \text{Eq. 107}$$

The turbulent kinetic energy k and its dissipation rate ϵ are obtained from the following transport equations:

$$\frac{\partial(\rho k)}{\partial t} + \frac{\partial(\rho k u_i)}{\partial x_i} = \frac{\partial}{\partial x_j} \left[\left(\mu + \frac{\mu_t}{\sigma_k} \right) \frac{\partial k}{\partial x_j} \right] + G_k - \rho \epsilon \quad \text{Eq. 108}$$

and

$$\frac{\partial(\rho \epsilon)}{\partial t} + \frac{\partial(\rho \epsilon u_i)}{\partial x_i} = \frac{\partial}{\partial x_j} \left[\left(\mu + \frac{\mu_t}{\sigma_\epsilon} \right) \frac{\partial \epsilon}{\partial x_j} \right] + C_{1\epsilon} \frac{\epsilon}{k} G_k - C_{2\epsilon} \rho \frac{\epsilon^2}{k} \quad \text{Eq. 109}$$

The production of turbulent kinetic energy G_k is modeled as:

$$G_k = -\overline{\rho u'_i u'_j} \frac{\partial u_j}{\partial x_i} \quad \text{Eq. 110}$$

Where the model constants are [\[42\]](#):

$$C_{1\epsilon} = 1.44, C_{2\epsilon} = 1.92, C_\mu = 0.09, \sigma_k = 1.0, \sigma_\epsilon = 1.3 \quad \text{Eq. 111}$$



Chapter **III**

*Numerical Modeling and
Implementation*



Chapter 3

Numerical Modeling and Implementation

3.1 Temperature of the ground: Kusuda equation

Firstly, we have validated the Kusuda equation (Eq. (14) in previous chapter) using experimental data conducted by Badache et al., [15], which they are measured the daily ground temperature in Varennes (Canada) from February to November 2014. Twenty-four 24 calibrated thermocouples (T type) were used in their experimental for determining the variation of soil temperature at different depths. The implemented subroutine in MATLAB and the used parameters are presented below. It is important to note that these parameters (Mean, Tamb, tshift) are given from meteorological data (Tmin and Tmax) at the Varennes region.

```
as=0.0948;tshift=84;Tmean=9.1262;Tamp=8.9180;w=2*pi/365;delta=
sqrt((2*as)/w);
z=linspace(0,30,30);t=linspace(0,365,365);
for j=1:length(t)
for i=1:length(z)
    Tk(i,j)= Tmean+Tamp.*exp(-z(i)./delta).*cos(w.*t(j)-
tshift-(z(i)./delta));
end
end
```

Figure 14 presents the comparison between measured and predicted ground temperature at depths 1 m, 8.5 m, 16 m, and 26 m at Varennes for the period from February 4th to November 25th, 2014. From this figure it can be seen that the measured and calculated ground temperature are in good agreements. The undistributed temperature at the Varennes is around 9.5 °C. It has been observed that Kusuda equation can predict very well the undistributed temperature of the ground.

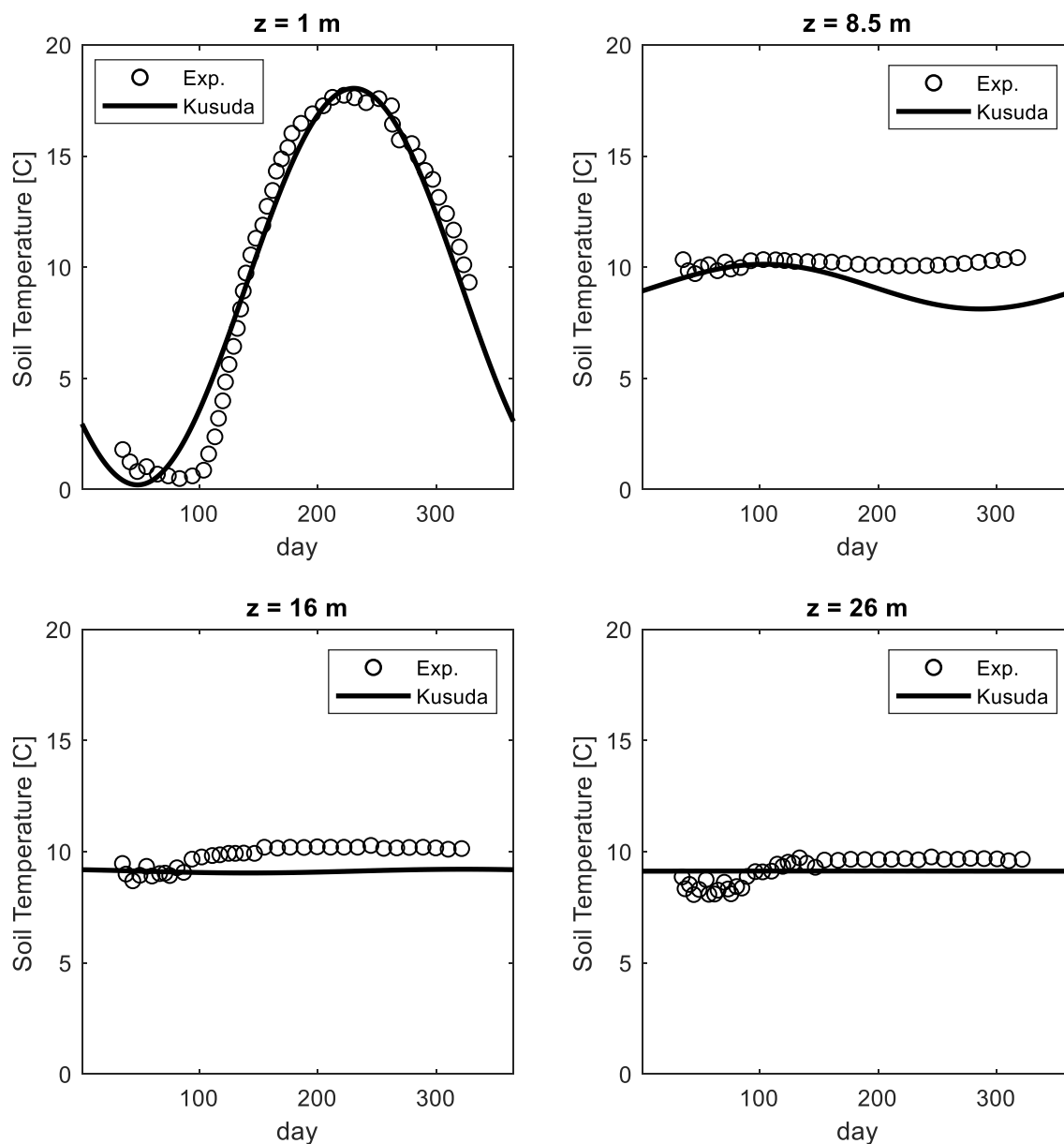


Figure 14: Measured and predicted ground temperature at depths 1 m, 8.5 m, 16 m, and 26 m at Varennes for the period from February 4th to November 25th, 2014.

3.2 Implementation of the analytical models

3.2.1 Calculation steps

To adapt the analytical (ICS, ILS and FLS) model, we used the methodology of Fontaine [43], which was able to implement the FLS model for horizontal geothermal heat exchangers. Same methodology with some modifications has been used. Here are the steps to follow to arrive at the final soil temperature and the temperature of the fluid at the outlet:

1. Calculate the resistance of the ground (R_g), the resistance of the pipe (R_p) and the characteristic thermal length (L_t) using the steady-state equations for horizontal pipes of Claesson and Dunand [44]. R_g and R_p are calculated using Eq. (81) and Eq. (82) respectively (presented in the previous chapter). L_t is calculated as: $L_t = (R_g + R_p) \cdot m_a \cdot Cp_a$;
2. Separate the pipe (regardless of its layout) into a series of n segments connected to each other. You don't have to be very tall to have good accuracy. For example, about twenty segments for a pipe with a length of 200 m is more than sufficient;
3. Compute the local heat flux in each segment using:

$$q'(x,t) = \frac{q(x,t)}{x} = \left((Tin(t)) \cdot \frac{\exp\left(-\frac{x}{L_t}\right)}{R_s + R_p} \right);$$

4. Calculate the pipe temperature using analytical solutions presented in the previous chapter; for ILS Eq. (33), for ICS Eq. (54) and for FLS Eq. (58).
5. knowing the average temperature at the wall of the pipe on each segment, calculate the average temperature of the fluid T_f for all segments with $T_f(x, t) = T_p(x, t) + (Tin(t) - T_p(x, t)) \times \exp(-x/(m_a \cdot cp_a \cdot R_p))$;

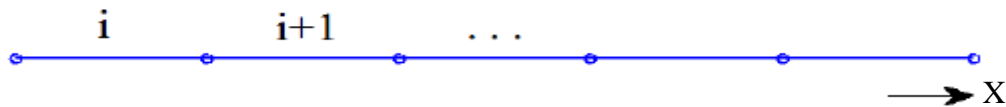


Figure 15: Representation of the EAHE separated into segments used in analytical IFS, ICS and FLS models.

3.2.2 Calculation subroutine

The implementation of the studied analytical solutions (ILS, ICS and FLS models) has been programmed using MATLAB software. The main subroutines of calculation for each model are presented below. The first step is to read data; the fluid proprieties ($m_a, Cp_a, Tin(t)$), the heat exchanger and the pipe proprieties ($L, r_i, r_e, k_p, k_g, R_p, R_g$), and the undistributed soil temperature T_0 , this latter can be obtained using Kusuda equation.

3.1.2.1 ILS model implementation

```
for j=1:length(t) % time;
```

```

for i=1:length(dx) % position;
q(i,j) = ((Tin(j))*exp(-i/(ma*cpa*(Rg+Rp)))/(Rg+Rp))/i;
Tp(i,j)=T0+(q(i,j)/(2*pi*kg))*expint(re^2/(4*alphas*t(j)));
Tf(i,j)=Tp(i,j)+(Tin(j)-Tp(i,j))*exp(i/(ma*cpa*Rp));
end
end

```

3.1.2.2 ICS model implementation

```

A=0; % initial value for sommation;
for j=1:length(t) % time;
    for i=1:length(dx) % position;
q(i,j) = ((Tin(j))*exp(-i/(ma*cpa*(Rg+Rp)))/(Rg+Rp))/i;
        for n=1:100 % analytical Bassel function;
aa(n)=pi.*(4.*n-1);J0z(n)=(aa(n)/4).*(1+(2./aa(n).^2)-
62/(3.*aa(n).^4)+7558./(15.*aa(n).^6));
Bn(n)=(J0z(n))./R; % R is the radius of the EAHE;
A=((1-exp(-
alpha_g.*(Bn(n).^2).*t(j)))/(Bn(n).^2)).*(besselj(0,Bn(n).*d
x(i)).*besselj(0,Bn(n).*re)./besselj(1,Bn(n).*R).^2)+A ;
        end % alpha_g is the soil thermal diffusivity;
Tp(i,j)=T0+(q(i,j)/(pi*kg*R^2)).*A;
        Tf(i,j)=Tp(i,j)+(Tin(j)-Tp(i,j))*exp(-i/(ma*cpa*Rp));
A=0;
    end
end

```

3.1.2.3 FLS model implementation

```

A=0; % initial value for sommation;
dh=[0:1:L]; % integration vector;
for j=1:length(t) % time;
    for i=1:length(dx) % position;
q(i,j) = ((Tin(j))*exp(-i/(ma*cpa*(Rg+Rp)))/(Rg+Rp))/i;
A(i,j)=trapz(dh,(erfc(real(sqrt(re^2+((dx(i))-
dh))./2*sqrt(t(j))))/(sqrt(re^2+((dx(i))-dh).^2)))+...

trapz(dh,(erfc(real(sqrt(re^2+((dx(i))+dh))./2*sqrt(t(j))))/(
sqrt(re^2+((dx(i))+dh).^2))));
Tp(i,j)=T0+(q(i,j)/(4*pi*kg)).*A(i,j);
        Tf(i,j)=Tp(i,j)+(Tin(j)-Tp(i,j))*exp(-i/(ma*cpa*Rp));
    end
end

```

3.3 Implementation of the semi-analytical model

In this stud, both semi-analytical RBM and GRBM models has been programmed in MATLAB. The RBM model computes the soil temperature, while the GRBM model calculates the fluid temperature based on the RBM model.

3.3.1 RBM model implementation

```

t=0;r=r1;rd=rsoil;rindex=1;
for j=1:time_inf
    t=t+3600;
        for i=1:n_division
            r=r+dr;
            A=0;
            %%
            for n=1:40
                aa(n)=pi*(4*n-
1);J0z(n)=(aa(n)/4)*(1+(2/aa(n)^2)-
62/(3*aa(n)^4)+7558/(15*aa(n)^6));
                Bn(n)=(J0z(n))/rinf;
                A=A+(1-exp(-
alpha*(Bn(n)^2)*t))/(Bn(n)^2)*(besselj(0,Bn(n)*r)*besselj(0,Bn
(n)*r1))/(besselj(1,Bn(n)*rinf)^2);
            end

            T(i)=(2*(Tf-
T0)./(log(rd/r1).*rinf^2))*A)+T0;
            if T(i)==(T0)
                if rindex==1
                    rsoil=r;
                    rd=r;
                    rindex=0;
                else
                    if r < rinf
                        TT(i)=T(i);
                    else
                        if t <= tinf
                            rd=rsoil;
                        end
                    end
                end
            end
        end
    end

    TT(i,j)=T(i);
end

    r=r1-dr;
    rindex=1;

```

end

For validation of the RBM model we used the results of the finite difference method obtained by Barkat et al., [45] and presented by Rouag et al., [24].

Tableau 1: Input parameters for the comparative verification with Barakat et al.

Soil parameters	Soil thermal capacity (J/(kg K))	1995.4
	Soil thermal conductivity (W/(m K))	1.74
	Soil Density (kg/m ³)	1868
	Soil initial temperature (°C)	25
Pipe parameters	Pipe surface temperature (°C)	40
	Pipe diameter (m)	0.3
Duration of operation	Time (h)	12

Table 1 gives the detailed input parameters of soil, pipe and time functioning used in the numerical simulation of Barakat et al. [45], (reported from Rouag et al., [24]) . Figure 16 shows that there is a good agreement between the soil radial temperature predicted by the RBM model with the numerical results of Barakat et al. After 12 h of operation, the soil reaches to the initial temperature at range of 0.5m from the pipe surface.

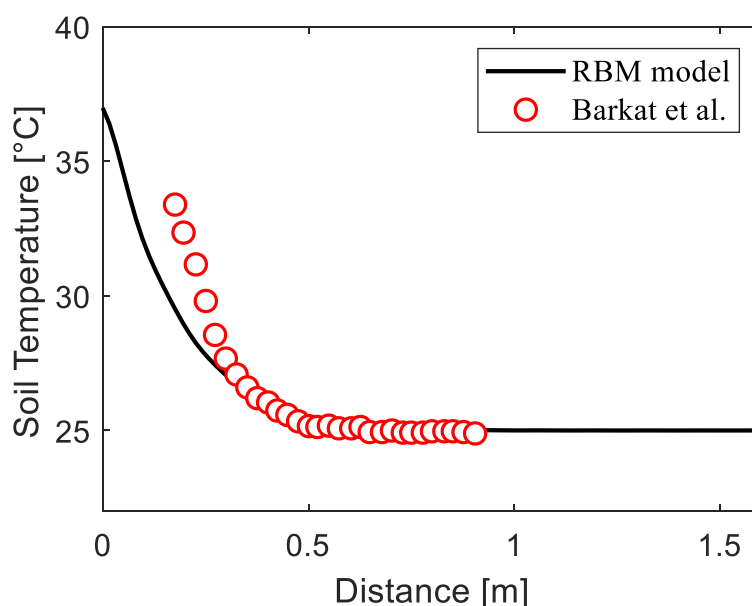


Figure 16: Reverification of the RBM model with the work of Barakat et al. [45].

3.3.2 GRBM model implementation

```
t=0;r=r1;rd=rsoil;rindex=1;dx=1;
for j=1:time_inf
    t=t+3600;
```

```

for k=2:47
    x=k*dx;
    T_a(1,j)=T_amp(j);
        for i=1:n_division
            r=r+dr;
            A=0;
            %%
            for n=1:40
                aa(n)=pi*(4*n-
1); J0z(n)=(aa(n)/4)*(1+(2/aa(n)^2)-
62/(3*aa(n)^4)+7558/(15*aa(n)^6));
                Bn(n)=(J0z(n))/rinf;
                A=A+(1-exp(-
alpha*(Bn(n)^2)*t))/(Bn(n)^2)*(besselj(0,Bn(n)*r)*besselj(0,Bn
(n)*r1))/(besselj(1,Bn(n)*rinf)^2);
                    end

                    T(i)=(2*(T_f(j)-
T0)./(log(rd/r1).*rinf^2))*A)+T0;
                    if T(i)==(T0)
                        if rindex==1
                            rsoil=r;
                            rd=r;
                            rindex=0;
                        else
                            if r < rinf
                                TT(i)=T(i);
                            else
                                if t <= tinf
                                    rd=rsoil;
                                end
                            end
                        end
                    end
                end
            end

            TT(i,j)=T(i);
        end

        r=r1-dr;
        rindex=1;

Rs=(log(rd/r1))/(2*pi*lambda);% eq11
R_tot=Rcv+Rp+Rs;
b=exp(-1/(rho_a*cp_a*S*V_a.*R_tot));

T_a(k,j)=(T_a(k-1,j)-T0).*b+T0 ;

end
end

```

3.4 CFD modeling

As we have seen in the previous chapter, the mathematical model of the turbulent flows around through the EAHE, which is described by the Navier-Stokes equations, is very complex. To solve such a model, an already existing CFD software is required. Certain conditions are required in the software to be exploited: (recognized worldwide, reliability, flexibility...). The ANSYS FLUENT (CFD software) meets all these criteria. In this study the ANSYS FLUENT 2020 R1 academic version (for students) has been used for CFD simulation of the EAHE.

3.4.1 Geometry design

In this study, the geometry of the EAHE represents as a cylindrical pipe of length L and diameter D . The soil surrounding of this pipe has a cylindrical shape of diameter equals the diameter of the EAHE, D . The computational domain contains two main parts: the first one is related to the bare soil for initial conditions calculations and the second one is devoted to the ground heat exchanger. The resolution of equations for both parts together is based on an iterative mathematical procedure using ANSYS FLUENT.

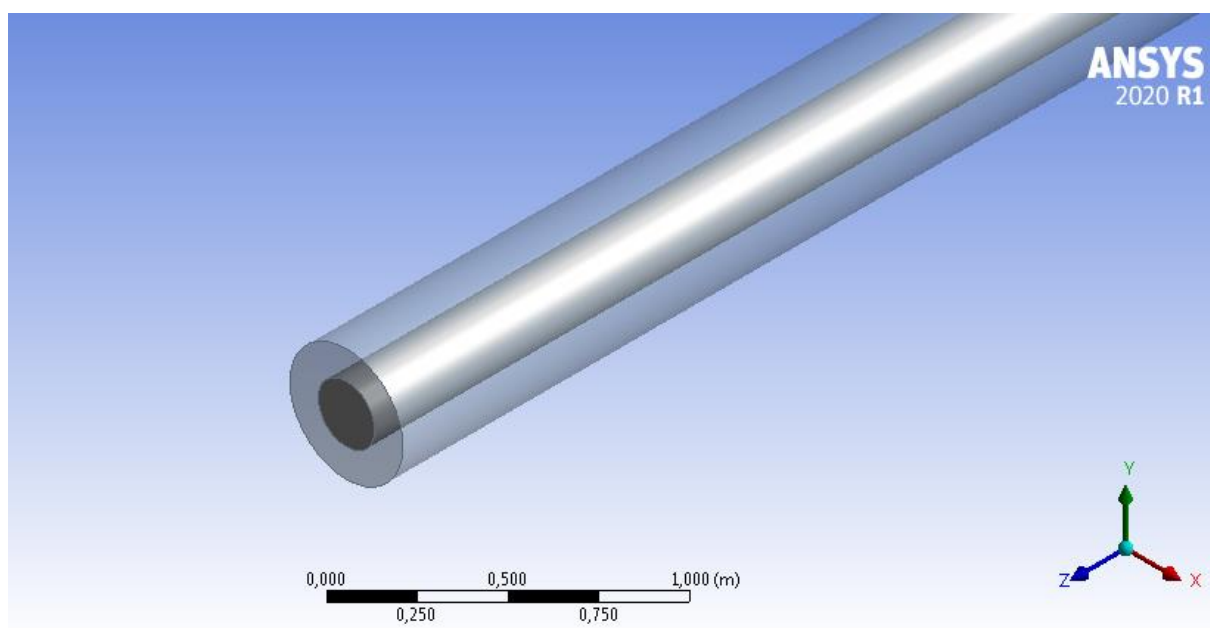


Figure 17: Geometry of the EAHE and surrounding soil in ANSYS Workbench.

3.4.2 Mesh generation

The mesh generation methodology used in this study is based on the work of Michel et al., [46], whose recommended to devise the fluid domain in the pipe into size of $4 \times D/17$, and the solid domain of $12 \times D/17$ size, where D is the heat exchanger diameter. This led to our mesh contains about 300,000 elements in the full computational domain. In addition, prismatic layers have been constructed near the pipe wall using the inflation technique for taking into account the wall-fluid boundary layer interaction.

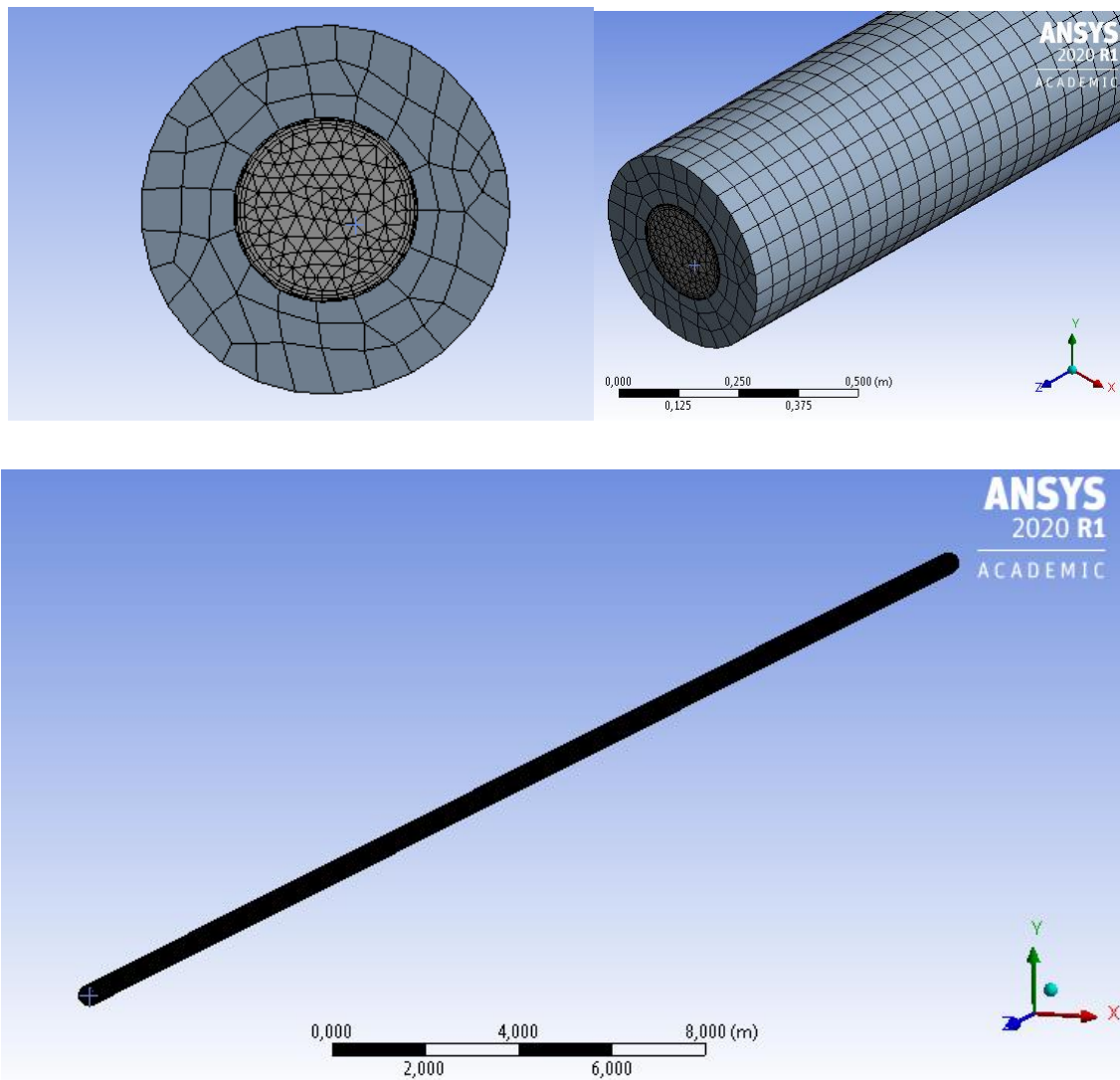


Figure 18: Mesh generation using ANSYS Workbench.

3.4.3 Discretization of equations

The ANSYS FLUENT software is based on the finite volume method to solve the governing equations of fluid flows. A brief description of the general steps in the solver and algorithms used for solving the Navier-Stokes equations will be presented in this section. The Finite Volume Method (FVM) is among of widely used methods to discretization of the equations in CFD codes. This method which firstly published in 1972 by Patankar and Spalding [47, 48] uses a control-volume-based technique to convert the governing equations to algebraic equations that can be solved numerically. This control volume technique consists of integrating the governing equations about each control volume, yielding discrete equations that conserve each quantity on a control-volume basis. Discretization of the governing equations can be illustrated most easily by considering the steady-state conservation equation for transport of a scalar quantity ϕ . This is demonstrated by the following equation written in integral form for an arbitrary control volume V as follows:

$$\oint \rho \phi \vec{v} \cdot d\vec{A} = \oint \Gamma_{\phi} \nabla \phi \cdot d\vec{A} + \int_V S_{\phi} dV \quad \text{Eq. 112}$$

Where: ρ is the density;

\vec{v} is the velocity vector ($u\vec{i} + v\vec{j} + w\vec{k}$);

\vec{A} is surface area vector;

Γ_{ϕ} is diffusion coefficient for variable ϕ ;

$\nabla \phi$ is gradient of ϕ , [$\nabla \phi = (\partial \phi / \partial x)\vec{i} + (\partial \phi / \partial y)\vec{j} + (\partial \phi / \partial z)\vec{k}$];

S_{ϕ} is source term of ϕ per unit volume.

For illustration the way of discretization of equations using the control-volume-based technique, as an example, the discretization of equation for a 2-D triangle cell shown in Figure 19 is given by [49, 50]:

$$\sum_i^{Nfaces} \rho_i \phi_i \vec{v}_i \cdot \vec{A}_i = \sum_i^{Nfaces} \Gamma_\phi (\nabla \phi)_n \cdot \vec{A}_i + S_\phi V \quad \text{Eq. 113}$$

Where: $Nfaces$ is the number of faces enclosing cell;

ϕ_i is the value of ϕ convected through face i ;

$\rho_i \vec{v}_i \cdot \vec{A}_i$ is the mass flux through the face;

\vec{A}_i is the area of face i , $|A| = |A_x \vec{i} + A_y \vec{j} + A_z \vec{k}|$;

$(\nabla \phi)_n$ is the magnitude of $\nabla \phi$ normal to the face i ;

V is the cell volume.

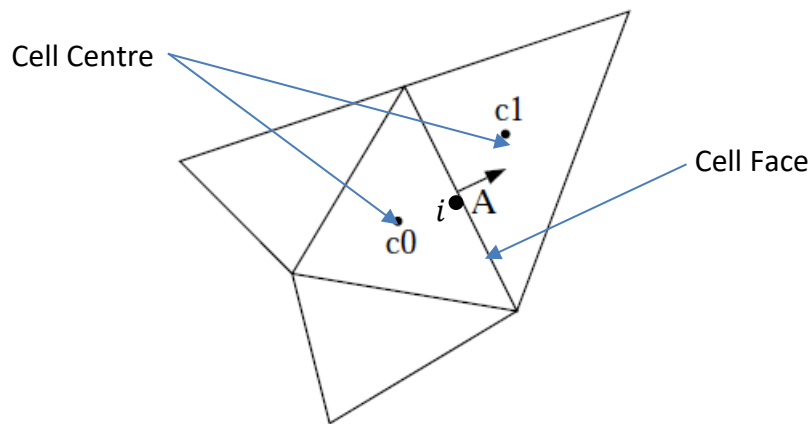


Figure 19: Example of a 2-D triangular control volume.

The equations solved by the solver take the same general form as the one given above and apply readily to three-dimensional for each flow variables. The discrete values of the scalar ϕ are stored at the cell centers (c_0 and c_1 in Figure 19). However, face values ϕ_i are required for the convection terms in Eq. (113) and must be interpolated from the cell center values.

The most obvious way of obtaining cell-face values is to use linear interpolation between cell centers. This technique known as the central differencing scheme. For the convected velocities in the convection term, this treatment will result in erroneous results [51]. A well-known technique solution the so-called upwind scheme for getting around these difficulties has been developed.

Upwinding means that the face value ϕ_i is derived from quantities in the cell upstream, or «upwind», relative to the direction of the normal velocity v_n in Eq. (113). Several schemes exist; the most used are the first-order upwind and second-order upwind. These two mostly used schemes are described in the following section.

3.4.3.1 First-order upwind

In first-order upwind scheme, quantities at cell faces are determined by assuming that the cell-center values of any field variable represent a cell-average value and hold throughout the entire cell; the face quantities are identical to the cell quantities. Thus, when first-order upwinding is selected, the face value ϕ_i is set equal to the cell-center value of ϕ in the upstream cell. Among of advantages of this scheme it's easily to converge, however, it less accurate than second-order upwind scheme [52]. The first-order upwind scheme is limited for the simple flows that are aligned with the mesh especially where the numerical diffusion are low [50].

3.4.3.2 Second-order upwind

In second-order upwind scheme, quantities at cell faces are computed using a multidimensional linear reconstruction approach. In this approach, higher-order accuracy is achieved at cell faces through a Taylor series expansion of the cell-centered solution about the cell centroid [53]. The face value ϕ_i is computed in the second-order upwind scheme using the following expression:

$$\phi_i = \phi + \nabla\phi \cdot \Delta\vec{s} \tag{Eq. 114}$$

Where ϕ and $\nabla\phi$ are the cell-centered value and its gradient in the upstream cell, and $\Delta\vec{s}$ is the displacement vector from the upstream cell centroid to the face centroid. This formulation requires the determination of the gradient $\nabla\phi$ in each cell. This gradient is computed using the divergence theorem as:

$$\nabla\phi = \frac{1}{V} \sum_i^{Nfaces} \tilde{\phi}_i \vec{A}_i \tag{Eq. 115}$$

Here the face values $\tilde{\phi}_i$ are computed by averaging ϕ from the two cells adjacent to the face. The second-order upwind is the most accurate scheme, however it has been shown that it can give a problem convergence in several applications [51].

In this study, the momentum equations and energy equation are discretized using second-order upwind scheme, while the turbulence transport equations are discretized using first-order upwind scheme due to the convergence problem.

3.4.4 Pressure interpolation schemes

The conservation equations described in the previous section are applied to each control volume in the computational domain. All dependent variables ($u, v, w, T, p, k, \epsilon$) are stored in the center of the control volume. However, the value of the pressure on the faces is necessary for the resolution of the equation of momentum for incompressible flows where no equation of state exists for pressure. Therefore, an interpolation scheme should be used to determine the pressure from the values at the center of the cells. This can be done using one of the following schemes available in ANSYS FLUENT:

3.4.4.1 Linear

Linear interpolation scheme computes the pressure on the face by averaging the pressures of the adjacent control volumes.

3.4.4.2 Second order

In the second order scheme [53], the pressure is reconstructed on the face using a central differencing scheme. This interpolation can provide an improvement of results, but it has been shown that it has convergence problems when is used especially at the beginning of the calculations [50].

3.4.4.3 PRESTO

PRESTO (PREssure Staggering Option) uses the discrete continuity balance for a “staggered” control volume about the face to compute the “staggered” (that is, face) pressure. This procedure is similar in spirit to the staggered-grid schemes used with structured meshes [48]. This interpolation is only implemented for quadrilateral or hexahedral control volumes.

3.4.4.4 Body Force Weighted

The Body Force Weighted scheme computes the face pressure by assuming that the normal gradient of the difference between pressure and body forces is constant. This interpolation is recommended when body forces are large, e.g., high Rayleigh natural convection or highly swirling flows.

3.4.4.5 Standard

In the Standard scheme [54], the pressure values are interpolated to the faces using the coefficients of the discretized equation of momentum. This interpolation is the simplest and the best especially when the pressure variation between two control volumes is small. In this study, the Standard scheme has been used for all studied cases.

3.4.5 Pressure-Velocity coupling

In fact, the numerically solving of the Navier-Stokes equations discretized system presents two difficulties:

- (i) The non-linearity of the convective terms in the momentum equations.
- (ii) In the source term, the pressure field is not known and it there is no governing equation for the pressure field.

The three equations of the momentum are coupled; each component of velocity appears in each momentum equation and in the continuity equation. The pressure gradient is part of the source term of the momentum equation. The pressure field is indirectly specified via the continuity equation. Therefore, the coupling between the pressure and the velocity will introduce a constraint in the solution of the flow field: if a correct pressure field is applied to the momentum equations, the resulting velocity field must satisfy the continuity equation [55].

All the difficulties outlined above will be overcome by the use of an iterative procedure. The role of pressure-velocity coupling is so to obtain a pressure equation from the discrete continuity equation. Several algorithms are available for achieve this purpose. In following sections, SIMPLE, SIMPLEC and Coupled algorithms will be presented.

3.4.5.1 SIMPLE/SIMPLEC algorithms

The SIMPLE algorithm (Semi-Implicit Method for Pressure-Linked Equations) which has been proposed by Patankar and Spalding [47], is the first version of pressure-velocity coupling algorithms. This algorithm uses a relationship between velocity and pressure corrections to enforce mass conservation and to obtain the pressure field. The iterative procedure of this algorithm starts with the estimation of pressure. Then, an approximation of the velocity field is obtained by solving the momentum equation. The pressure gradient term is calculated using the pressure distribution from the previous iteration or an initial guess. Thereafter, the pressure equation is formulated and solved in order to obtain the new pressure distribution. Finally, velocities are corrected and a new set of conservative fluxes is calculated.

In the SIMPLE algorithm, the discretized momentum equation and pressure correction equation are solved implicitly, where the velocity correction is solved explicitly. This is the reason why it is called "Semi-Implicit Method". Among the disadvantages of this algorithm, the divergence in the case where the corrections are too fast, and also since this algorithm is based on the estimating of pressure field, it is required an important number of iterations [49, 55].

Several algorithms have been developed to improve the SIMPLE algorithm. Among of improved algorithms from the original SIMPLE algorithm, the SIMPLEC (SIMPLE Consistent) algorithm which was developed by Van Doormal and Raithby [56]. The steps of this algorithm are almost the same as those of the SIMPLE algorithm where the difference that in the speed correction equations neglects the least significant terms. It has been shown that the SIMPLEC algorithm is the most suitable for a larger of applications and it can give a converged solution more quickly than SIMPLE algorithm [50, 52].

3.4.5.2 Coupled algorithm

In the previous presented algorithms, the momentum equation and pressure correction equations are solved separately. This type of coupling called the pressure-based segregated algorithm. Among disadvantages of those algorithms, the slow of the convergence. Another alternative available based on the coupled approach is developed called pressure-based coupled algorithm [50] developed by FLUENT's team. The coupled algorithm solves the momentum and pressure-based continuity equations together. The full implicit coupling is achieved through

an implicit discretization of pressure gradient terms in the momentum equations, and an implicit discretization of the face mass flux. This approach offers some advantages over the non-coupled or segregated approach and it has been shown it is the most robust and appropriate especially for steady-state simulations [57].

In this study, in first step, the comparison between SIMPLE, SIMPLEC and coupled algorithms was performed to resolve the Pressure-Velocity coupling equations. It was found that the coupled algorithm allows accelerating the convergence of solutions by 25%. Therefore, the coupled algorithm was used in the present study.

3.4.6 Boundary conditions

Setting the correct boundary conditions is a very important step for any numerical study. These boundary conditions must be very close to the reality of the studied physical phenomenon. However, due to the complicated of those phenomena, simplifications of the boundary conditions are needed. For EAHE applications, since the velocity of air is habitually quite low compared to sound speed, where the Mach number does not exceed 0.3. Therefore, the flow is considered as incompressible, and its properties as constants. The boundary conditions used in the present study, can be summarized as follow:

- (i) **Velocity inlet:** at the inlet of the EAHE pipe, the velocity can be assumed constant.
- (ii) **Outflow:** in the outlet boundary, where the pressure and temperature are not known, the outflow boundary condition is more suitable for this case. This boundary applies a zero-flux normal to the outlet surface for compute all problem variables.
- (iii) **Wall:** for the wall of the pipe and for the soil domain, the wall boundary condition has been utilized, this applies a no-slip condition (velocity null) at the pipe wall. For the soil, a constant temperature has been applied (undistributed temperature T_0).

The ANSYS FLUENT solves the fluid domain by solving the Navier-Stokes equations, and the soil domain by solving the heat equation of conduction.



Chapter **IV**

Results and Discussion



Chapter 4

Results and Discussion

4.1 Description of the experimental EAHE setup

The experimental of short-time scale EAHE used here for validation of the methods was carried out by Moumimi's team in the University of Biskra (34°47'N - 5°43'E) in 2009. And reperformed in May 2nd, 2013. As presented in the Figure 20, the experimental EAHE configuration is a horizontal serpentine shape of cylindrical PVC pipe of 110 mm inner diameter and 47 m of length. The whole is buried at a depth of 3 m under a slope of 2% for the evacuation of condensed air. The horizontal serpentine sections of the pipe are spaced by a distance of about 2m. The outlet of the horizontal pipe is connected to a variable flow air extractor through a vertical pipe. Fourteen thermocouples have been used to measure temperature of the air along the horizontal pipe (denoted as T_{in} , T_1 , T_2 , ..., T_{14}). These thermocouples are inserted at different positions along the horizontal pipe length (Figure 21). The main characteristics of the EAHE components and the technical specifications of measurement equipment's are available in the reference [25].



Figure 20 : Photos of the experimental EAHE setup in the University of Biskra: (a) hole with a serpentine shape; (b) buried horizontal PVC pipe with thermocouples.

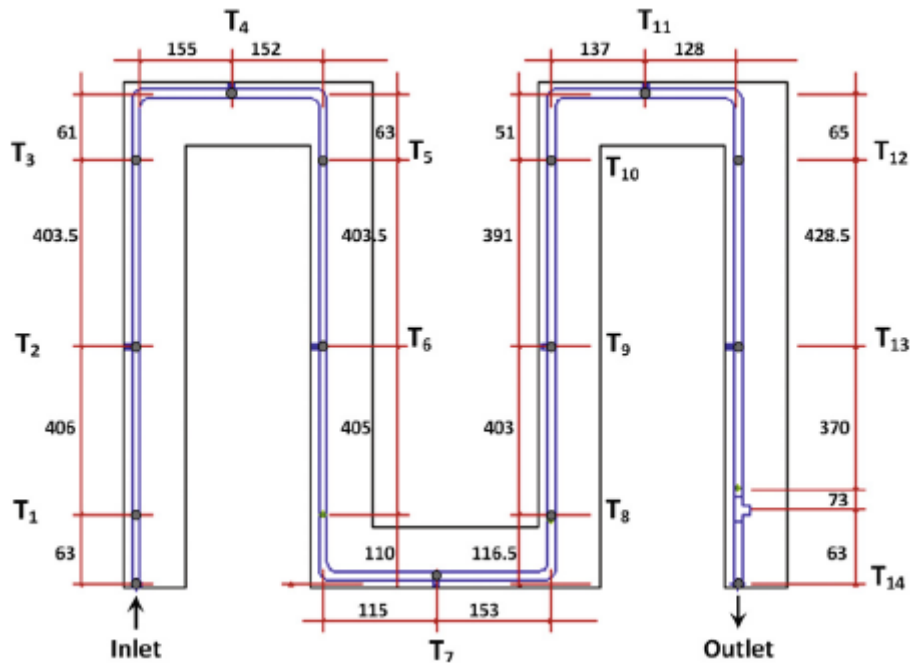


Figure 21: Scheme shows the position of thermocouples measuring air flow temperatures (T_{in} , T_1 , T_2 , ..., T_{14}) with the following distances (from the EAHE inlet): 0, 63, 469, 872, 1089, 1304, 1707, 2337, 2607, 3010, 3400, 3589, 3782, 4210, 4700 cm.

Experiments were performed at the Biskra University on May 2nd, 2013 from 09:45 to 15:45. Temperatures are measured each 15 min for a constant air flow velocity of 3.5 m/s. The experimental measurements of air temperatures obtained from the fourteen thermocouples are presented in Figure 22.

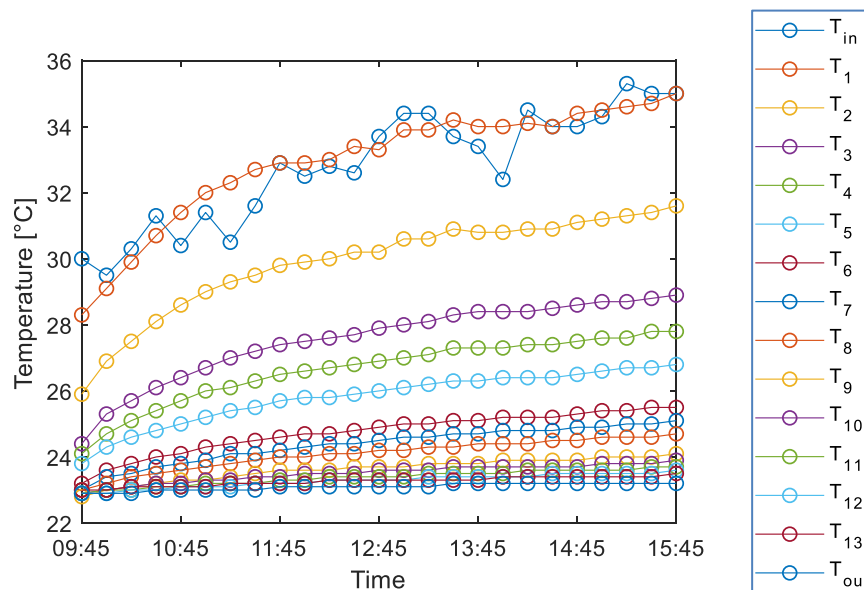


Figure 22: Variation of EAHE temperature with time at different positions.

4.2 Determination of the undistributed soil temperature

In order to determine the undistributed soil temperature in the Biskra region ($34^{\circ}47'N - 5^{\circ}43'E$), we used the Kusuda equation (Eq. 14 in chapter 2). The Kusuda equation needs the amplitude (T_{amp}), average temperature (T_{mean}) and t_{shift} as input parameters. These informations can be obtained from metrological conditions. For this purposes, we used the daily average temperature measured by NASA for the year of 2014 [58]. The used ambient temperature distributions are presented in Figure 23. Here, T_{mean} is the soil's average temperature ($^{\circ}C$), T_{amp} is the amplitude of surface temperature ($^{\circ}C$) calculated using $((T_{max} - T_{min})/2)$; T_{max} is the maximal ambient temperature ($^{\circ}C$) and T_{min} is the minimal ambient temperature ($^{\circ}C$) and t_{shift} is the day of the year with the minimum temperature value of the surface.

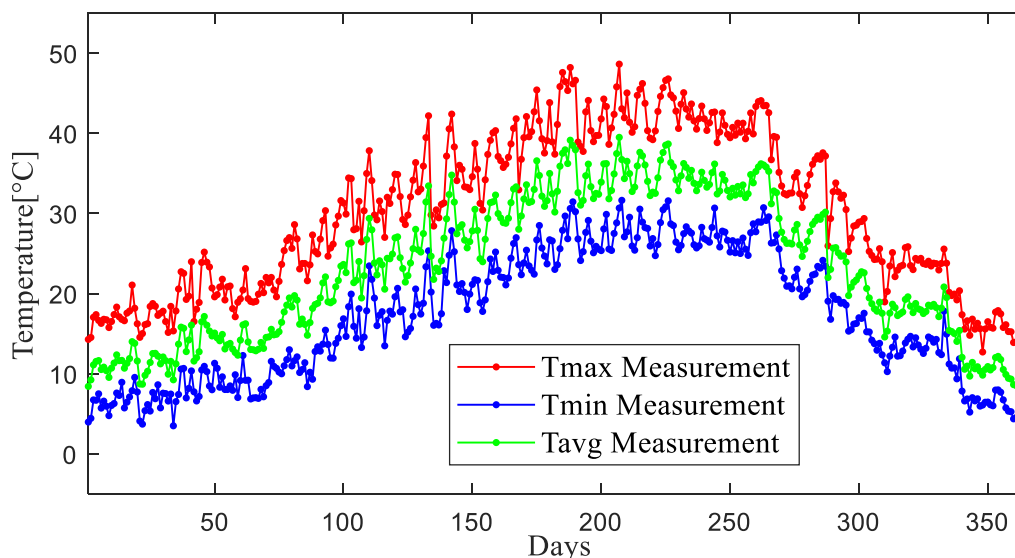


Figure 23: Variation of the min, max and average temperature at the level of 2 m, measured for Biskra region by [58].

Figure 24 presents the distribution of the soil temperature with depth for different days of seasonal transformations (21th January, March, June, September and December) calculated using Kusuda equation based on the data presented in the Figure 23. From Figure 24, it can be seen than the undistributed temperature of the soil reams constant throught the year (around of $22.5^{\circ}C$). It can be observed also from the figure, in the summer season (June for example), the temperature of the ground surface reaches $45^{\circ}C$ and it decreases rapidly with the depth. On the other hand, in the winter season (January for example), the ground temperature at the surface is cool around of $0^{\circ}C$ and it increases with the depth. The undistributed temperature of the

ground leads to the possibility of exploiting the earth's underground temperature for cooling and heating.

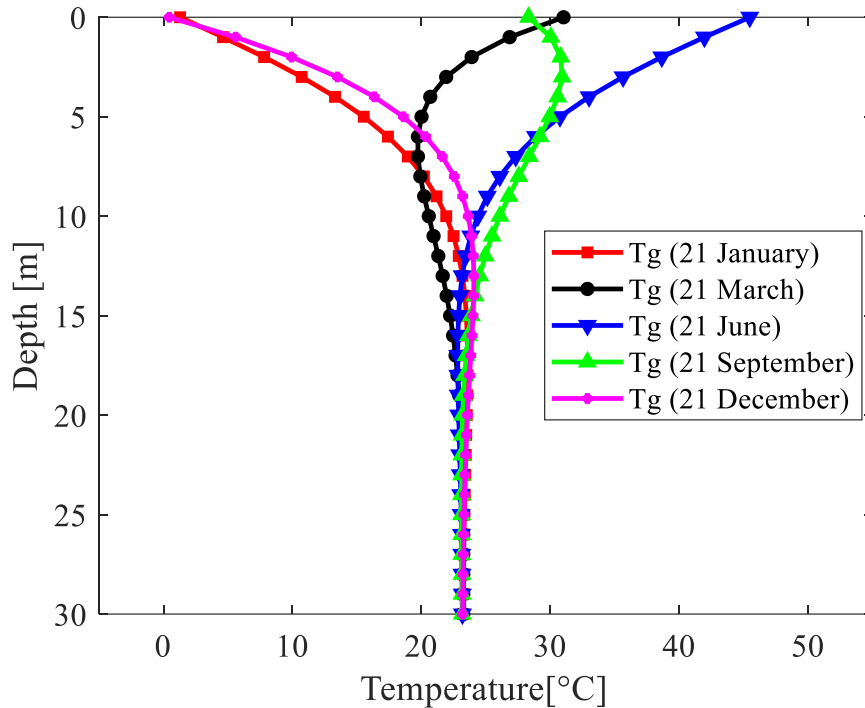


Figure 24: Distribution of the ground temperature with depth simulated for Biskra region using Kusuda equation.

4.3 Analytical simulations

4.3.1 ICS model

In order to validate the analytical, semi-analytical and CFD models, with the experimental results described above, a horizontal EAHE of 47 m of length and 0.22 m of diameter has been simulated. Table 2 presents the physical and thermal properties of air, pipe and soil used in the validation.

Tableau 2 : Physical and thermal properties of air, pipe and soil used in the validation [25].

	Density (kg/m ³)	Specific heat Capacity (J/Kg.K)	Thermal Conductivity (W/m.K)
Air	1.225	1005	0.0242
Soil	1800	1340	1.5
Pipe (PVC)	1380	900	0.16

Figure 25 presents the variation of the air temperature with the pipe position for different time calculated using ICS model. It can be observed that with the increase in hours,

the air temperature decreases especially in the first part of the EAHE. However, the variation at the outlet part is very small due to the continuous operation and the length of the heat exchanger.

Figure 26 shows the evolution of the ICS predicted air temperature along the pipe compared to the experimental results after different hours of functioning. It is noticed that the ICS model curves are fairly consistent with the experimental data.

Figure 27 presents the variation of the outlet temperature with operation time. The curves of ICS and experimental data seem in good agreement. However, the ICS under predicted slightly the outlet temperature especially in the outlet part of the exchanger.

Table 3 shows the validation of the ICS model air temperatures with the experimental measurements carried out in the University of Biskra (May 2nd, 2013). With the increase in the time, the relative error increases. The minimum error is 1.38 %, where the maximum error is around of 2.66 %.

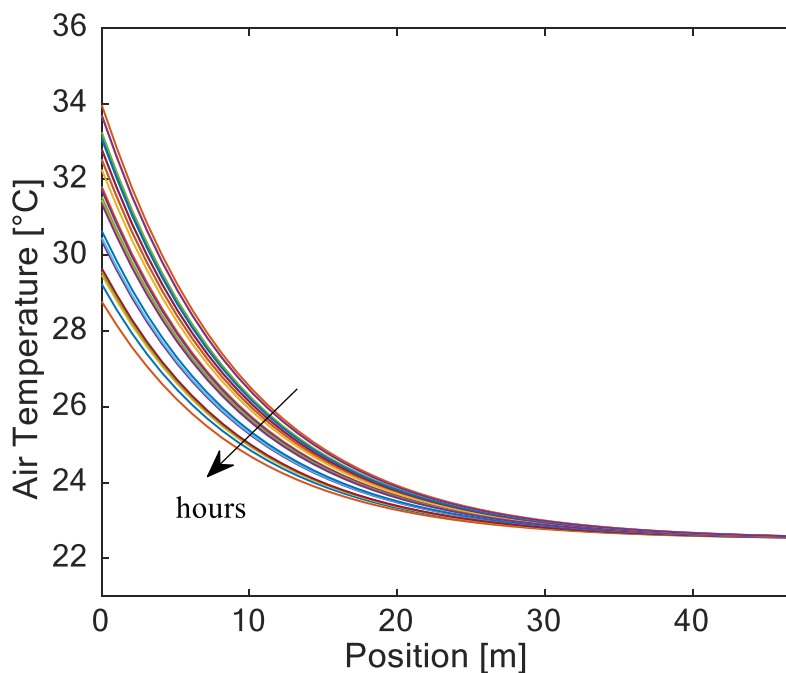


Figure 25: Variation of the air temperature with EAHE length, calculated using ICS model.

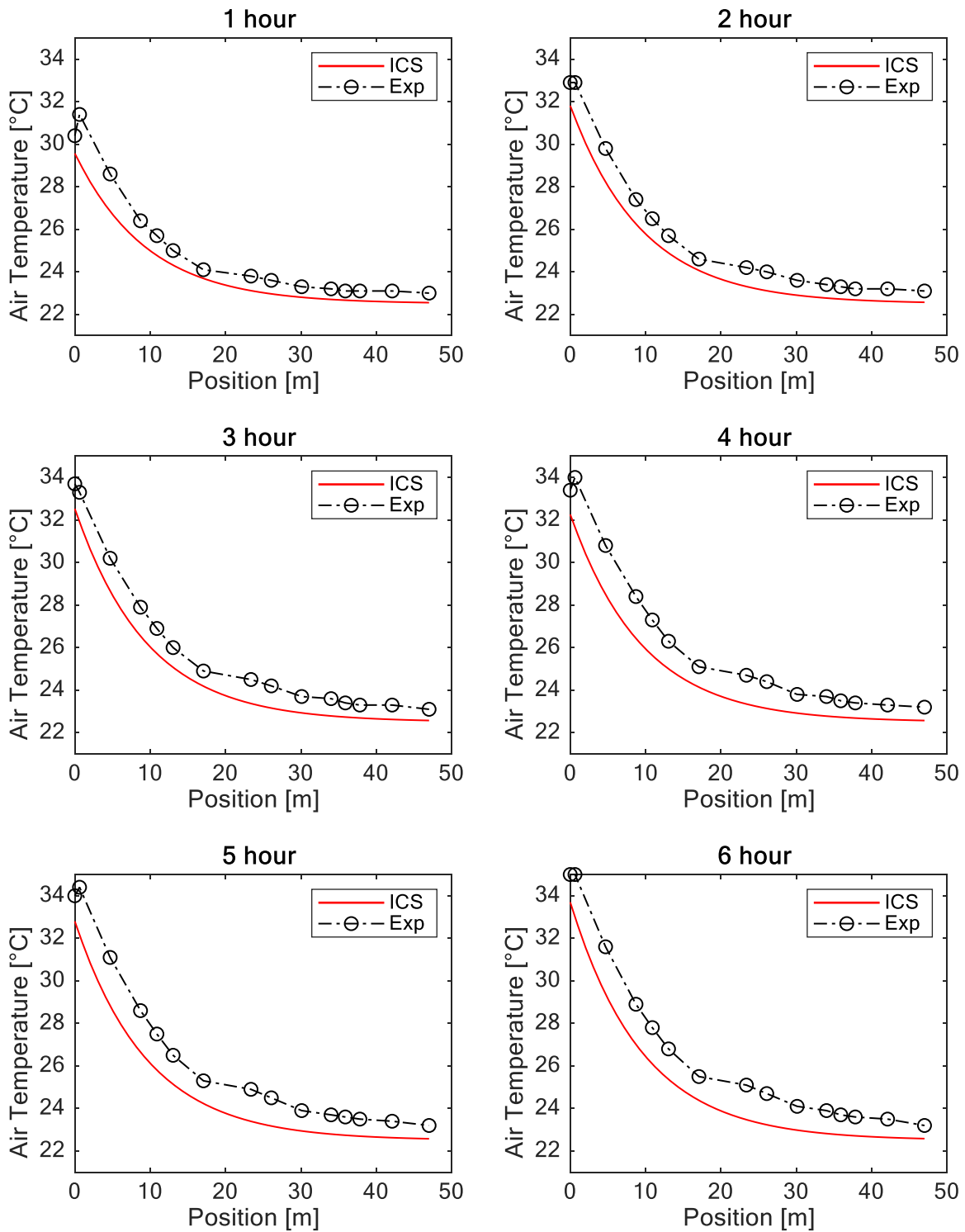


Figure 26: Validation of the ICS model with experimental results after different hours of functioning.

Tableau 3: Validation of the ICS model air temperatures with the experimental measurements carried out in the University of Biskra (May 2nd, 2013).

Time (HH: MM)	Duration (Hours)	Tin (°C)	Tout Exp (°C)	Tout ICS (°C)	Relative error (%)
09:45	0	30	22.9	22.5492	1.3889
10:00	¼	29.5	22.9	22.5459	1.3889
10:15	½	30.3	22.9	22.5511	1.3889
10:30	¾	31.3	23	22.5577	1.8176
10:45	1	30.4	23	22.5518	1.8176
11:00	1¼	31.4	23	22.5583	1.8176
11:15	1½	30.5	23	22.5524	1.8176
11:30	1¾	31.6	23	22.5597	1.8176
11:45	2	32.9	23.1	22.5682	2.2427
12:00	2¼	32.5	23.1	22.5656	2.2427
12:15	2½	32.8	23.1	22.5675	2.2427
12:30	2¾	32.6	23.1	22.5662	2.2427
12:45	3	33.7	23.1	22.5734	2.2427
13:00	3¼	34.4	23.1	22.5780	2.2427
13:15	3½	34.4	23.1	22.5780	2.2427
13:30	3¾	33.7	23.2	22.5734	2.6640
13:45	4	33.4	23.2	22.5715	2.6640
14:00	4¼	32.4	23.2	22.5649	2.6640
14:15	4½	34.5	23.2	22.5787	2.6640
14:30	4¾	34	23.2	22.5754	2.6640
14:45	5	34	23.2	22.5754	2.6640
15:00	5¼	34.3	23.2	22.5774	2.6640
15:15	5½	35.3	23.2	22.5839	2.6640
15:30	5¾	35	23.2	22.5819	2.6640
15:45	6	35	23.2	22.5819	2.6640

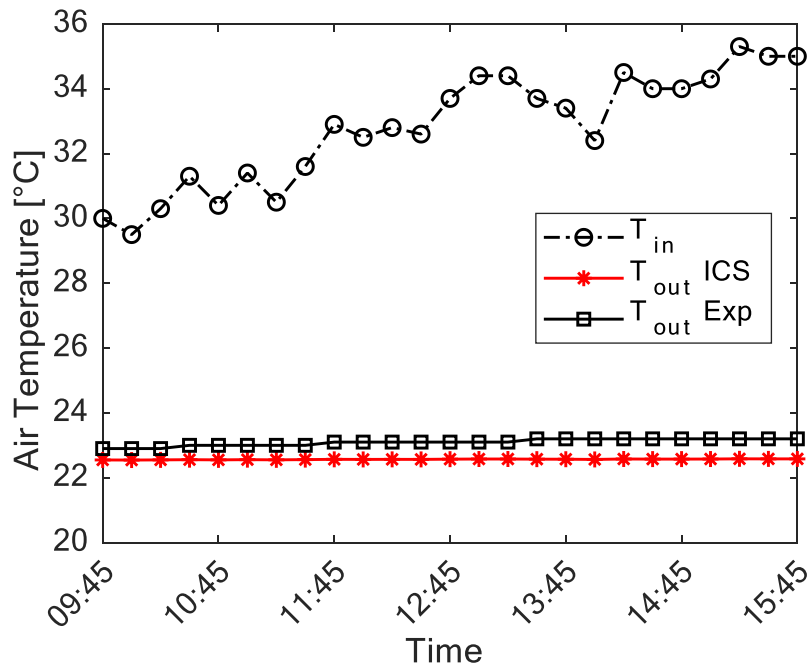


Figure 27: Variation of the outlet temperature with time of operation, validation of the ICS model with experimental data.

4.3.2 ILS model

Figure 28 presents the variation of the air temperature with the pipe length for different operation time, calculated using IFS model. It can be observed that with the increase in hours, the air temperature decreases especially in the first part of the exchanger. However, the variation at the outlet part is very small due to the continuous operation and the length of the heat exchanger.

Figure 29 presents the variation of the outlet temperature with operation time. The curves of IFS and experimental data seem in good agreement. However, the IFS under predicted slightly the outlet temperature especially in the outlet part of the exchanger.

Figure 30 shows the evolution of the IFS predicted air temperature along the pipe compared to the experimental results after different hours of functioning. It is noticed that the IFS model curves are in good agreements with experimental data.

Table 4 shows the validation of the IFS model air temperatures with the experimental measurements carried out in the University of Biskra. With the increase in the time, the relative error slightly increases. The minimum error is 1.29 %, where the maximum error is around of 2.57 %.

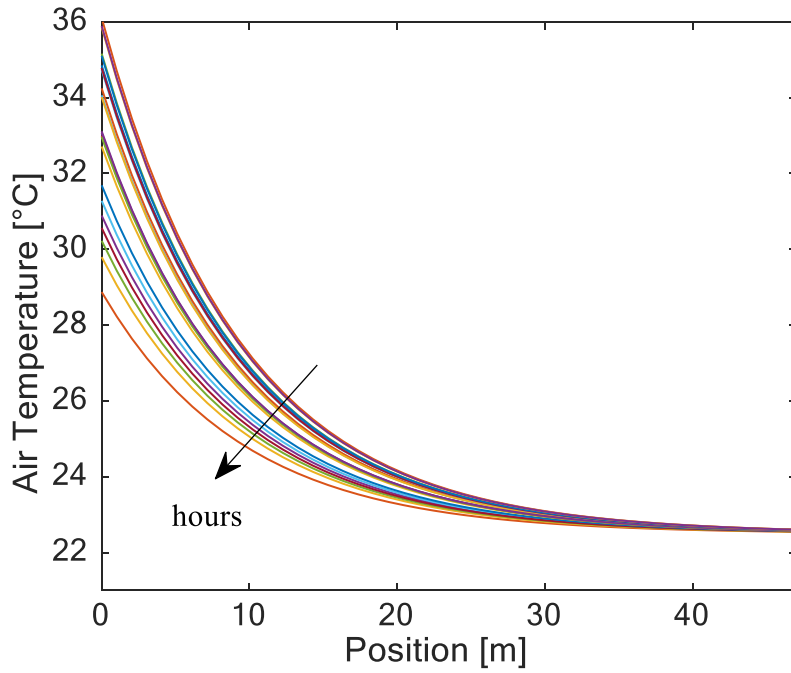


Figure 28: Variation of the air temperature with EAHE length, calculated using ILS model.

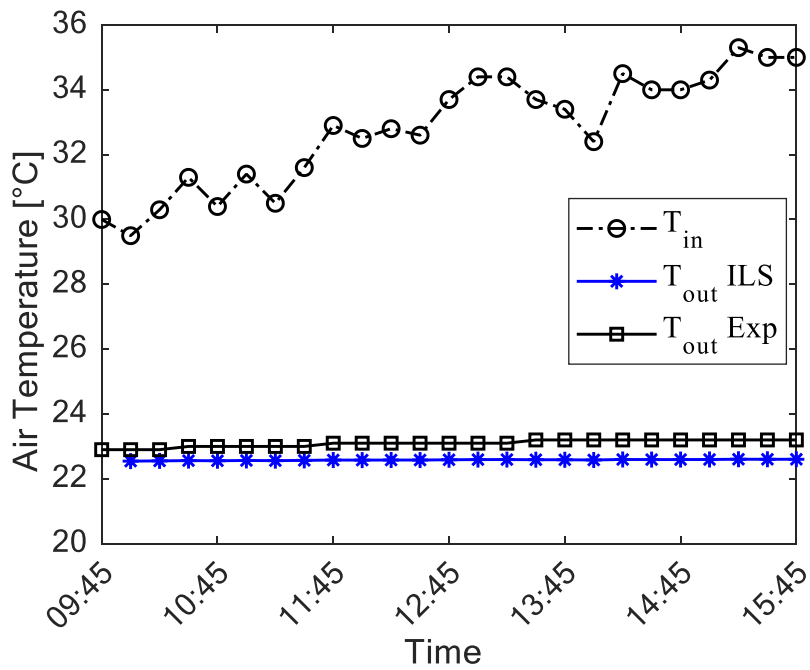


Figure 29: Variation of the outlet temperature with time of operation, validation of the ILS model with experimental data.

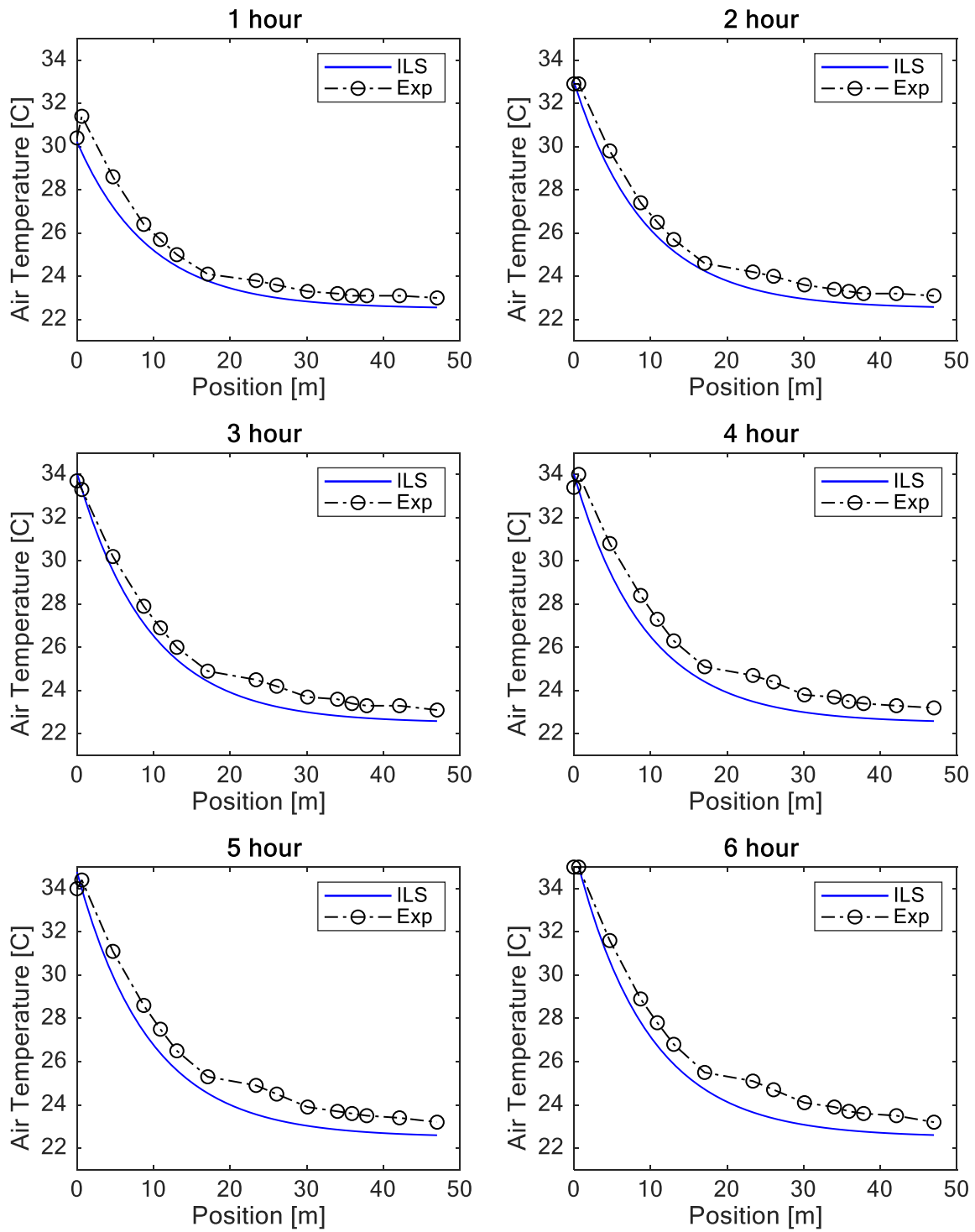


Figure 30: Validation of the ILS model with experimental results after different hours of functioning.

Tableau 4: Validation of the ILS model air temperatures with the experimental measurements carried out in the University of Biskra (May 2nd, 2013).

Time (HH: MM)	Duration (Hours)	Tin (°C)	Tout Exp (°C)	Tout ILS (°C)	Relative error (%)
09:45	0	30	22.9	22.5540	1.2938
10:00	¼	29.5	22.9	22.5467	1.2938
10:15	½	30.3	22.9	22.5540	1.2938
10:30	¾	31.3	23	22.5626	1.7230
10:45	1	30.4	23	22.5581	1.7230
11:00	1¼	31.4	23	22.5662	1.7230
11:15	1½	30.5	23	22.5613	1.7230
11:30	1¾	31.6	23	22.5699	1.7230
11:45	2	32.9	23.1	22.5798	2.1484
12:00	2¼	32.5	23.1	22.5779	2.1484
12:15	2½	32.8	23.1	22.5808	2.1484
12:30	2¾	32.6	23.1	22.5801	2.1484
12:45	3	33.7	23.1	22.5885	2.1484
13:00	3¼	34.4	23.1	22.5941	2.1484
13:15	3½	34.4	23.1	22.5947	2.1484
13:30	3¾	33.7	23.2	22.5904	2.5702
13:45	4	33.4	23.2	22.5888	2.5702
14:00	4¼	32.4	23.2	22.5822	2.5702
14:15	4½	34.5	23.2	22.5976	2.5702
14:30	4¾	34	23.2	22.5945	2.5702
14:45	5	34	23.2	22.5949	2.5702
15:00	5¼	34.3	23.2	22.5975	2.5702
15:15	5½	35.3	23.2	22.6051	2.5702
15:30	5¾	35	23.2	22.6033	2.5702
15:45	6	35	23.2	22.6037	2.5702

4.3.3 FLS model

Figure 31 presents the variation of the air temperature with the pipe length for different operation time, calculated using FLS model. It can be observed that with the increase in hours, the air temperature decreases especially in the first part of the exchanger. However, the variation at the outlet part is very small due to the continuous operation and the length of the heat exchanger.

Figure 32 shows the evolution of the FLS predicted air temperature along the pipe compared to the experimental results after different hours of functioning. It is noticed that the FLS model curves are in good agreements with experimental data.

Figure 33 presents the variation of the outlet temperature with operation time. The curves of IFS and experimental data seem in good agreement. However, the FLS under predicted slightly the outlet temperature especially in the outlet part of the exchanger.

Table 5 shows the validation of the FLS model air temperatures with the experimental measurements carried out in the University of Biskra. With the increase in the time, the relative error slightly increases. The minimum error is 1.38 %, where the maximum error is around of 2.66%.

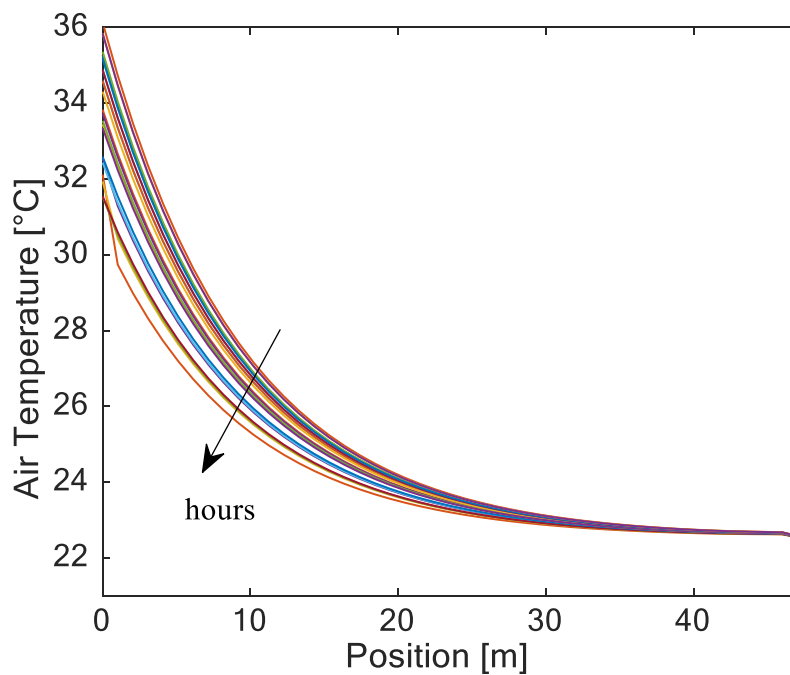


Figure 31: Variation of the air temperature with EAHE length, calculated using FLS model.

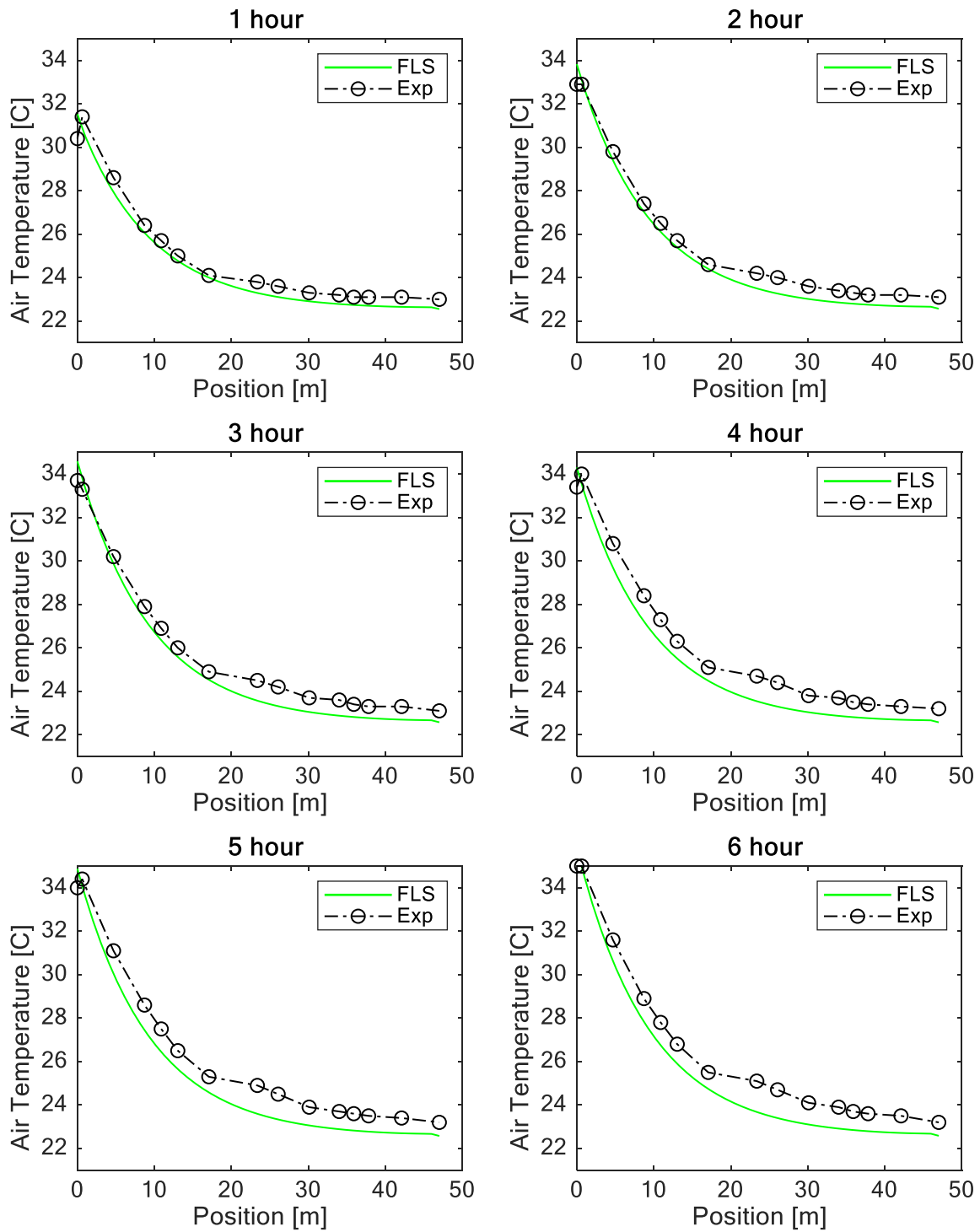


Figure 32: Validation of the FLS model with experimental results after different hours of functioning.

Tableau 5: Validation of the FLS model air temperatures with the experimental measurements carried out in the University of Biskra (May 2nd, 2013).

Time (HH: MM)	Duration (Hours)	Tin (°C)	Tout Exp (°C)	Tout FLS (°C)	Relative error (%)
09:45	0	30	22.9	22.6059	1.3888
10:00	¼	29.5	22.9	22.5537	1.3888
10:15	½	30.3	22.9	22.5542	1.3888
10:30	¾	31.3	23	22.5590	1.8175
10:45	1	30.4	23	22.5523	1.8175
11:00	1¼	31.4	23	22.5586	1.8175
11:15	1½	30.5	23	22.5526	1.8175
11:30	1¾	31.6	23	22.5597	1.8175
11:45	2	32.9	23.1	22.5682	2.2426
12:00	2¼	32.5	23.1	22.5656	2.2426
12:15	2½	32.8	23.1	22.5675	2.2426
12:30	2¾	32.6	23.1	22.5662	2.2426
12:45	3	33.7	23.1	22.5734	2.2426
13:00	3¼	34.4	23.1	22.5780	2.2426
13:15	3½	34.4	23.1	22.5780	2.2426
13:30	3¾	33.7	23.2	22.5734	2.6640
13:45	4	33.4	23.2	22.5715	2.6640
14:00	4¼	32.4	23.2	22.5649	2.6640
14:15	4½	34.5	23.2	22.5787	2.6640
14:30	4¾	34	23.2	22.5754	2.6640
14:45	5	34	23.2	22.5754	2.6640
15:00	5¼	34.3	23.2	22.5774	2.6640
15:15	5½	35.3	23.2	22.5839	2.6640
15:30	5¾	35	23.2	22.5820	2.6640
15:45	6	35	23.2	22.5820	2.6640

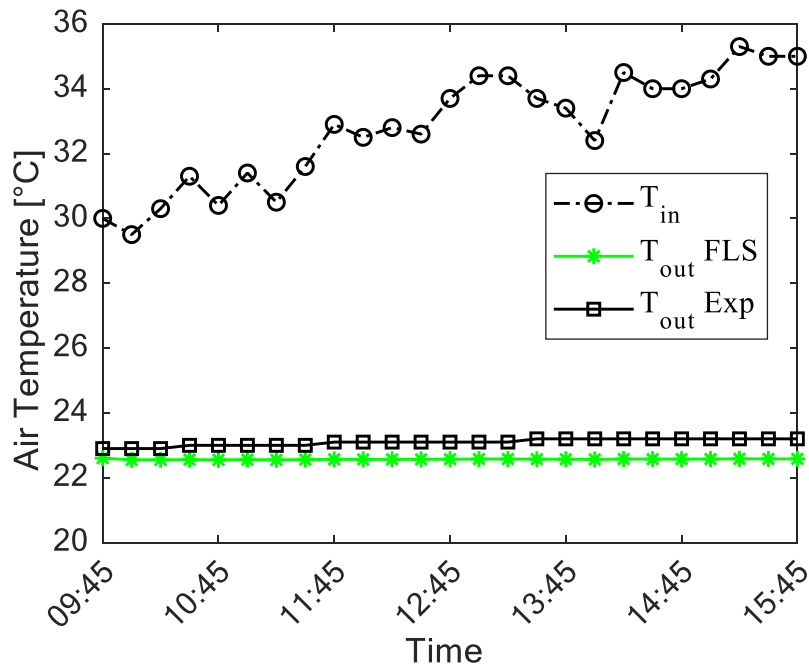


Figure 33: Variation of the outlet temperature with time of operation, validation of the FLS model with experimental data.

4.4 Semi-analytical model

Figure 34 presents the variation of the air temperature with the pipe length for different operation time, calculated using GRBM model. It can be observed that with the increase in hours, the air temperature decreases especially in the first part of the exchanger. However, the variation at the outlet part is very small due to the continuous operation and the length of the heat exchanger.

Figure 35 presents the variation of the outlet temperature with operation time. The curves of GRBM and experimental data seem in good agreement.

Figure 36 shows the evolution of the GRBM predicted air temperature along the pipe compared to the experimental results after different hours of functioning. It is noticed that the GRBM model curves are in good agreements with experimental data.

Table 6 shows the validation of the GRBM model air temperatures with the experimental measurements carried out in the University of Biskra. With the increase in the time, the relative error slightly increases. The minimum error is 0.48 %, where the maximum error is around of 0.82%.

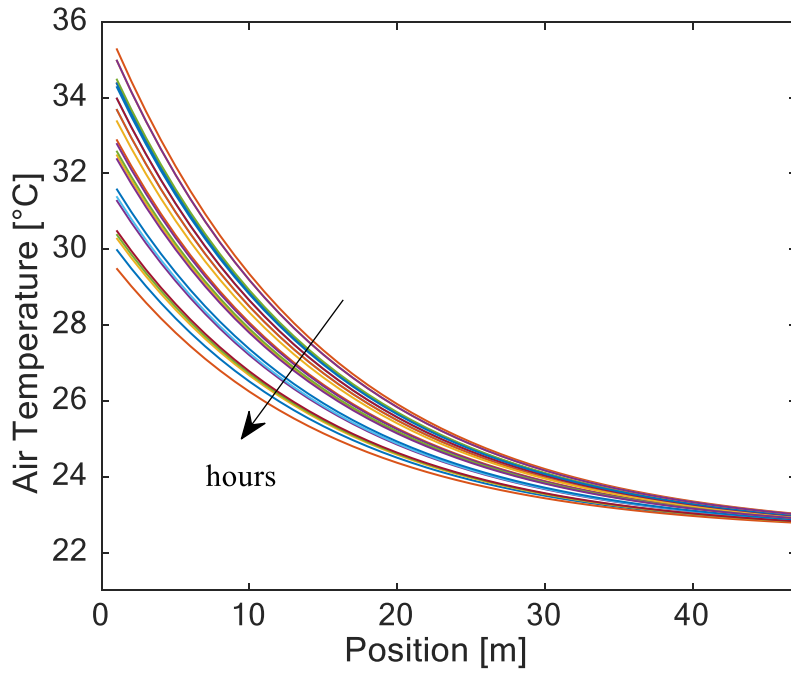


Figure 34: Variation of the air temperature with EAHE length, calculated using GRBM model.

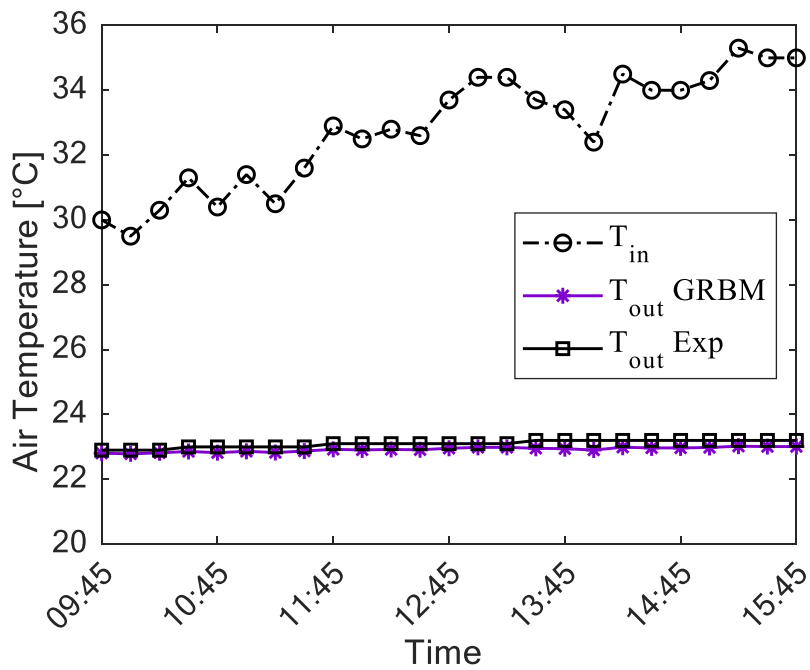


Figure 35: Variation of the outlet temperature with time of operation, validation of the GRBM model with experimental data.

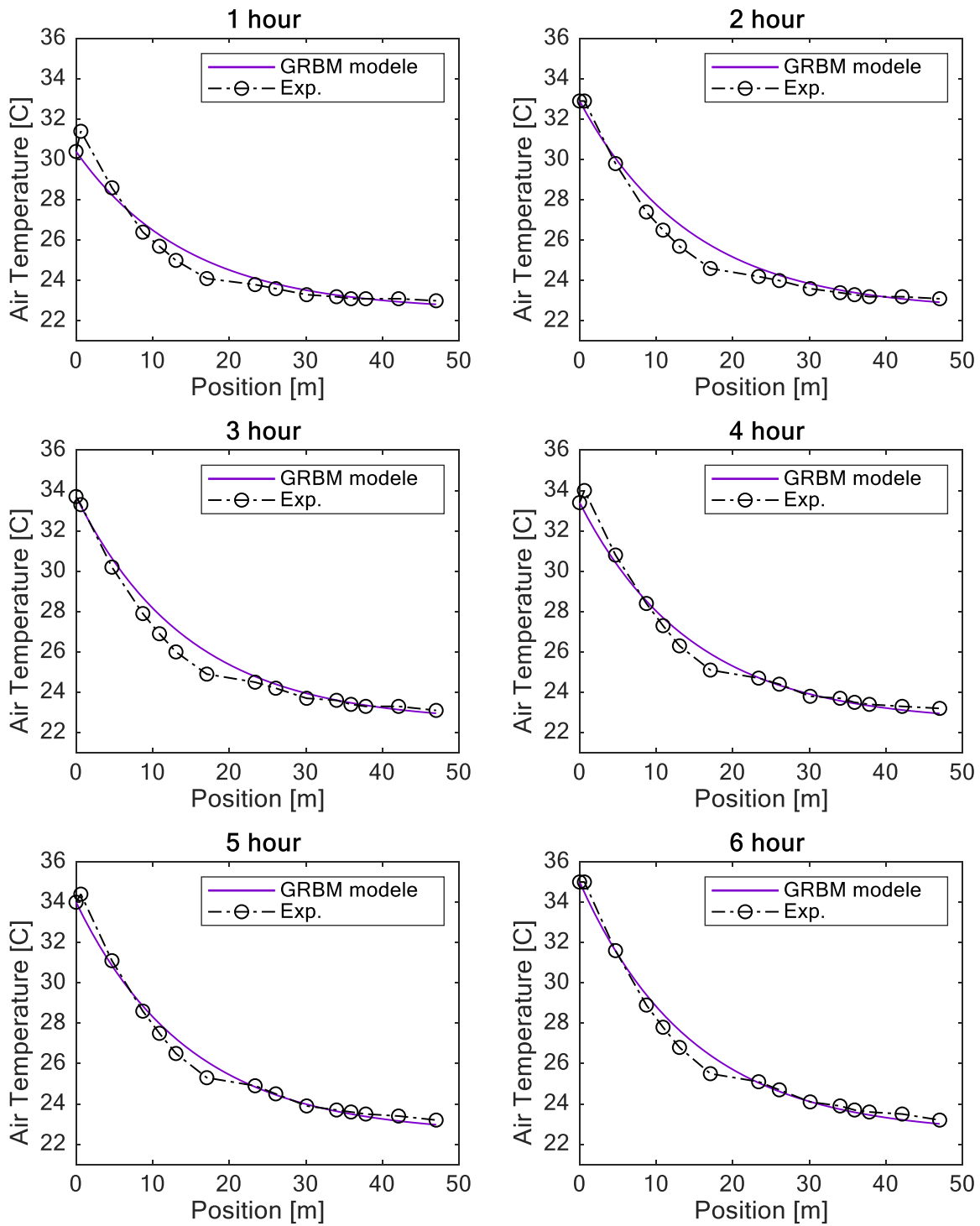


Figure 36: Validation of the GRBM model with experimental results after different hours of functioning.

Tableau 6: Validation of the GRBM model air temperatures with the experimental measurements carried out in the University of Biskra (May 2nd, 2013).

Time (HH: MM)	Duration (Hours)	T _{in} (°C)	T _{out} Exp (°C)	T _{out} GRBM (°C)	Relative error (%)
09:45	0	30	22.9	22.8060	0.4801
10:00	¼	29.5	22.9	22.7856	0.4801
10:15	½	30.3	22.9	22.8182	0.4801
10:30	¾	31.3	23	22.8590	0.0432
10:45	1	30.4	23	22.8223	0.0432
11:00	1¼	31.4	23	22.8631	0.0432
11:15	1½	30.5	23	22.8264	0.0432
11:30	1¾	31.6	23	22.8712	0.0432
11:45	2	32.9	23.1	22.9243	0.3899
12:00	2¼	32.5	23.1	22.9079	0.3899
12:15	2½	32.8	23.1	22.9202	0.3899
12:30	2¾	32.6	23.1	22.9120	0.3899
12:45	3	33.7	23.1	22.9569	0.3899
13:00	3¼	34.4	23.1	22.9855	0.3899
13:15	3½	34.4	23.1	22.9855	0.3899
13:30	3¾	33.7	23.2	22.9569	0.8193
13:45	4	33.4	23.2	22.9447	0.8193
14:00	4¼	32.4	23.2	22.9039	0.8193
14:15	4½	34.5	23.2	22.9895	0.8193
14:30	4¾	34	23.2	22.9691	0.8193
14:45	5	34	23.2	22.9691	0.8193
15:00	5¼	34.3	23.2	22.9814	0.8193
15:15	5½	35.3	23.2	23.0222	0.8193
15:30	5¾	35	23.2	23.0099	0.8193
15:45	6	35	23.2	23.0099	0.8193

4.5 CFD model

Figure 37 presents the variation of the air temperature with the pipe length for different operation time, calculated using the transient CFD model (time step = 30s, simulation time= 6 hours). It can be observed that with the increase in hours, the air temperature decreases especially in the first part of the exchanger.

Figure 38 shows the evolution of the CFD predicted average air temperature along the pipe compared to the experimental results after different hours of functioning. It is noticed that the CFD model curves are in good agreements with experimental data.

Figure 39 presents the variation of the outlet temperature with operation time. The curves of CFD and experimental data seem in good agreement.

Table 7 shows the validation of the CFD model air temperatures with the experimental measurements carried out in the University of Biskra. With the increase in the time, the relative error slightly increases. The minimum error is very small around of 0.19%, where the maximum error is around of 0.67%.

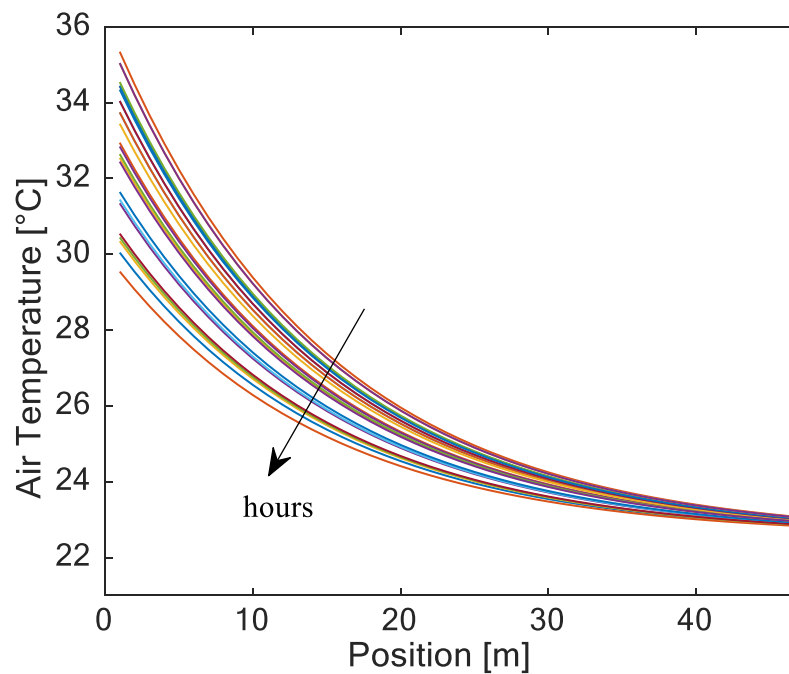


Figure 37: Variation of the air temperature with EAHE length, calculated using CFD model.

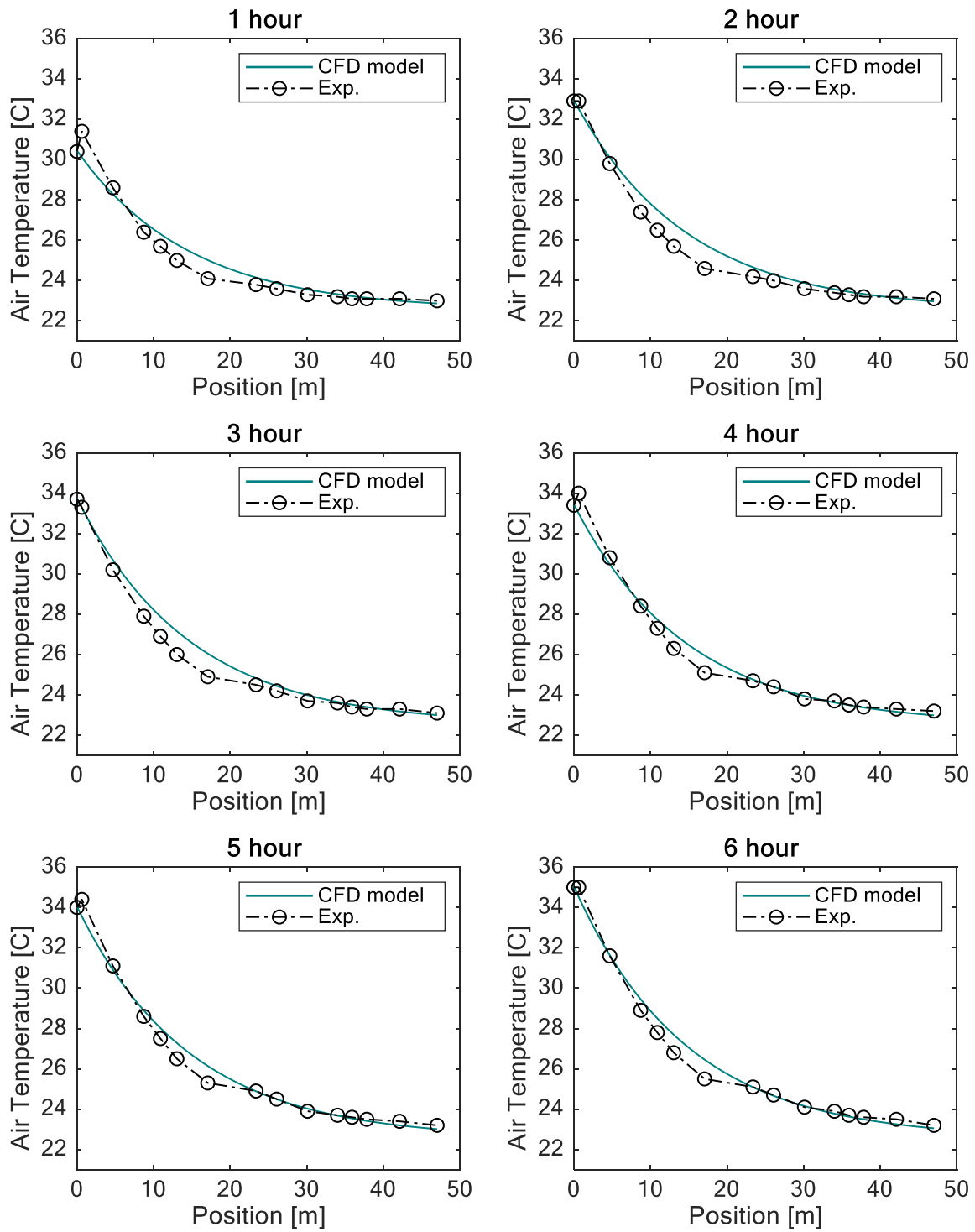


Figure 38: Validation of the CFD model with experimental results after different hours of functioning.

Tableau 7: Validation of the CFD model air temperatures with the experimental measurements carried out in the University of Biskra (May 2nd, 2013).

Time (HH: MM)	Duration (Hours)	Tin (°C)	Tout Exp (°C)	Tout CFD (°C)	Relative error (%)
09:45	0	30	22.9	22.8501	-
10:00	¼	29.5	22.9	22.8297	0.6729
10:15	½	30.3	22.9	22.8624	0.6729
10:30	¾	31.3	23	22.9032	0.6729
10:45	1	30.4	23	22.8664	0.2352
11:00	1¼	31.4	23	22.9072	0.2352
11:15	1½	30.5	23	22.8705	0.2352
11:30	1¾	31.6	23	22.9154	0.2352
11:45	2	32.9	23.1	22.9684	0.2352
12:00	2¼	32.5	23.1	22.9521	0.1987
12:15	2½	32.8	23.1	22.9643	0.1987
12:30	2¾	32.6	23.1	22.9562	0.1987
12:45	3	33.7	23.1	23.0011	0.1987
13:00	3¼	34.4	23.1	23.0296	0.1987
13:15	3½	34.4	23.1	23.0296	0.1987
13:30	3¾	33.7	23.2	23.0011	0.1987
13:45	4	33.4	23.2	22.9888	0.6289
14:00	4¼	32.4	23.2	22.9480	0.6289
14:15	4½	34.5	23.2	23.0337	0.6289
14:30	4¾	34	23.2	23.0133	0.6289
14:45	5	34	23.2	23.0133	0.6289
15:00	5¼	34.3	23.2	23.0255	0.6289
15:15	5½	35.3	23.2	23.0663	0.6289
15:30	5¾	35	23.2	23.0541	0.6289
15:45	6	35	23.2	23.0541	0.6289

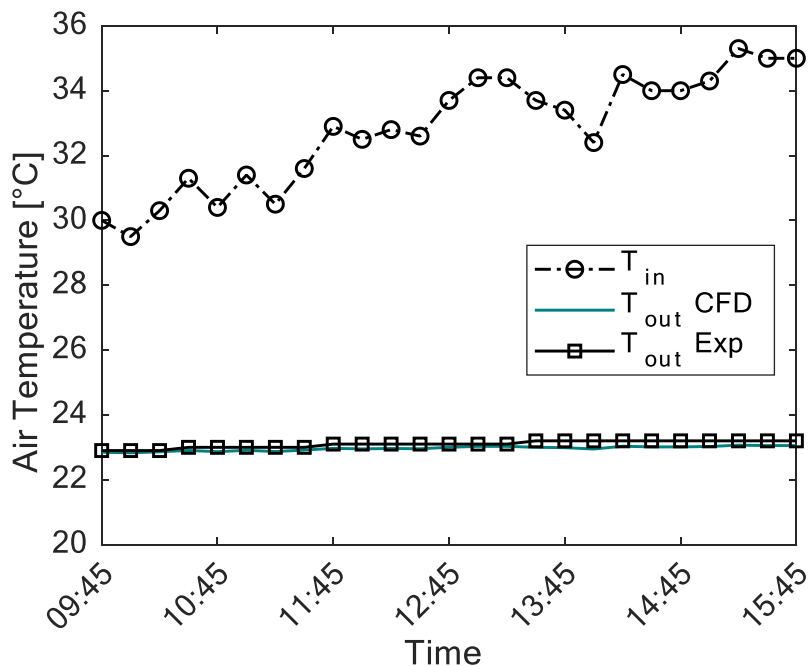


Figure 39: Variation of the outlet temperature with time of operation, validation of the CFD model with experimental data.

4.6 Comparisons of results

To properly examine the accuracy of the studied models on the thermal prediction of the EAHE. We presented the comparison of the local relative error computed for each model based on the outlet temperature (Figure 40), and the comparison of the outlet air temperature (Figure 41). From these figures, it is clear that all studied models give an acceptable results and good agreement with the experimental, where the maximum relative error not exceed 3% in all studied cases. However, there are an important difference between the prediction of the studied models. The analytical models (ICS, ILS and FLS) give almost the same level of accuracy, where the error increases with the time. It has been observed also that both GRBM and CFD give similar predictions, where the error is almost constant. The results obtained by the CFD model is closest to the experimental results, where the error not exceed 0.6 %.

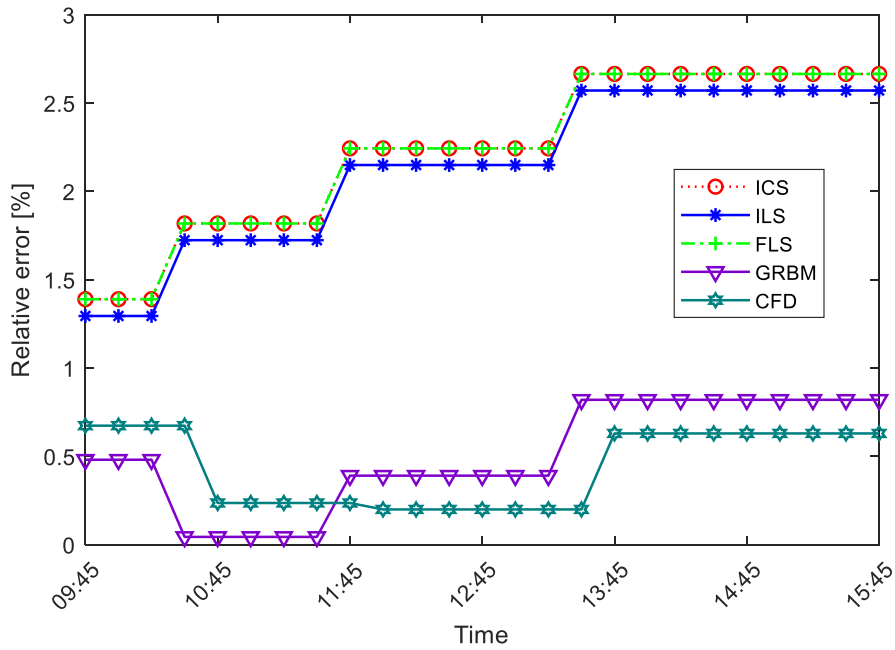


Figure 40: Comparison of local relative error computed using different models.

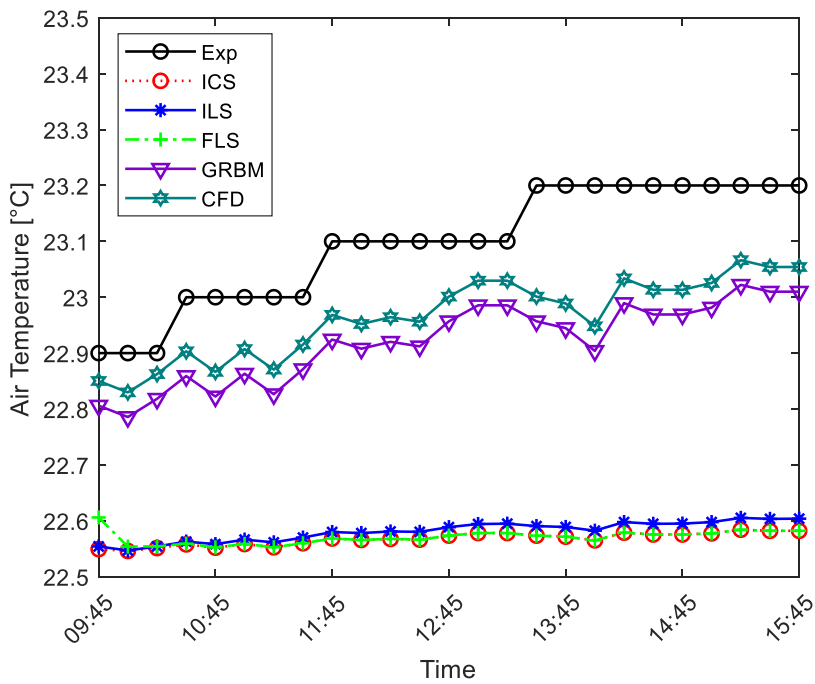


Figure 41: Outlet air temperature variation after 6 hours of operation, comparison between analytical, semi-analytical and CFD methods.

Table 8 presents the comparison of the minimum and the maximum relative error calculated for the five studied models. It has been found that analytical models (ILS, FLS and

ICS) give some error range. According to the accuracy of predictions, the studied models are classified from 1 to 5. In the first place comes the CFD model (range 0.19-0.67%), then the semi-analytical model is classified in the second place (error varied from 0.48-0.81%). The analytical models are categorized in the third place with an error interval varied from 1.38 to 2.66%. However, due to slight difference between results, ILS model is more accurate than other models (FLS and CLS).

Tableau 8: Comparison of min and max relative errors.

Method	Minimum relative error (%)	Maximum relative error (%)	Classification
ICS	1.3889	2.6640	5
ILS	1.2938	2.5702	3
FLS	1.3888	2.6640	4
GRBM	0.4801	0.8193	2
CFD	0.1987	0.6729	1

Conclusion

The study presented in this thesis focuses on transient analytical and numerical simulation of an EAHE installed in the local climate (region of Biskra). The main objective is to evaluate the accuracy of thermal prediction of several analytical, semi-analytical and numerical methods. For this purpose, five methods namely as ICS, ILS, FLS, GRBM, and CFD have been adapted and validated using experimental data available in the literature. For analytical and semi-analytical models, the MATLAB software has been used. For the CFD model, ANSYS FLUENT (academic version) has been utilized. Same assumptions and boundary conditions have been applied for all models, in which the heat exchanger is considered as a horizontal tube buried in the soil. Firstly, the undistributed soil temperature in the Biskra region (34°47'N - 5°43'E) has been calculated analytically using Kusuda equation. Then, the transient air temperature has been calculated for each method using the described formulation. From the work presented in this study, the following conclusions can be drawn:

- All the studied analytical, semi-analytical and CFD methods give accurate results, where the maximum relative error does not exceed 3% in all cases;
- The error between analytical/numerical and experimental results increases slightly with time of operation;
- The results obtained by the CFD model is the closest to the experimental results, where the error not exceed 0.6 % in all simulated cases;
- The results done by analytical models (ICS, ILS and FLS) are very similar; the error is varied from 1.38 to 2.66%. However, the ILS model gives a best accuracy compared to the ICS and FLS models;
- The accuracy of the GRBM and CFD being rather similar, however, the CFD model can improve the results by 0.2% compared to the semi-analytical model.

Perspectives

As perspectives related to this work, we propose:

- As this study has been applied and validated only for short-time scale EAHE, it is recommended to reperform the comparison for long-time scale EAHEs;
- To study numerically or experimentally new geometric configurations (spiral, helicoidal, including of baffles ...) in order to improve the heat transfer through the EAHEs;
- Implementation and study the accuracy of new analytical, semi-analytical and numerical methods, as Green function, g-function, CFD with more advanced turbulence models as Large Eddy Simulation (LES).

Bibliography

1. GWEC, S., Global Wind, *Global Wind Energy Council (GWEC): Opening up new markets for business*. 5 May 2017, Mongolia.
2. (IEA), I.E.A., *World energy outlook 2012*.
3. Ozgener, L., *A review on the experimental and analytical analysis of earth to air heat exchanger (EAHE) systems in Turkey*. *Renewable and Sustainable Energy Reviews*, 2011. **15**(9): p. 4483-4490.
4. Bordoloi, N., et al., *An intense review on the latest advancements of Earth Air Heat Exchangers*. *Renewable and Sustainable Energy Reviews*, 2018. **89**: p. 261-280.
5. Swenka, M.J., *An energy and cost analysis of residential ground-source heat pumps in Iowa*. 2008.
6. Ouali, S., *Étude géothermique du sud de l'Algérie*. 2005.
7. Al-Khoury, R., *Computational modeling of shallow geothermal systems*. 2011: CRC press.
8. Bisoniya, T.S., A. Kumar, and P. Baredar, *Experimental and analytical studies of earth-air heat exchanger (EAHE) systems in India: a review*. *Renewable and Sustainable Energy Reviews*, 2013. **19**: p. 238-246.
9. Gouda, A., *Using of geothermal energy in heating and cooling of agricultural structures*. Benha University, 2010.
10. Sehli, A., A. Hasni, and M. Tamali, *The potential of earth-air heat exchangers for low energy cooling of buildings in South Algeria*. *Energy Procedia*, 2012. **18**: p. 496-506.
11. Grundmann, R.M., *Improved design methods for ground heat exchangers*. 2016.
12. SELAMAT, S.B., *Numerical Modelling for Horizontal Ground Heat Exchangers Optimization*. 2016, 佐賀大学.
13. Nebar, H., *Etude théorique et expérimentale d'un échangeur air/sol destiné au rafraîchissement des locaux par la géothermie*. 2012, Université Mohamed Khider-Biskra.

14. Klein, S., et al., *A transient system simulation program*. Solar Energy Laboratory, University of Wisconsin-Madison, Madison, WI, USA, 2000.
15. Badache, M., et al., *A new modeling approach for improved ground temperature profile determination*. *Renewable Energy*, 2016. **85**: p. 436-444.
16. Jaeger, J.C. and H.S. Carslaw, *Conduction of heat in solids*. 1959: Clarendon P.
17. Ingersoll, L. and H. Plass, *Theory of the ground pipe source for the heat pump*. ASHRAE Transactions, 1948. **54**: p. 339-348.
18. Hart, D.P. and R. Couvillion, *Earth-coupled Heat Transfer: Offers Engineers and Other Practitioners of Applied Physics the Information to Solve Heat Transfer Problems as They Apply to Earth-coupling*. 1986: National water well association.
19. Yener, Y. and S. Kakac, *Heat Conduction*, Taylor and Francis. 2008, Philadelphia.
20. Ingersoll, L.R., O.J. Zabel, and A.C. Ingersoll, *Heat conduction with engineering, geological, and other applications*. 1954.
21. Eskilson, P., *Thermal analysis of heat extraction boreholes*. 1987.
22. Lamarche, L. and B. Beauchamp, *A new contribution to the finite line-source model for geothermal boreholes*. *Energy and Buildings*, 2007. **39**(2): p. 188-198.
23. Marcotte, D. and P. Pasquier, *On the estimation of thermal resistance in borehole thermal conductivity test*. *Renewable energy*, 2008. **33**(11): p. 2407-2415.
24. Rouag, A., A. Benchabane, and C.-E. Mehdid, *Thermal design of Earth-to-Air Heat Exchanger. Part I a new transient semi-analytical model for determining soil temperature*. *Journal of Cleaner Production*, 2018. **182**: p. 538-544.
25. Mehdid, C.-E., et al., *Thermal design of Earth-to-air heat exchanger. Part II a new transient semi-analytical model and experimental validation for estimating air temperature*. *Journal of Cleaner Production*, 2018. **198**: p. 1536-1544.
26. Tzaferis, A., et al., *Analysis of the accuracy and sensitivity of eight models to predict the performance of earth-to-air heat exchangers*. *Energy and buildings*, 1992. **18**(1): p. 35-43.
27. Fiche, A., et al. *Continuous belief functions and α -stable distributions*. in *2010 13th International Conference on Information Fusion*. 2010. IEEE.
28. ANSYS_Fluent, *17 Documentation*. Ansys Inc. 2017.
29. Kolmogorov, A.N. *Dissipation of energy in locally isotropic turbulence*. in *Dokl. Akad. Nauk SSSR*. 1941.
30. Kolmogorov, A.N. *The local structure of turbulence in incompressible viscous fluid for very large Reynolds numbers*. in *Dokl. Akad. Nauk SSSR*. 1941.
31. Smagorinsky, J., *General circulation experiments with the primitive equations: I. The basic experiment*. *Monthly weather review*, 1963. **91**(3): p. 99-164.

32. Germano, M., et al., *A dynamic subgrid-scale eddy viscosity model*. Physics of Fluids A: Fluid Dynamics, 1991. **3**(7): p. 1760-1765.
33. Kim, W.-W. and S. Menon. *A new dynamic one-equation subgrid-scale model for large eddy simulations*. in *33rd Aerospace Sciences Meeting and Exhibit*. 1995.
34. Nicoud, F. and F. Ducros, *Subgrid-scale stress modelling based on the square of the velocity gradient tensor*. Flow, turbulence and Combustion, 1999. **62**(3): p. 183-200.
35. You, D. and P. Moin, *A dynamic global-coefficient subgrid-scale eddy-viscosity model for large-eddy simulation in complex geometries*. Physics of Fluids, 2007. **19**(6): p. 065110.
36. Spalart, P.R., *Strategies for turbulence modelling and simulations*. International Journal of Heat and Fluid Flow, 2000. **21**(3): p. 252-263.
37. Reynolds, O., *On the dynamical theory of incompressible viscous fluids and the determination of the criterion*. Proceedings of the Royal Society of London, 1894. **56**(336-339): p. 40-45.
38. Wilcox, D.C., *Turbulence modeling for CFD*. Vol. 2. 1998: DCW industries La Canada, CA.
39. Schmitt, F.G., *About Boussinesq's turbulent viscosity hypothesis: historical remarks and a direct evaluation of its validity*. Comptes Rendus Mécanique, 2007. **335**(9-10): p. 617-627.
40. Boussinesq, J., *Essai sur la théorie des eaux courantes*. 1877: Imprimerie nationale.
41. Blazek, J., *Computational fluid dynamics: principles and applications*. 2015: Butterworth-Heinemann.
42. Launder, B.E. and D.B. Spalding, *Lectures in mathematical models of turbulence*. 1972.
43. Fontaine, P.-O., *Modélisation des systèmes géothermiques à boucles horizontales pour chauffer les bâtiments et prévenir la fonte du pergélisol*. 2010, École Polytechnique de Montréal.
44. Claesson, J., A. Dunand, and G. Vachaud, *Mathematical analysis of heat extraction from horizontal pipes in the subsoil*. Document-Swedish Council for Building Research, 1983(16): p. 487-493.
45. Barakat, S., et al., *Enhancement of gas turbine power output using earth to air heat exchanger (EAHE) cooling system*. Energy conversion and management, 2016. **111**: p. 137-146.
46. Rodrigues, M.K., et al., *Numerical investigation about the improvement of the thermal potential of an Earth-Air Heat Exchanger (EAHE) employing the Constructal Design method*. Renewable Energy, 2015. **80**: p. 538-551.

47. Patankar, S.V. and D.B. Spalding, *A calculation procedure for heat, mass and momentum transfer in three-dimensional parabolic flows*. International journal of heat and mass transfer, 1972. **15**(10): p. 1787-1806.
48. Patankar, S., *Numerical heat transfer and fluid flow*. 1980: CRC press.
49. Ferziger, J.H. and M. Peric, *Computational methods for fluid dynamics*. 2012: Springer Science & Business Media.
50. Ansys, A.F., *17.0 Theory Guide*. ANSYS inc, 2017.
51. Sørensen, N.N., *General purpose flow solver applied to flow over hills*. 1995, Technical University of Denmark Danmarks Tekniske Universitet, Risø National Laboratory for Sustainable Energy Risø Nationallaboratoriet for Bæredygtig Energi, Wind Energy Division Afdelingen for Vindenergi, Aeroelastic Design Aeroelastisk Design.
52. Versteeg, H.K. and W. Malalasekera, *An introduction to computational fluid dynamics: the finite volume method*. 2007: Pearson Education.
53. Barth, T.J. and D.C. Jespersen, *The design and application of upwind schemes on unstructured meshes*. 1989.
54. Rhie, C. and W.L. Chow, *Numerical study of the turbulent flow past an airfoil with trailing edge separation*. AIAA journal, 1983. **21**(11): p. 1525-1532.
55. Popa, I., *Modélisation numérique du transfert thermique. Méthode des volumes finis*. Universitaria Craiova, 2002.
56. Van Doormaal, J. and G. Raithby, *Enhancements of the SIMPLE method for predicting incompressible fluid flows*. Numerical heat transfer, 1984. **7**(2): p. 147-163.
57. Walters, D.K. and D. Cokljat, *A three-equation eddy-viscosity model for Reynolds-averaged Navier–Stokes simulations of transitional flow*. Journal of fluids engineering, 2008. **130**(12): p. 121401.
58. NASA, *The Prediction of Worldwide Energy Resource (POWER) project*, <https://power.larc.nasa.gov/>, 2018.

Abstract

In this work, we are interested to the transient simulation of an Earth-Air Heat Exchanger (EAHE) installed in a local environment in the Biskra region (34°47'N - 5°43'E). The main objective is to evaluate the accuracy of numerical predictions of various analytical, semi-analytical and numerical methods. For this purpose, five transient approaches denoted as ICS, ILS, FLS, GRBM, and CFD have been implemented and validated using experimental data available in the literature. Same assumptions and boundary conditions have been applied for all models, in which the heat exchanger is considered as a horizontal tube buried in the soil subjected to a transient heat flux. Firstly, the undistributed soil temperature in the Biskra region has been analytically determined using Kusuda's equation. Then, the variation of the instantaneous air temperature as a function of the exchanger length has been calculated numerically. Good agreements between the numerical and experimental results were obtained, where the maximum relative error did not exceed 3% in all the studied cases.

Keywords: Earth-Air Heat Exchanger (EAHE), Geothermal energy, Thermal design, Analytical and semi-analytical methods, CFD.

Résumé

Dans ce travail, nous nous intéressons à la simulation transitoire d'un 'échangeur de chaleur air-sol (EAHE) installé dans un environnement local dans la région de Biskra (34°47'N - 5°43'E). L'objectif principal est d'évaluer la précision de prédictions numériques de diverses méthodes analytiques, semi-analytiques et numériques. À cette fin, cinq approches transitoires dénommées ICS, ILS, FLS, GRBM et CFD ont été mises en œuvre et validées à l'aide de données expérimentales disponibles dans la littérature. Dans un premier temps, la température non distribuée du sol dans la région de Biskra a été déterminée analytiquement à l'aide de l'équation de Kusuda. Ensuite, la variation de la température instantanée de l'air en fonction de la longueur de l'échangeur a été calculée numériquement. Bons accords entre les résultats numériques et expérimentaux ont été obtenus, où l'erreur relative maximale n'a pas dépassé 3% dans tous les cas étudiés.

Mots clés: Échangeur de chaleur air-sol (EAHE), Énergie géothermique, Conception thermique, Méthodes analytiques et semi-analytiques, CFD.

ملخص:

في هذا العمل، نحن مهتمون بالمحاكاة العابرة لمبادل حراري جو-أرض (EAHE) مثبت في بيئة محلية في منطقة بسكرة. الهدف الرئيسي هو تقييم دقة التنبؤات العددية للعديد من الطرق التحليلية وشبه التحليلية والرقمية. لهذا الغرض، تم تنفيذ خمسة طرق عابرة يشار إليها باسم ICS، ILS، FLS، GRBM و CFD والتحقق من صحتها باستخدام البيانات التجريبية المتاحة. تم تطبيق نفس الافتراضات وشروط الحدود على جميع النماذج، حيث يعتبر المبادل الحراري بمثابة أنبوباً أفقياً مدفوناً في الأرض يخضع لتدفق حراري متغير بالنسبة للزمن. أولاً، تم تحديد درجة الحرارة الثابتة للأرض في منطقة بسكرة تحليلياً باستخدام معادلة Kusuda. بعد ذلك، تم حساب التغير في درجة حرارة الهواء اللحظية كدالة لطول المبادل عددياً. تم الحصول على توافق جيد بين النتائج العددية والتجريبية حيث أن للخطأ النسبي الأعظمي لم يتجاوز 3% في جميع الحالات المدروسة.

الكلمات المفتاحية: مبادل حراري جو-أرض (EAHE)، طاقة حرارية أرضية، تصميم حراري، طرق تحليلية وشبه تحليلية، CFD.